

17490

NATIONAL LIBRARY
OTTAWA



BIBLIOTHÈQUE NATIONALE
OTTAWA

NAME OF AUTHOR.....LINDA DAVIES.....

TITLE OF THESIS.....INVERSION OF TRAVEL TIME DATA

UNIVERSITY...OF...ALBERTA.....

DEGREE FOR WHICH THESIS WAS PRESENTED.....M. Sc.....

YEAR THIS DEGREE GRANTED.....(19)73.....

Permission is hereby granted to THE NATIONAL LIBRARY
OF CANADA to microfilm this thesis and to lend or sell copies
of the film.

The author reserves other publication rights, and
neither the thesis nor extensive extracts from it may be
printed or otherwise reproduced without the author's
written permission.

(Signed).....Linda Davies.....

PERMANENT ADDRESS:

.....26 RIALTO DR.....

.....DON MILLS.....

.....ONT.....

DATED...30th May 1973

NL-91 (10-68)

THE UNIVERSITY OF ALBERTA

INVERSION OF TRAVEL TIME DATA

by

(C)

LINDA DAVIES

A THESIS

SUBMITTED TO THE FACULTY OF GRADUATE STUDIES AND RESEARCH

IN PARTIAL FULFILLMENT OF THE REQUIREMENTS FOR THE DEGREE

OF MASTER OF SCIENCE

IN GEOPHYSICS

DEPARTMENT OF PHYSICS

EDMONTON, ALBERTA

FALL, 1973

THE UNIVERSITY OF ALBERTA

FACULTY OF GRADUATE STUDIES AND RESEARCH

The undersigned certify that they have read, and
recommend to the Faculty of Graduate Studies and Research,
for acceptance, a thesis entitled INVERSION OF TRAVEL
TIME DATA submitted by Linda Davies in partial fulfillment
of the requirements for the degree of Master of Science
in Geophysics.

C. H. Chapman
Supervisor

J. W. Jackson

J. A. Kornishan

G. L. Cummings

Date ... 28th May 1973

ABSTRACT

The discreteness of travel-time data when using the Herglotz-Wiechert inversion technique results in a set of velocity depth profiles which will satisfy the data, rather than the unique model obtained when it is assumed that the data is continuous. The envelope of these models is analytically determined in this thesis for different types of data sets and computations of the velocity-depth profiles are then made for a number of cases.

The effect on the envelope width of changing the sampling interval is determined, as is the effect of knowing the velocity as a function of depth in certain regions (i.e. in the crust or down to the lower mantle).

In order to compare this method with other inversion methods, it is necessary to define an averaged radius which is then maximised and minimised so that a series of extremal curves is obtained, for a number of averaging lengths. This type of result (i.e. the variation in averaged velocity at any radius versus the averaging length) is directly comparable with, for example, the resolving power versus radius plots obtained by Gilbert and Backus type inversion. In previous work with Herglotz-Wiechert inversion, it has not been realised that to make any such comparison, it is necessary

to first average radius as a function of velocity, then maximise and minimise it and not vice versa. In this thesis these maximum and minimum averaged profiles are analytically determined and computations made to show the effect on an envelope of decreasing the averaging length.

Regions of high and low velocity are discussed and an 'earth-stripping' process is applied to some outer core data for which extremal velocity-depth profiles may then be obtained.

ACKNOWLEDGEMENTS

I am grateful to Dr. C.H. Chapman for his interest and encouragement in this thesis. I also wish to thank Dr. E. Nyland for his helpful discussions and Dr. R.A. Wiggins for his advice.

The helpfulness of the staff of Computing Services was also appreciated.

This thesis was supported by the Physics Department at the University of Alberta through a teaching assistantship and summer bursaries from Dr. C.H. Chapman's National Research Council grant.

All computations were done on the IBM 360/67 system of the Computing Centre of the University of Alberta.

TABLE OF CONTENTS

	<u>Page</u>
CHAPTER 1 INTRODUCTION	1
CHAPTER 2 BASIC METHOD OF INVERSION	10
CHAPTER 3 DISCRETE DATA	28
CHAPTER 4 LOW VELOCITY CHANNELS*	78
CHAPTER 5 TRIPPLICATIONS	88
CHAPTER 6 CONCLUSIONS	100
REFERENCES	104
APPENDIX 1	108
APPENDIX 2	112
APPENDIX 3	114

LIST OF FIGURES

<u>Figure</u>		<u>Page</u>
1.1	Path of ray, with ray parameter p , indicating various ray characteristics (Bullen 1965, p.111).	3
1.2	Sketch to show the effect of the k^{th} low velocity channel on turning point of rays immediately above and below channel.	6
2.1	A typical travel time ($T-\Delta$) curve showing the three types of discontinuity.	11
2.2	Illustration of the "earth-stripping" concept for a ray entering a type II low velocity region. In this case the rays used are Pcp and PKP (Macelwane 1951, p.286).	15
2.3	Both type 'I' and II discontinuities in the $p-\Delta$ plane. The distance between the reflected and direct ray, $\delta\Delta(p)$ (as shown) is the 'effective' range of the "earth-stripping" process.	17
2.4	The travel-time curve obtained by the "earth-stripping" process, as illustrated in fig. 2.3.	18
2.5	Both this and fig. 2.6 are travel time data, which includes low velocity channels, transposed to the $p-r$ (i.e. ray parameter versus turning radius) plane. In both figures r_k , \bar{r}_k are the	20

FigurePage

2.5 (cont'd) top and bottom radii of the k^{th} low velocity zone, respectively and the cross hatched areas represent the first of the double integrals in equations (2.5) and (2.6). Figure 2.5 shows the order of integration in equation (2.5).

2.6 This diagram shows the order of integration in equation (2.6). 21

2.7 A velocity radius profile for perfect, continuous data, including a low velocity zone. As can be seen, even under these circumstances velocity cannot be determined exactly as a function of radius below $r(p^{(1)})$ (i.e. the radius at the top of the low velocity channel). 24

2.8 The function $\phi(p)$ defined in the equation for an averaged radius. 26

3.1 The bounds on any model for (p, T, Δ) data in the $p-\Delta$ plane (i.e. ray parameter in sec/deg versus range in degs). An arbitrary $p(\Delta)$ curve is also shown, where, to satisfy the data, the curve must always be with the bounds. 31

3.2 A sketch of $\cosh^{-1} p/q$ as a function of p , showing that any small perturbation, δp , away from the mean, will result in a decrease in the value of $I^{(o)}(q)$. 32

FigurePage

- 3.3 The $p(\Delta)$ curve, in the $p-\Delta$ plane, which will maximise $I^{(o)}(q)$ where the inset refers to the change in end point if $q < m_j$. The untrained end point would be similar to that shown in the main diagram but with $p = m_j^*$ rather than u_j . 34
- 3.4 Sketch of a family of $I^{(o)}(q)$ curves, where $I^{(o)}(q)$ decreases as a function of increasing q . Hence the value of m_j^* will depend on q and may be constrained to u_j or m_j . 35
- 3.5 A plot in the $p-\Delta$ plane of the band of possible $p(\Delta)$ curves where the solid lines through the boxes is the $p(\Delta)$ curve which minimises $I^{(o)}(q)$. The inset refers to the alternative end point value if $q < m_j$. 37
- 3.6 Radius-velocity plot to show the effect of decreasing the sampling width from 5° , to 3° and 1° . The range of q values used is also indicated. 40
- 3.7 Radius-velocity plot for (p, T, Δ) data with the effect of fixing part of the model indicated by broken lines. 42
- 3.8 A radius-velocity plot with the envelope of profiles represented by the solid lines and three individual profiles, which are also the extreme profiles for $q = q_{\max}$, represented 45

FigurePage3.8
(cont'd)

by broken lines. The lines across the envelope are the values of ϕ , as shown.

3.9

A graph of $\phi(p)$, the averaging function defined by equation (2.9).

48

For $b < p < \eta_0$, a perturbation δp from the mean, $p = m_i$, will result in a decrease in the area under the $\phi(p)$ curve. For $a < p < b$, a perturbation δp from $p = m_j$ will result in an increase in the area under the $\phi(p)$ curve.

3.10

The values of $p(\Delta)$ about the point $p = b$ which will, in general, maximise the integral, are represented by the solid lines through the boxes.

49

3.11

The values of $p(\Delta)$ about the point $p = b$ which will minimise the integral, as represented by solid lines through the boxes.

53

3.12

The two possible ways of minimising the integral about the point $p = b$ as shown by (1) and (2).

54

3.13

A plot of extremal radius as a function of the averaging window, $(b - a)$, for $\eta = 6.5$ with the model fixed to $p = 7.60$ sec/deg.

57

FigurePage

- 3.14 A plot of extremal radius as a function of the averaging window, $(b - a)$, for $n = 6.3$ with the model fixed to $p = 7.60 \text{ sec/dég}$. 58
- 3.15 An alternative way of plotting fig. 3.14, that is by representing the variation in extremal radii as a function of averaging length by a series of error circles in a radius versus n plot. 60
- 3.16 A radius-velocity plot for the same region as in fig. 3.8 where the solid line is for a zero averaging length. All sets of broken curves are for various averaging lengths, as shown. The relation to n (i.e. q in fig. 3.8) is shown by the solid lines across the curves and the values of n are as shown. 62
- 3.17 These box structures in the $p-\Delta$ plane represent the bounds on permissible $p(\Delta)$ curves for inversion when using (p, Δ) data. The extremal $p(\Delta)$ curves are as shown, as is an arbitrary curve. 65
- 3.18 The $p(\Delta)$ curves which give the extremal values of the averaging integral and hence the averaged radius, for (p, Δ) data. 67

FigurePage

3.19 The band of permissible models, in the $p-\Delta$ plane, for (T, Δ) data. The maximising $p(\Delta)$ curve is as shown. 68

3.20 The minimising $p(\Delta)$ curve for (T, Δ) data is represented by the solid line through the band structure. The end point, $\Delta(q)$, is that for $w_j \leq q < m_j$. 71

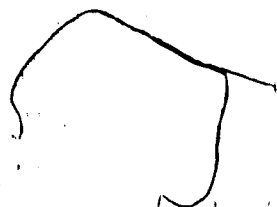
3.21 The $p(\Delta)$ curve which will maximise the integral is shown as a solid line through the band structure, with $b-$ a the interval over which an average radius is taken. 74

3.22 The minimising $p(\Delta)$ curve for (T, Δ) data for an averaging interval $b-$ a is represented by the solid line through the band structure. 76

4.1 Radius-velocity plot for the outer core region, using 'earth stripped' PKP and SKS data. 79

4.2 The upper and lower limits on τ for (T, p) data, shown in the $\tau-p$ plane. 86

5.1 Ray parameter, p , in sec/deg, as a function of range, Δ , in deg. This $p(\Delta)$ curve shows a triplication with an example of possible data, for unobserved triplications at data points, superimposed. 89

FigurePage

- 5.2 The band structure, in the $p-\Delta$ plane, for an unobserved triplication at Δ_i . The cross hatched area shows the usual band width if no triplications occur while the shaded region shows the increase in band width necessary to accommodate the type of situation illustrated in fig. 5.1. 91
- 5.3 Portion of the $T-\Delta^0$ which includes a triplication. The labels on the difference branches of the curve correspond to sections of the $p(\Delta)$ curve shown in fig. 5.4. 92
- 5.4 The $p(\Delta)$ curve in the i^{th} interval which will maximise the Herglotz-Wiechert integral when a triplication is observed at Δ_i . Labels A and C refer to the forward branches of the travel-time curve, as shown in fig. 5.3 while B refers to the reverse branch. 93
- 5.5 The more general maximisation curve in the i^{th} interval, where \hat{p}_i is the value of p which will maximise $I^{(o)}(q)$ and also satisfy time constraints. 95
- 5.6 The change in the maximisation curve of fig. 5.5 for smaller value of q . 96

FigurePage

- 5.7 The $p(\Delta)$ curve which will minimise $I^{(0)}(q)$ in the i^{th} interval, for $q > m_i$. 97
- 5.8(a) Possible minimisation curve for $q < m_i$. 98
- 5.8(b) Both this and fig. 5.8(a) show possible minimisation curves for $q < m_i$. The curve giving the absolute minimum may be determined numerically. 99
- A3.1 Diagram to show behaviour of $\phi/\sin \phi$ and $(n_{\min}^{(k)}(\bar{r}^{(k)})^2 - q^2)/n_{\min}^{(k)}(r)^2 - q^2$ and hence determine the sign of $\delta I^{(k)}(q)$. 118
- A3.2 A radius-velocity plot for a low velocity channel with $\bar{r}_{\max}^{(1)}$ and $\bar{r}_{\min}^{(1)}$ the maximum and minimum radii for the bottom of the low velocity channel (as determined by $\delta r^{(1)}$). The shaded curves are those obtained from the low velocity channel model while the cross-hatched area is produced by perturbing the model. 121

CHAPTER 1

INTRODUCTION

One of the basic studies of geophysics is, given surface observations, to determine internal structure. In seismology, given a set of arrival times of seismic waves at known distances from the source (i.e. a travel-time curve) is it possible to determine the corresponding velocity-depth profile in the earth? This is the problem of inverting body wave data, and is the subject of this thesis.

There are a number of direct and indirect methods of inverting travel time data. These include:

(1) Herglotz-Wiechert inversion effectively integrates a function of a travel-time ($T-\Delta$) curve to any range and determines the velocity at corresponding depth (this will be discussed later in more detail).

(2) The Monte Carlo method has been applied to $T-\Delta$ data by Press (1968, 1970 a,b), Wiggins (1968) and others. It involves trial and error on a large scale and, as such, is very expensive in terms of computing. The method has the further disadvantage of providing solutions with little real insight into the physics involved.

(3) Gilbert-Backus inversion involves linear perturbations of a starting velocity model until in agreement with known travel-time data. It has been

discussed by Johnson and Gilbert (1972) and others.

Both (2) and (3) are indirect methods. That is, given a velocity model, time (T) and surface path length (Δ) must be computed and compared with observed values, to test the model's validity.

This thesis will be concerned with the first method, which is a direct inversion technique. The same notation as in Bullen (1963) will be used, as this notation rather than that of the earth flattened system (Gerver and Markushevich, 1966, 1967, McMechan and Wiggins, 1971, Wiggins, McMechan and Toksöz, 1972) is more frequently encountered in seismology (though the latter does have slight algebraic advantages).

From the properties of geometric optics (i.e. for a ray obeying Snell's law):

$$\Delta(p) = 2 \int_{s(p)}^{r_o} \frac{p dr}{r(n^2 - p^2)^{1/2}} \quad (1.1)$$

$$T(p) = 2 \int_{s(p)}^{r_o} \frac{n^2 dr}{(n^2 - p^2)^{1/2}} \quad (1.2)$$

where, as illustrated in fig. 1.1, $\Delta(p)$ is the angular separation between the source and the receiver for a ray, with ray parameter p ;

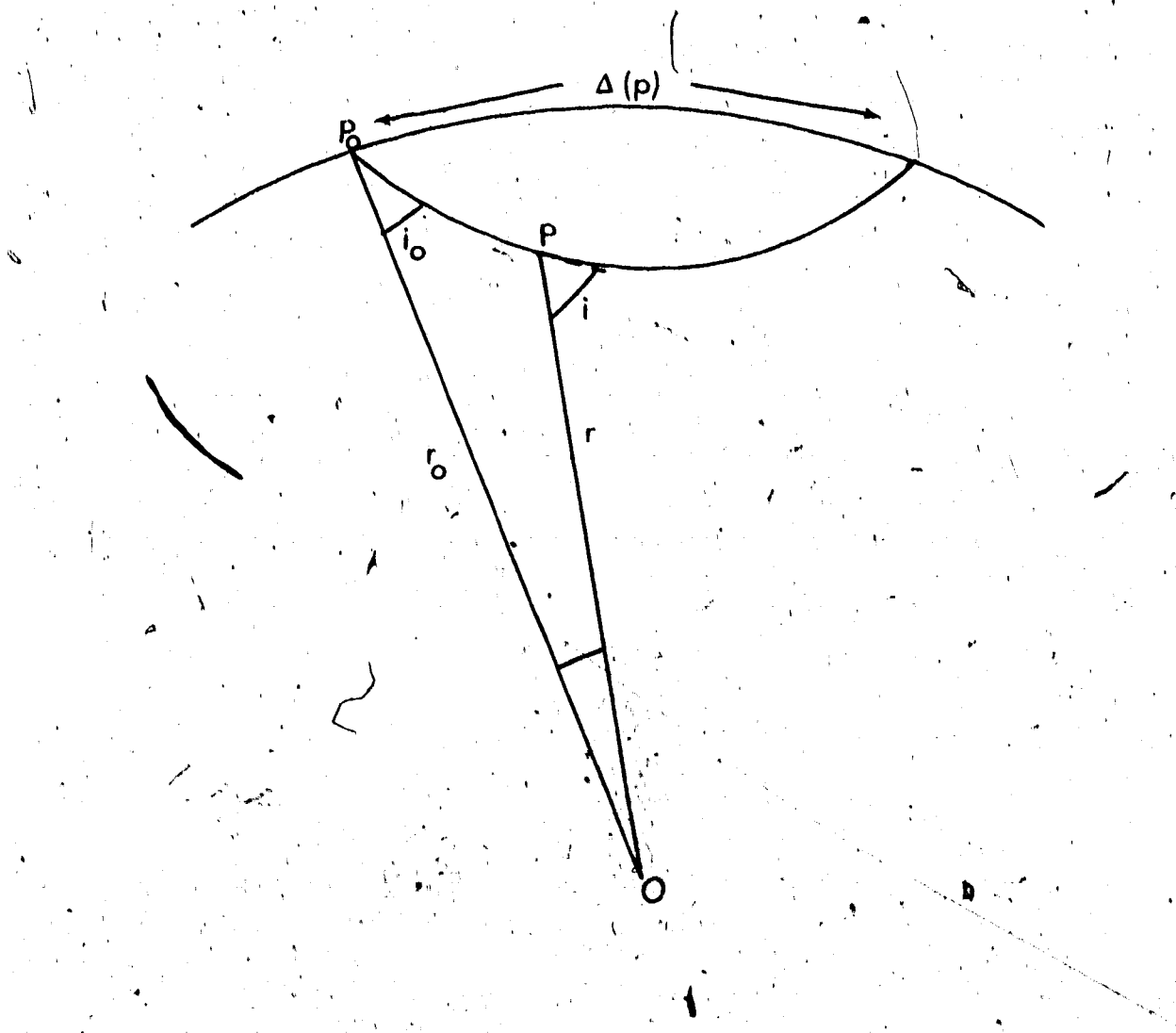


Fig. 1.1. Path of ray, with ray parameter p ,
indicating various ray characteristics
(Bullen 1965, p.111).

r_0 is the source and receiver radii (assumed equal).

p the ray parameter, is the distance derivative of the travel-time curve. It is also the reciprocal of the apparent velocity of a body wave across the surface of the earth (i.e. angular slowness).

$s(p)$ is the radius at which the ray bottoms.

η is the ratio $r/v(r)$.

$T(p)$ is the travel time for the ray with ray parameter p .

The assumptions necessary to make equations (1.1) and (1.2) valid will be discussed later.

Equation (1.1), which is a form of Abel's integral equation, was first investigated in relation to seismology independently by Herglotz (1907) and Bateman (1910) and later simplified by Wiechert (1910). Their solution, the classical inversion equation, is :

$$\pi \ln \frac{r_0}{s(q)} = \int_0^{\Delta(q)} \cosh^{-1} \left(\frac{p}{q} \right) d\Delta \quad (1.3)$$

This equation says that the radius $s(q)$ at which a chosen ray, with ray parameter q , turns may be determined because the structure above $s(q)$ has already been calculated using the same equation. Here, $\Delta(q)$ is the range of this chosen ray.

This method of inversion has only recently been extended to include the effect of wave guides (Gerver and Markushevich, 1966, 1967). Equation (1.3) assumes that a small perturbation, δp , in the ray parameter will produce correspondingly small changes, δr , in the radius at which the ray bottoms and δv in the turning ray velocity. Obviously this will not be true if low velocity channels are included and the more general inversion equation is :

$$\pi \ln \frac{r_0}{s(q)} = \int_0^{\Delta(q)} \cosh^{-1}(\frac{p}{q}) d\Delta + \sum_{k=1}^{k^*} \int_{r_k}^{r_{k^*}} \frac{2}{r} \times \tan^{-1} \sqrt{\frac{n^2 - p_k^2}{p_k^2 - q^2}} dr \quad (1.4)$$

(this equation will be discussed in Chapter 2)

where each low velocity channel is assumed independent of the others and the summation represents the effect of channels 1 through k^* . All other symbols are as previously defined, where the subscript k refers to the k^{th} low velocity channel, as illustrated in fig. 1.2.

A number of assumptions must be made in this inversion:

- (1) Both source and receiver radii are equal to r_0 .

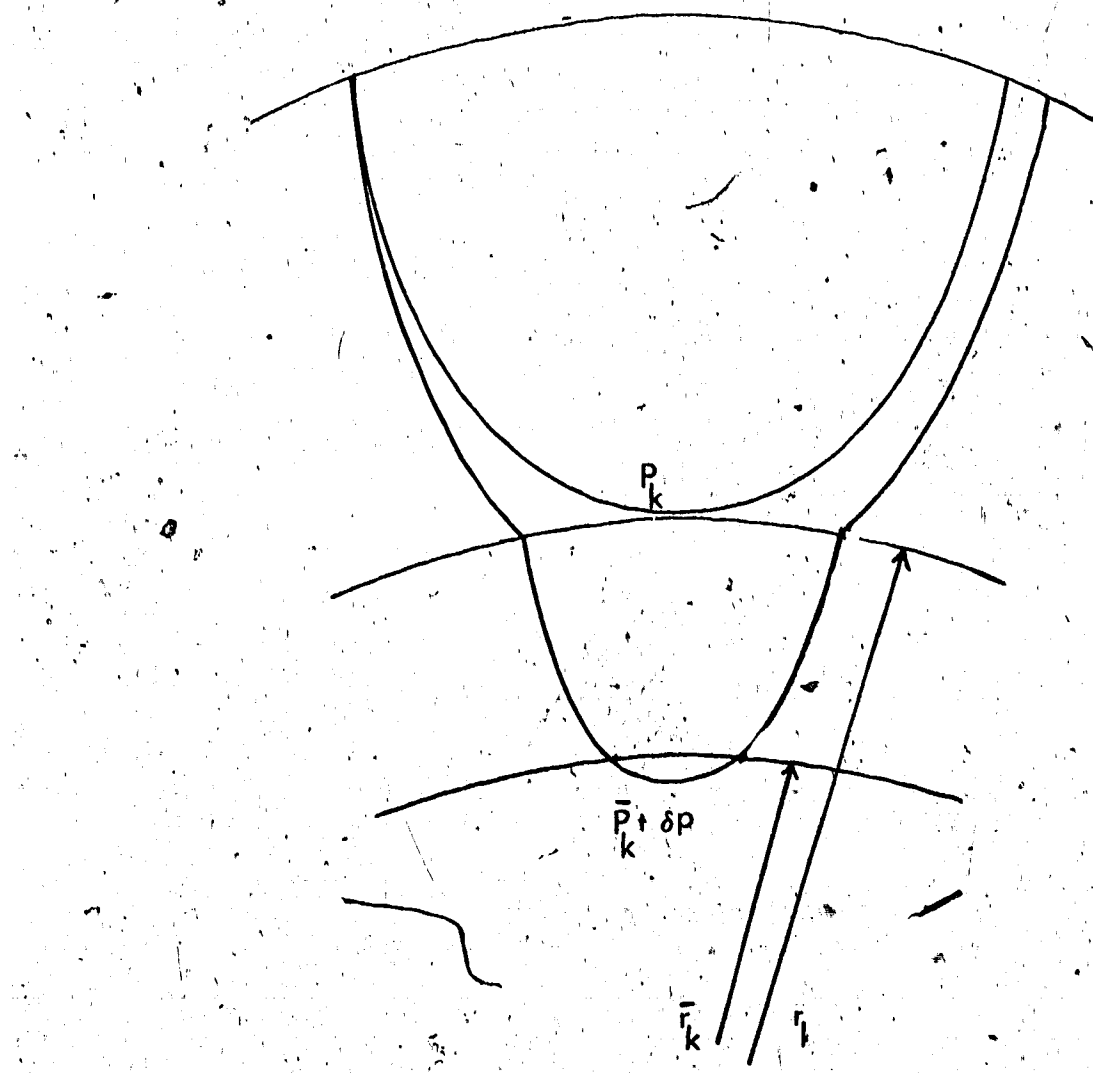


Fig. 1.2. Sketch to show the effect of the k^{th} low velocity channel on turning point of rays immediately above and below channel.

(2) Only one ray type and velocity is being investigated.

(3) The velocity $v(r)$ is non-zero and may be discontinuous, as can the first and second derivatives, but only at a finite number of points. Elsewhere the second derivative must be continuous.

(4) It is assumed the complete $T-\Delta$ curve is known exactly (i.e. all values of p from q to r_o/v_o ($=n_o$) are known).

(5) There is no ambiguity of $2n\pi$ in Δ , except possibly in the inner core. This is reasonable as rays which have path lengths greater than 2π will have much reduced amplitudes.

If all the above assumptions are true, then knowing $p = n_o$ at $\Delta = 0$ it is possible to calculate velocities near the surface radius r_o . As p decreases, that is as deeper rays are sampled, corresponding velocities may be determined because the velocity structure above the ray being sampled has already been found.

Practically, data will be discrete rather than continuous, so that the $T-\Delta$ curve will be represented by a set of points rather than a continuous line. That is, in moving from one range to the next there is an ambiguity in the velocity depth structure "seen" by rays at these ranges. For the Herglotz-Wiechert

inversion method, this discreteness of the data means that for a chosen ray (with ray parameter q), there will be an indefinite number of velocity models above the radius ($s(q)$) where the ray turns, which fit the data (because of the above mentioned ambiguity).

Hopefully for each chosen ray, it will be possible to select the velocity models which will maximise and minimise $s(q)$ (and hence maximise and minimise the ray's velocity at the turning point, if low velocity zones are temporarily ignored). This thesis is concerned with this problem.

As will be shown in Chapter 3, discrete data in a $T-\Delta$ curve corresponds to an envelope in the $p-\Delta$ plane ($p = dT/d\Delta$) and it is possible to analytically determine $p(\Delta)$ curves in this plane which:

- (1) give extremal values of the integral of equation (1.3) and hence extremal velocity-depth profiles,
- (2) lie completely within the $p-\Delta$ envelope,
- (3) satisfy the travel-time constraint

$$\int_0^{\Delta(p)} p \, d\Delta = T(p).$$

The presence of low velocity channels presents difficulties and though it is still possible to find the extremal paths of integration, the complete analytic

solution has not yet been obtained.

Regions of high velocity gradient have been treated by McMechan (1971) and will be discussed in Chapter 4.

Arbitrary $p(\Delta)$ curves in the $p-\Delta$ plane correspond to non-extremal velocity-depth profiles which will certainly touch the extremal curves but will drop away again (this will be shown in Chapter 3).

For example, at a particular radius, an arbitrary model will actually define the maximum velocity.

Bessonova et al (1970) and Keilis-Borok (1970) define an average radius which is effectively the turning radius from an averaged velocity profile. The corresponding average velocity-depth curve may also be maximised and minimised, as will be shown in Chapter 3.

A trade off curve may then be computed for the width of the averaged velocity-depth envelope versus the range of p over which the averaging is taken. This will provide a direct comparison with the Gilbert-Backus results (which is intimately concerned with the trade-off of resolution versus accuracy) and the Monte Carlo method (which will give a low "density" of models through extremal points).

CHAPTER 2

BASIC METHOD OF INVERSION

Initially perfect, continuous travel-time data will be considered, so that certain features of the travel-time curve may be determined. Regions of high or low velocity gradient introduce various anomalies into travel-times, as illustrated in fig. 2.1. These anomalies are:

(1) A triplication, which is a region of high velocity gradient. For continuous data, triplications cause no problem in inversion and have been investigated by McMechan (1971) for discrete data.

(2) A type I discontinuity, which is due to a discontinuous decrease in velocity gradient at radius $r^{(k)}$ such that

$$n(r^{(k)} + 0) < n(r^{(k)} - 0)$$

where $(r^{(k)} + 0)$ is the radius just above and $(r^{(k)} - 0)$ that just below $r^{(k)}$. An example of this structure is the core.

(3) A type II discontinuity, as with the low velocity zone, is caused by a continuous decrease in velocity gradient at r_k , such that

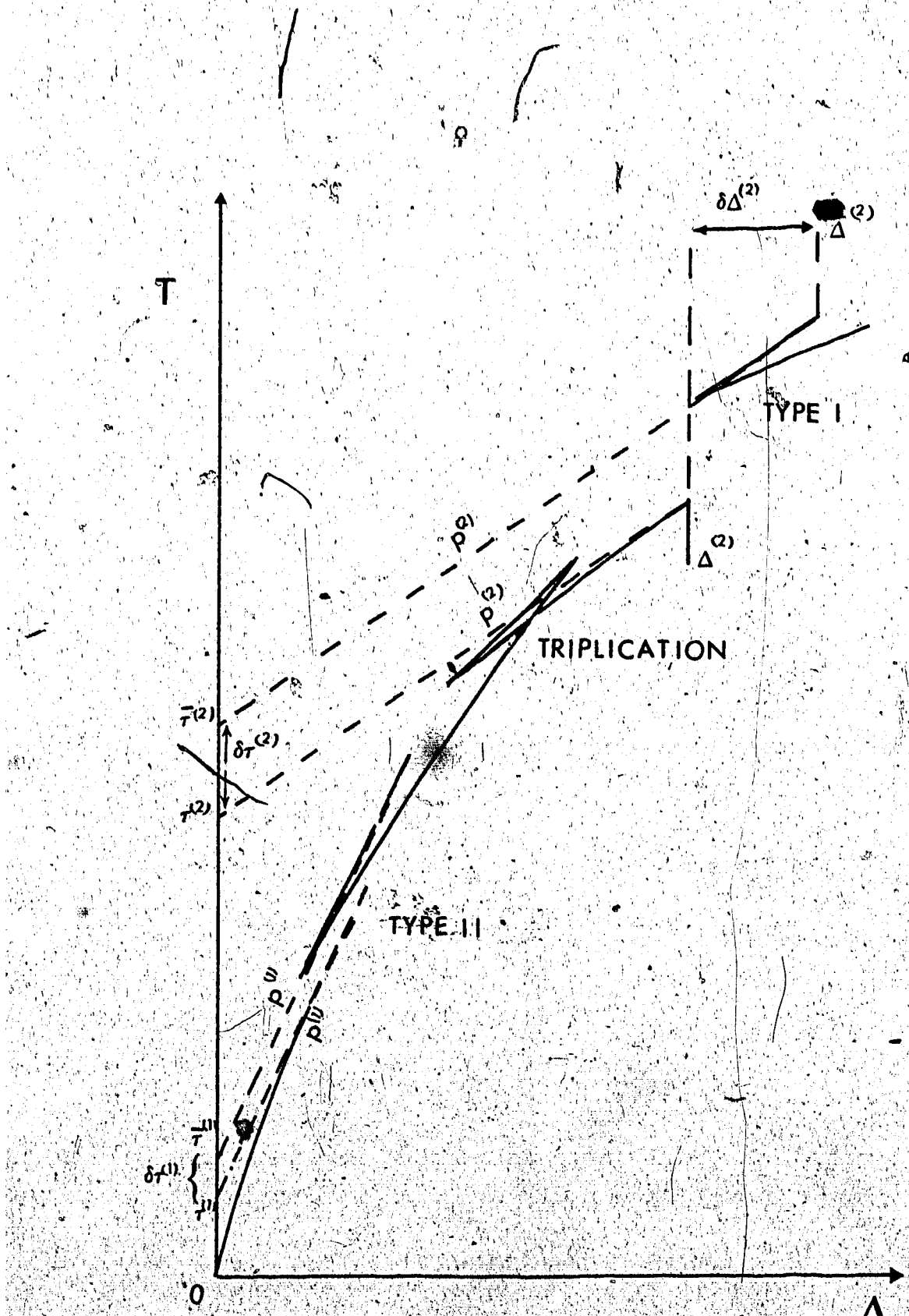


Fig. 2.1. A typical travel time ($T-\Delta$) curve
showing the three types of discontinuity:

$$n'(r_k) = 0 \quad (2.1)$$

In practice (2) may not be a clear discontinuity in Δ because of smearing by diffraction. A third type of discontinuity, I' , must also be considered. This is a combination of types I and II, such that

$$n'(r^{(k)} + 0) = 0 \quad (2.2)$$

$$n(r^{(k)} + 0) < n(r^{(k)} - 0) \quad (2.3)$$

This type of discontinuity may be a result of uncertainties in types I and II and it has been suggested (Bolt, 1972) for the D'' branch, at the core-mantle boundary.

A type I or I' discontinuity may be inverted more easily than a type II discontinuity and it is therefore important to determine their differentiating characteristics. Before proceeding further, it should be noted that the parameter τ , defined in fig. 2.1, may also be written in integral form

$$\tau(p) = T - p\Delta = 2 \int_0^{\infty} \frac{(n^2 - p^2)^{1/2}}{r} dr \quad (2.4)$$

Though, as indicated in fig. 2.1, T , Δ and τ remain finite at a type I discontinuity, the exact end points $\Delta^{(k)}$ ($= \Delta(p^{(k)} + 0)$) and $\bar{\Delta}^{(k)}$ ($= \Delta(p^{(k)} - 0)$) cannot be clearly defined because of non-geometric effects.

Thus, it is very difficult to determine the type of discontinuity directly from the travel-time curve and amplitude properties must be inspected instead.

Using wave theory it is possible to show that for type I, the amplitude of a diffracted signal decays exponentially for $\Delta > \Delta^{(k)}$ with a cube root dependence on frequency (equation (A1.3)). Similarly, for type II, the diffracted signal amplitude decays exponentially for $\Delta > \Delta^{(k)}$ but is independent of frequency (equation (A1.5), $j=0$). This result agrees with that obtained by geometric considerations (equation (A2.3)). For a type I' discontinuity we find that the amplitude behaviour is the same as for type II but with a decay rate which depends on the boundary conditions (equation (A1.6)).

It is assumed that the velocity model to just above the low velocity zone has been inverted and is known. Ideally, it is possible to determine the type of discontinuity through amplitude inspection, though in practice amplitude data is difficult to analyse.

For both type I' and II discontinuities $\Delta^{(k)}$ and $\pi^{(k)}$ are infinite and obviously the whole curve $\Delta(p)$, as p tends to $p^{(k)}$, cannot be observed. However, it is possible to extrapolate the model to $r^{(k)}$, using equation (A2.1) and hence calculate $\pi^{(k)}$ (equation (2.4)).

Similarly, using equation (A2.2), $\Delta(p)$ can be extrapolated, for p tending to $p^{(k)}$, from above and below and hence an estimate of $\tau^{(k)}$ obtained. This then provides a value of $\delta\tau^{(k)}$ where

$$\delta\tau^{(k)} = 2 \int_{r^{(k)}}^{r^{(k)}} \frac{1}{r} \left(\eta^2 - p^{(k)} \right)^{\frac{1}{2}} dr$$

A second constraint, $\delta\Delta^{(k)}(p)$, which is illustrated in fig. 2.2, is indeterminate for a type II discontinuity but remains finite as p tends to $p^{(k)}$ for both types I and I'. For the latter, the ranges themselves become infinite about the discontinuity though their difference, $\delta\Delta^{(k)}$, remains finite. This parameter is not directly observed but may be calculated as

$$\delta\Delta^{(k)}(p) = \Delta(p) - 2 \int_{r^{(k)}}^{r^{(k)}} \frac{p dr}{r(\eta^2 - p^2)^{\frac{1}{2}}}$$

and

$$\delta\Delta^{(k)} = \delta\Delta^{(k)}(p^{(k)})$$

These measurements $\delta\tau^{(k)}$ and $\delta\Delta^{(k)}$, whether directly observable (type I) or estimated by extrapolating off the last data point (type I') can be thought of as data from a "stripped" earth, to a radius $r^{(k)}$. This is illustrated in fig. 2.4, which shows the travel

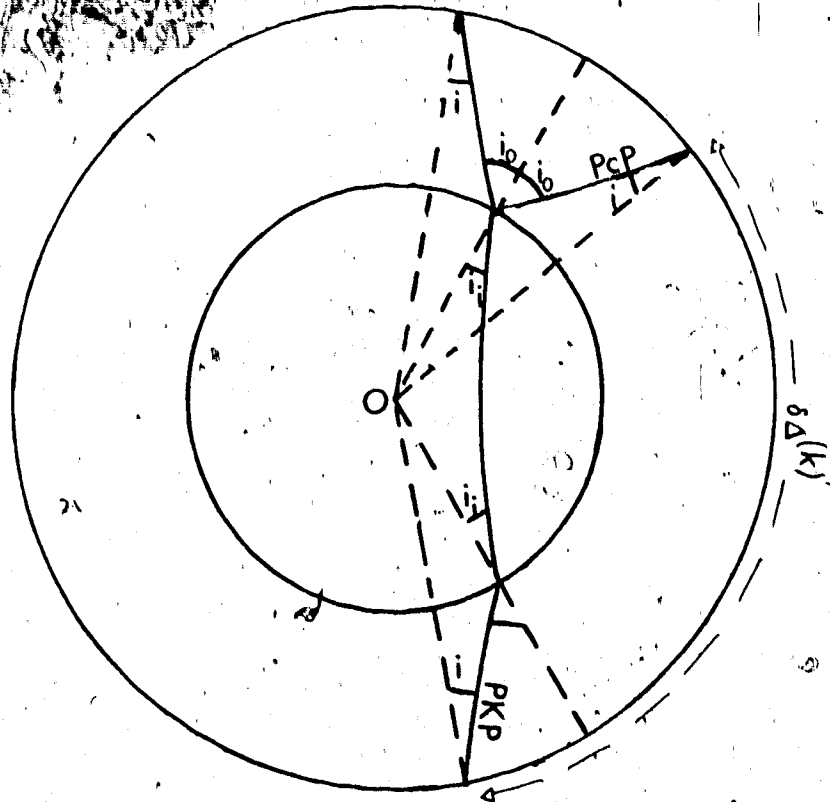


Fig. 2.2. Illustration of the "earth-stripping" concept for a ray entering a type II. low velocity region. In this case the rays used are PcP and PKP (Macelwane 1951, p.286).

time curve for such a "stripped" earth. An "earth-stripping" process (Macelwane, 1951) removes the reflection time, which effectively removes the layers above the discontinuity, as shown in fig. 2.3 in the $p-\Delta$ plane. Thus, a $\delta T^{(k)} - \delta \Delta^{(k)}(p)$ curve is obtained which will have no observed values below $\delta \Delta^{(k)}(p^{(k)})$, $\delta T^{(k)}(p^{(k)})$, (fig. 2.4) though it may be possible to fill the lower part of this curve with other data, for example SKS for the outer core. If this supplementary data does not exist, the situation becomes a special type of discrete data problem, which will be discussed in Chapter 3. With this technique, it is most convenient to assume that there are no triplications or low velocity zones within the region of the low velocity zone (i.e. velocity increases smoothly with depth between $r^{(k)}$ and $\bar{r}^{(k)}$). Multiple zones could be included but will not be studied here.

The above process is not possible for a type II discontinuity because $\delta \Delta^{(k)}(p^{(k)})$ is undefined. Instead the results of Gerver and Markushevich (1966, 1967), which generalise the classical Herglotz-Wiechert integral to include low-velocity channels (equation (1.4)), must be applied. These results will now, therefore, be derived. It should be noted that to compare the following with the results of Gerver and Markushevich, the

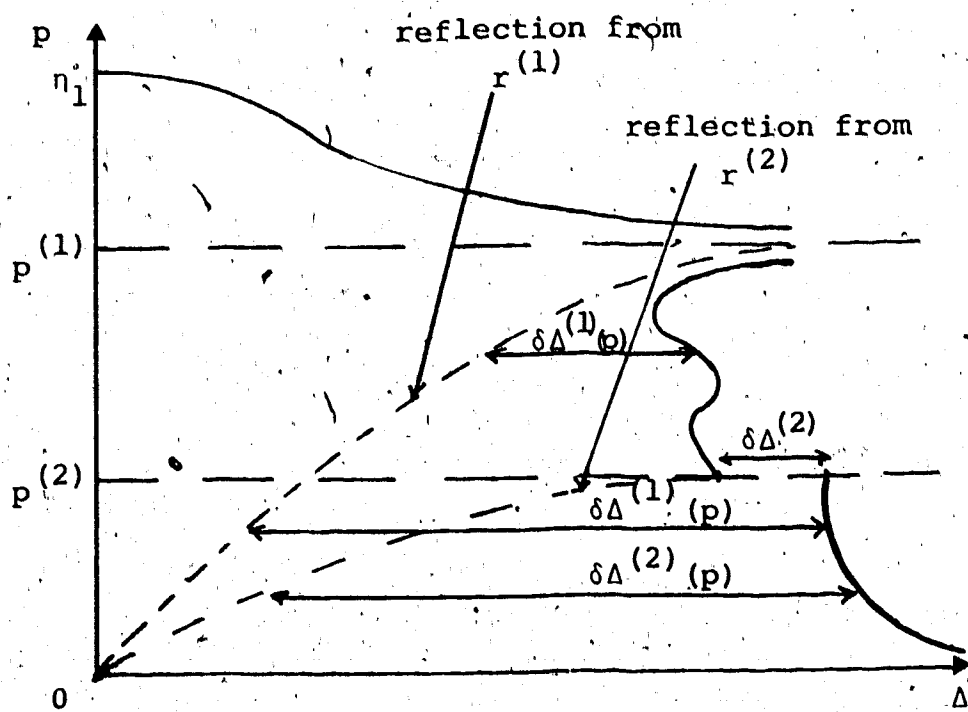


Fig. 2.3. Both type I' and II discontinuities in the p - Δ plane. The distance between the reflected and direct rays, $\delta\Delta(p)$ (as shown) is the 'effective' range of the "earth-stripping" process.

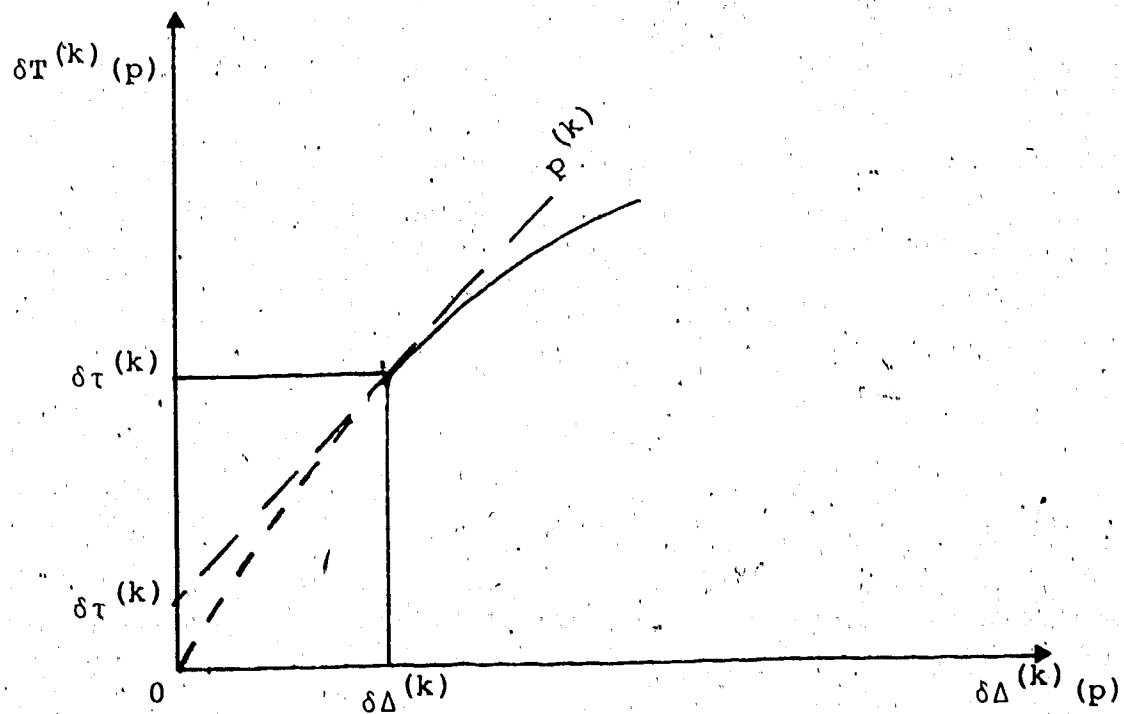


Fig. 2.4. The travel-time curve obtained by the "earth-stripping" process, as illustrated in fig. 2.3.

transformations from earth flattened to spherical co-ordination must be used. The operation

$$\int_q^{n_o} \frac{dp}{(p^2 - q^2)^{\frac{1}{2}}}$$

is applied to $\Delta(p)$ (equation (1.1)) :-

$$\int_q^{n_o} \Delta(p) \frac{dp}{(p^2 - q^2)^{\frac{1}{2}}} = \int_q^{n_o} \left[\int_{s(p)}^{r_o} \frac{2p dr}{r(n^2 - p^2)^{\frac{1}{2}}} \right] \frac{dp}{(p^2 - q^2)^{\frac{1}{2}}} \quad (2.5)$$

The right hand side of equation (2.5) is equivalent to an integral over the area $D^{(o)}(q)$ in the p-r plane, as shown in fig. 2.5, where the total area between the points $(s(q), n(r))$ and (r_o, q) is defined to be $D(q)$.

$$D(q) = D^{(o)}(q) + \sum_{k=1}^{k_q} D(k)$$

$$\text{for } p^{(k_q+1)} \leq q < p^{(k_q)}$$

If the order of integration is reversed, as shown in fig. 2.6, then

$$\int_q^{n_o} \frac{\Delta(p) dp}{(p^2 - q^2)^{\frac{1}{2}}} = \int_{s(q)}^{r_o} \int_q^{n(r)} \frac{2p dr dp}{r(n^2 - p^2)^{\frac{1}{2}} (p^2 - q^2)^{\frac{1}{2}}} \quad (2.6)$$

$$\sum_{k=1}^{k_q} \int_{r(k)}^{r(k+1)} \int_{p(k)}^{n(r)} \frac{2p dr dp}{r(n^2 - p^2)^{\frac{1}{2}} (p^2 - q^2)^{\frac{1}{2}}} \quad (2.6)$$

$$D(k)(q)$$

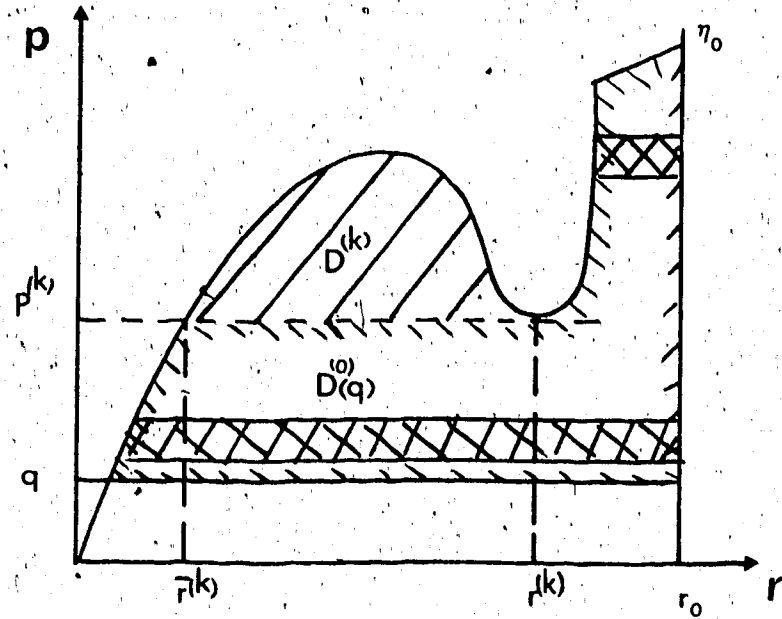


Fig. 2.5. Both this and fig. 2.6 are travel time data, which includes low velocity channels, transposed to the $p-r$ (i.e. ray parameter versus turning radius) plane. In both figures r_k , \bar{r}_k are the top and bottom radii of the k^{th} low velocity zone, respectively and the cross-hatched areas represent the first of the double integrals in equations (2.5) and (2.6). Fig. 2.5 shows the order of integration in equation (2.5).

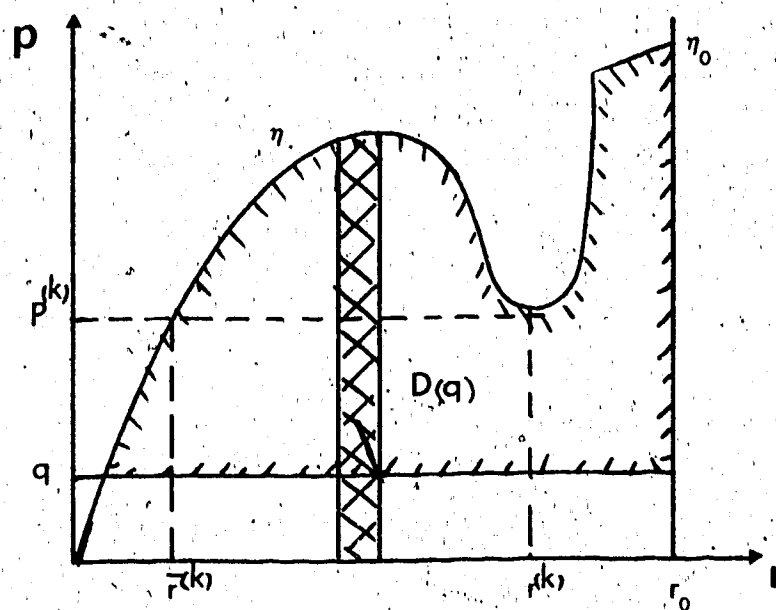


Fig. 2.6. This diagram shows the order of integration
in equation (2.6).

In general,

$$\int \frac{p dp}{(n^2 - p^2)^{\frac{1}{2}} (p^2 - q^2)^{\frac{1}{2}}} = -\tan^{-1} \sqrt{\frac{n^2 - p^2}{p^2 - q^2}}$$

and hence the first term on the right in (2.6) reduces to

$$\pi \ln \left\{ \frac{r_o}{s(q)} \right\}$$

Integrating the left hand side by parts gives

$$\int_0^{\Delta(q)} \cosh^{-1} \left(\frac{p}{q} \right) dA$$

and so the equation becomes :

$$\begin{aligned} \ln \frac{r_o}{s(q)} &= \frac{1}{\pi} \int_0^{\Delta(q)} \cosh^{-1} \left(\frac{p}{q} \right) dA + \frac{1}{\pi} \sum_{k=1}^{k=q} \underbrace{\int_{r^{(k)}}_{r^{(k)}} \frac{2}{r} \times}_{\tan^{-1} \sqrt{\frac{n^2 - p^{(k)} \cdot 2}{p^{(k)} \cdot 2 - q^2}} dr} \\ &= I^{(0)}(q) + \sum_{k=1}^{k=q} I^{(k)}(q), \text{ say.} \end{aligned} \quad (2.7)$$

Obviously, for $p^{(1)} < q \leq n_o$, the classical result is obtained, where the summation term is ignored, and for "perfect" data this will produce a unique velocity-depth profile. As explained above, for q tending to $p^{(1)}$, the upper depth, $(r^{(1)})$ at the low velocity channel

is known, but its extent is not, as it depends on how the velocity function varies within the channel.

Thus, even for "perfect" data, it is only possible to impose limits on the velocity model for $q < p^{(1)}$, using the constraint $\delta r^{(1)}$ (fig. 2.7). This will be discussed in more detail in Chapter 3.

With discrete data, $p(\Delta)$ is not known exactly and hence $I^{(0)}(q)$ cannot be evaluated explicitly.

However, if maximum and minimum values of $I^{(0)}(q)$ can be found, while still satisfying the data, this

will give minimum and maximum velocity and radius values and define the envelope mentioned previously.

The problem of inverting low velocity channels of type II can similarly be specified as finding the extremal values of $I^{(k)}(q)$ which fit the data (continuous or discrete).

When considering low velocity models, numerical instabilities are encountered, in that thin, very deep low velocity zones cause only small changes in $T(\Delta)$ (Keilis - Borok, 1970, Bessonova et al, 1970). Hence, rather than calculating the "true" profile an average structure may be used, which will be more stable. In radial variables, the definition equivalent to Bessonova et al's (1970) is

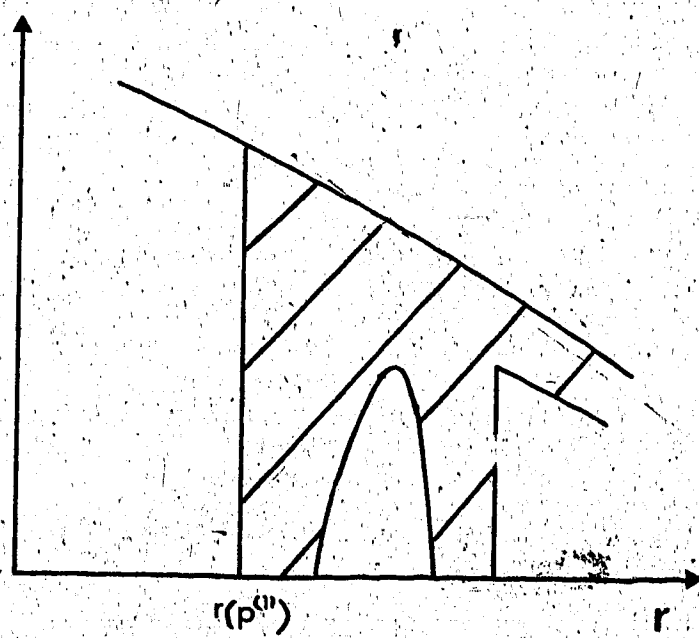


Fig. 2.7. A velocity radius profile for perfect, continuous data, including a low velocity zone.

As can be seen, even under these circumstances velocity cannot be determined exactly as a function of radius below $r(p^{(1)})$ (i.e. the radius at the top of the low velocity channel).

$$\ln R(a,b) = \frac{1}{b-a} \int_a^b \ln s(\eta) d\eta$$

where $a \leq p \leq b$ is the averaging interval and, as defined earlier, $s(\eta)$ is the radius at which a ray, with ray parameter q , turns. We recall that (equation (2.7)),

$$\ln \frac{s(q)}{r_o} = -I^{(o)}(q) - \sum_{k=1}^K I^{(k)}(q),$$

and thus

$$\ln \frac{R(a,b)}{r_o} = -\frac{1}{b-a} \int_a^b \{I^{(o)}(q) + \sum_{k=1}^K I^{(k)}(q)\} dq.$$

The first term on the right hand side becomes, on substitution for $I^{(o)}(q)$ and reversing the order of integration :-

$$\begin{aligned} & \int_b^a \Delta(p) \left\{ \cos^{-1} \frac{a}{p} - \cos^{-1} \frac{b}{p} \right\} dp + \int_a^b \Delta(p) \cos^{-1} \frac{a}{p} dp \\ &= \int_a^b \Delta(p) \phi(p, a, b) dp. \end{aligned}$$

where

$$\phi(p, a, b) = \begin{cases} \cos^{-1} \frac{a}{p} - \cos^{-1} \frac{b}{p} & b < p < r_o \\ \cos^{-1} \frac{a}{p} & a < p < b \end{cases}$$

(as shown in fig. 2.8).

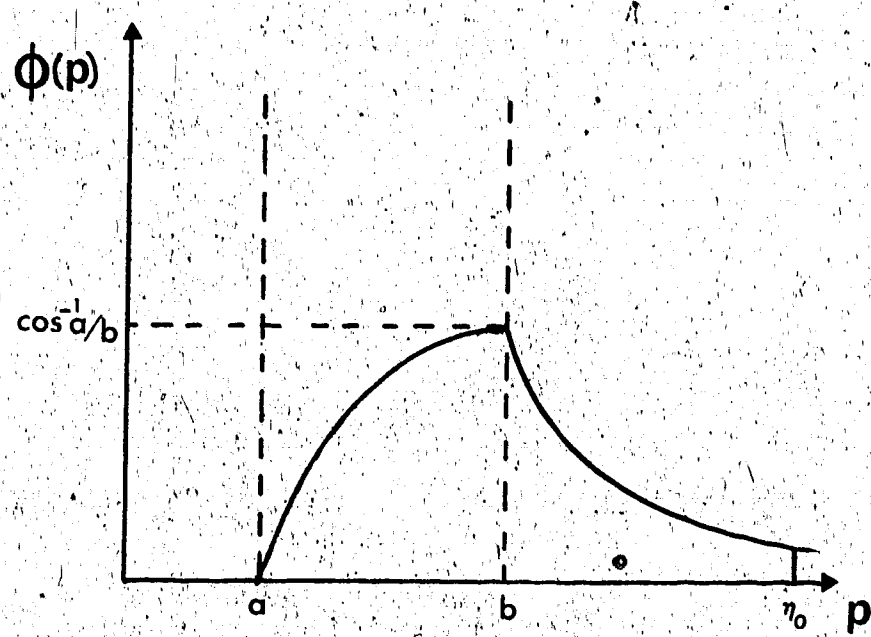


Fig. 2.8. The function $\phi(p)$ defined in the equation
for an averaged radius.

Hence

$$\ln \frac{R(a,b)}{r_0} = -\frac{1}{b-a} \left(\int_a^b \Delta(p) \phi(p, a, b) dp + \int_a^b \sum_{k=1}^K q I^{(k)}(q) dq \right).$$

Bessonova et al (1970) introduced this average to avoid the numerical instabilities of solutions including low velocity channels. However, it will be used here in the interpretation of discrete data. This problem will be looked at in the next chapter. The envelope of all models defined by $I_{\max}^{(o)}(q)$ and $I_{\min}^{(o)}(q)$ will be discussed, as will the maximum and minimum average models defined by $R_{\max}(a,b)$ and $R_{\min}(a,b)$. The former is actually a special case of the latter with $a = b$, where (a,b) may be thought of as a resolving window.

CHAPTER 3

DISCRETE DATA

In reality, rather than an infinite amount of data, there will only be a finite number of data points, assumed to be part of a continuous function. In this chapter, it will be shown that even though the condition of knowing a complete T- Δ curve is not met, it is still possible to use Herglotz-Wiechert inversion techniques and obtain a set of velocity-depth profiles which satisfy the data.

First, extremal velocity-depth profiles will be calculated for the forward branch of T- Δ curves only, where $dp/d\Delta \leq 0$. Regions of low velocity gradient will be discussed in the next chapter and reversal regions, which have been considered by McMechan and Wiggins (1972), will be reviewed in Chapter 5.

The most highly constrained case to consider is when phase velocity (p) as well as travel time data is known. That is $T_i = T(\Delta_i)$, $u_i = p(\Delta_i)$ are exactly known for certain stations Δ_i , $i \geq 1, \dots$, where it is assumed that $T_1 = 0$, $\Delta_1 = 0$ and data are arranged in increasing order.

Though information is only obtained for a finite number of points, the condition that the gradient of

$T = T(\Delta)$ must be a monotonically decreasing function of range provides a further restriction. That is, for the linear interpolation gradient m , $m_{i+1} < m_i < m_{i-1}$, where

$$m_i = \frac{T_{i+1} - T_i}{\Delta_{i+1} - \Delta_i} = \frac{\delta T_i}{\delta \Delta_i}$$

For (p, T, Δ) data, the upper and lower limits on p may be further reduced, as m_i represents an averaged value of ray parameter p between (T_i, Δ_i) and (T_{i+1}, Δ_{i+1}) while u_i and u_{i+1} are the p values at (T_i, Δ_i) and (T_{i+1}, Δ_{i+1}) respectively and therefore, as $dp/d\Delta \leq 0$, $u_i < m_i < u_{i+1}$.

The constraints on the data may be summarised as

$$(1) \quad u_{i+1} \leq p \leq u_i \quad \text{for } \Delta_i < \Delta < \Delta_{i+1}$$

$$(2) \quad p = u_i \quad \text{for } \Delta = \Delta_i$$

$$(3) \quad \frac{dp}{d\Delta} \leq 0$$

$$(4) \quad \int_0^{\Delta} p d\Delta = T$$

Equation (4) may then be modified to

$$\int_{\Delta_i}^{\Delta_{i+1}} p d\Delta = T_{i+1} - T_i = \delta T_i$$

Constraints (1) and (2) state that in the $p-\Delta$ plane any valid p model must lie within independent box structures as illustrated in fig. 3.1 which indicates an arbitrary p curve and the bounds on any p model in the $p-\Delta$ plane.

The problem then becomes that of determining the maximum and minimum $I^{(o)}(q)$ (as defined in equation 2.7) subject to the above constraints. Obviously, the simplest way to maximise the integral is with $p = u_i$. However condition (4) would not then be valid and in fact will only be met if p is evenly distributed about the mean, m_i .

$$I^{(o)}(q) = \int_0^{\Delta(q)} \cosh^{-1} \frac{p}{q} d\Delta$$

and

$$\frac{d^2}{dp^2} \cosh^{-1} \frac{p}{q} < 0.$$

Thus any small perturbation of p , δp , from $p = m_i$ will result in a decrease in the total area of the interval as indicated by fig. 3.2. So for $p = m_i$ the integral

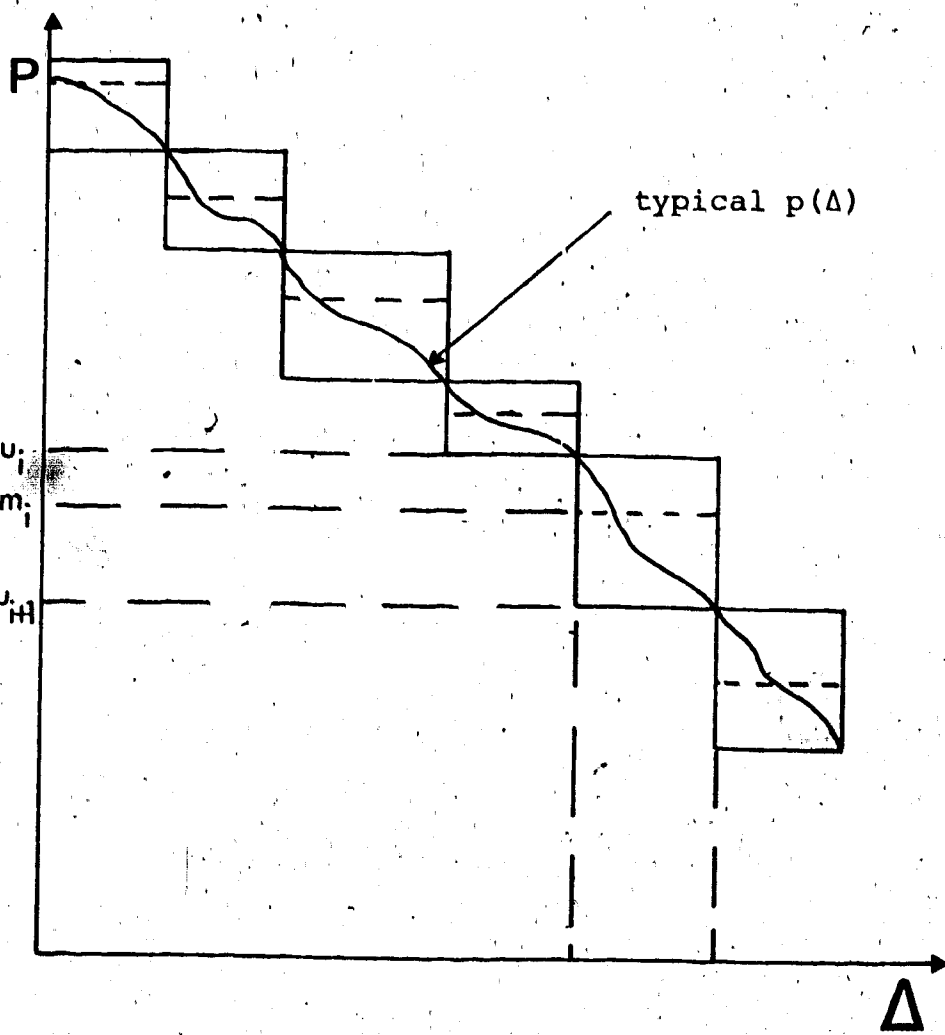


Fig. 3.1. The bounds on any model for (p, T, Δ) data in the $p-\Delta$ plane (i.e. ray parameter in sec/deg versus range in degs). An arbitrary $p(\Delta)$ curve is also shown, where, to satisfy the data, the curve must always be within the bounds.

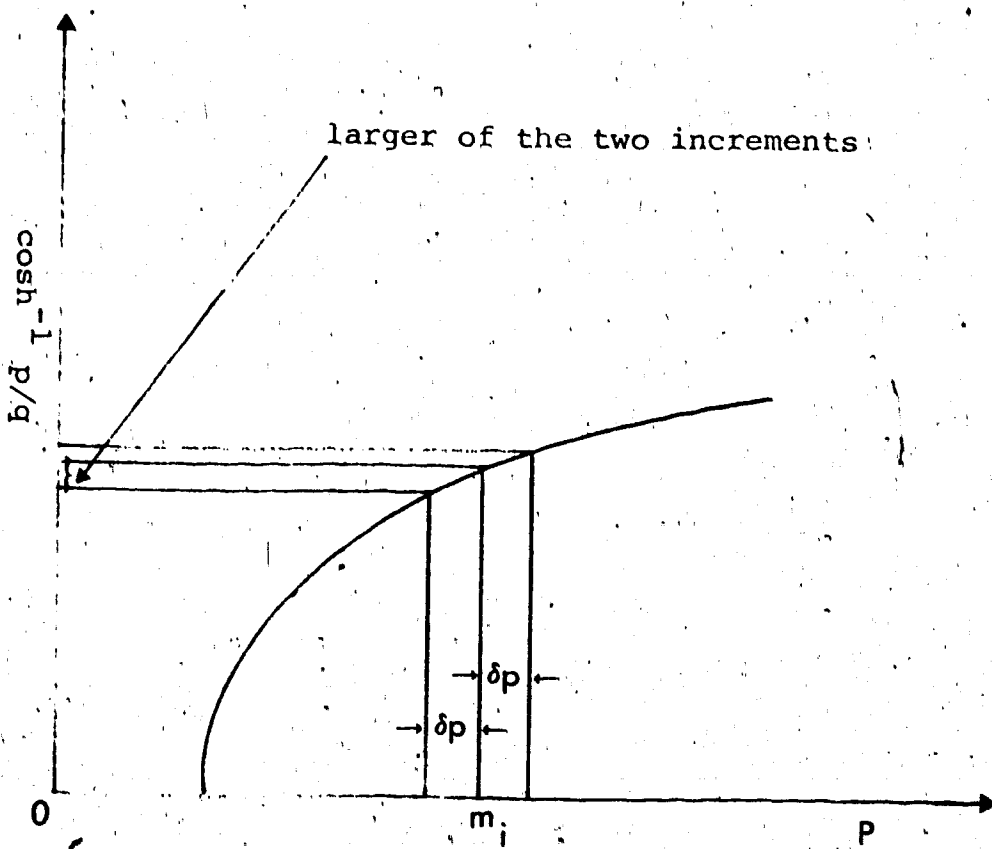


Fig. 3.2. A sketch of $\cosh^{-1} p/q$ as a function of p , showing that any small perturbation, δp , away from the mean m_i , will result in a decrease in the value of $I^{(c)}(q)$.

will be the global maximum as shown in fig. 3.3. However, the end points must be considered separately.

The end point $\Delta(0)$ is quite straightforward as $p = m_1$ will produce the maximum, as in the general interval.

At $\Delta(q)$, the integral will be maximised by taking $p = m_j^*$ in the interval containing $p = q$, and, beyond $\Delta(q)$, by taking p equal to its minimising value. The relationship between $\Delta(q)$ and m_j^* is found by the following equation, which satisfies condition (4),

$$\int_{\Delta_j}^{\Delta(q)} m_j^* dp + \int_{\Delta(p)}^{\Delta_{j+1}} u_{j+1} dp = \delta T_j$$

i.e.

$$\Delta(q) = \frac{\delta T_j + m_j^* \Delta_j - u_{j+1} \Delta_{j+1}}{m_j^* - u_{j+1}}$$

As can be seen from fig. 3.4, the value of m_j^* will be dependent on the value of q , and as $\Delta_j \leq \Delta(q) \leq \Delta_{j+1}$, m_j^* is constrained above and below to u_j and m_j respectively. Hence, for all q , m_j^* must be found such that

for $m_j \leq m_j^* \leq u_j$

$$(i) \quad \frac{\partial I_j}{\partial m_j^*} = 0$$

$$\Delta_j \leq \Delta(q) \leq \Delta_{j+1}$$

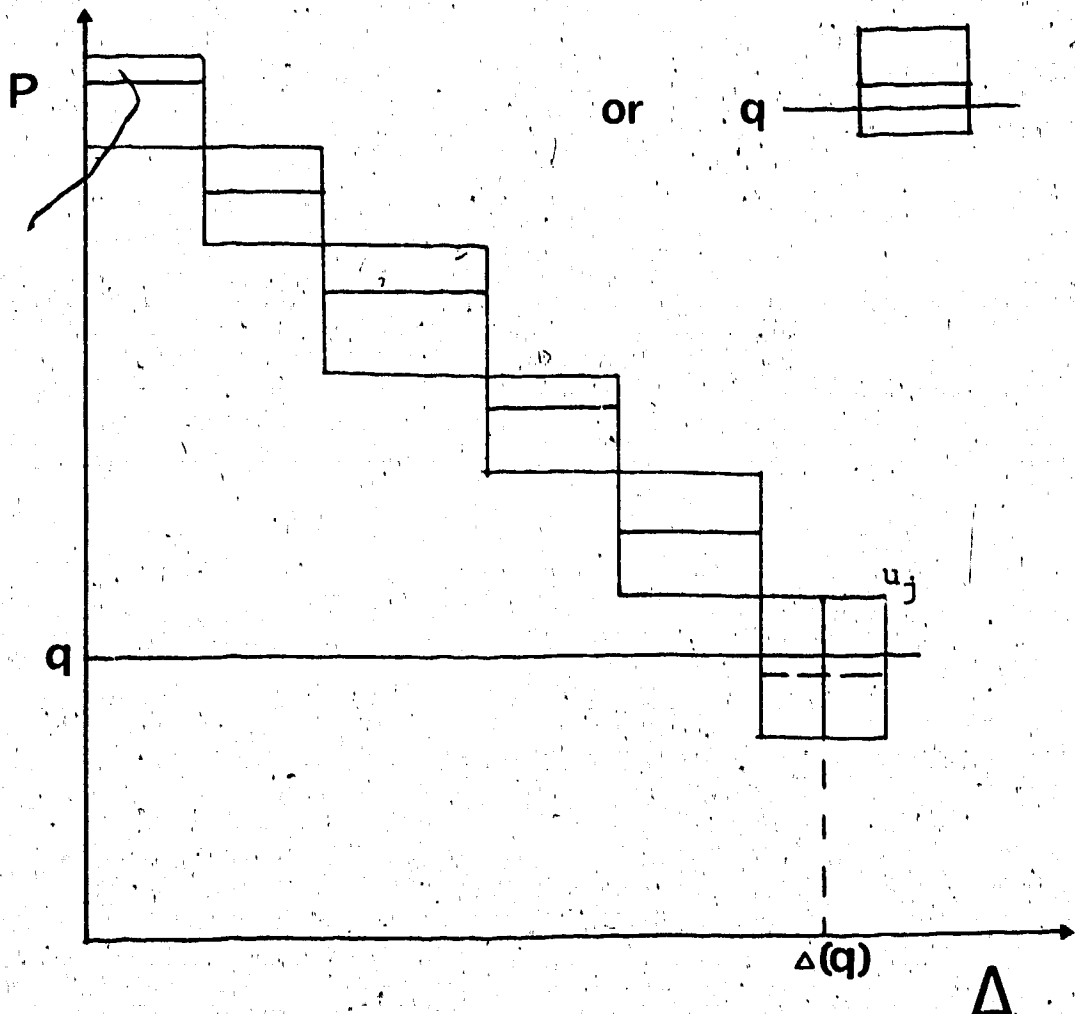


Fig. 3.3. The $p(\Delta)$ curve, in the $p\Delta$ plane, which will maximise $I^{(o)}(q)$ where the inset refers to the change in end point if $q < m_j$. The unconstrained end point would be similar to that shown in the main diagram but with $p = m_j^*$ rather than u_j .

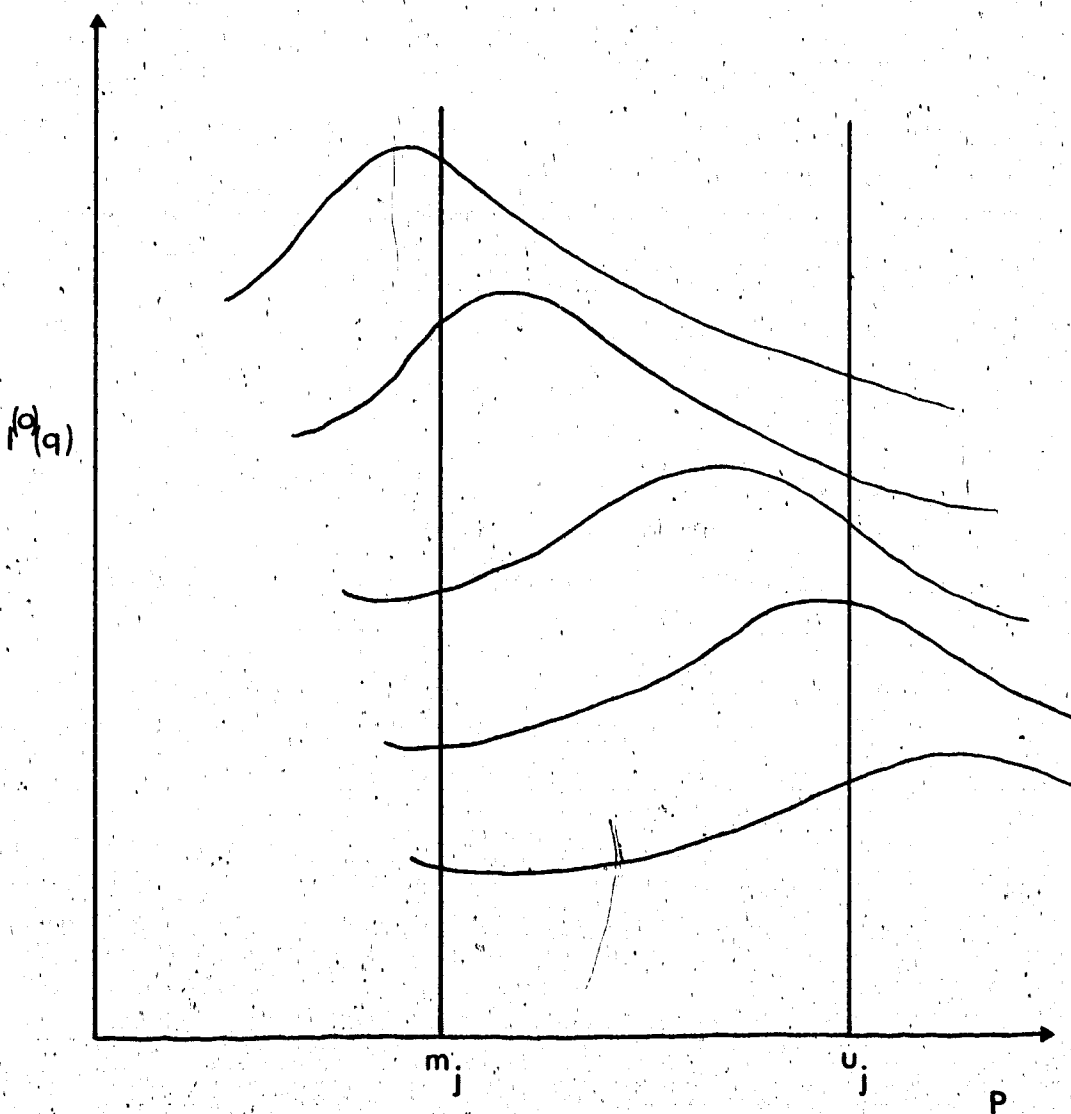


Fig. 3.4. Sketch of a family of $I^{(o)}(q)$ curves, where $I^{(o)}(q)$ decreases as a function of increasing q . Hence the value of m_j^* will depend on q and may be constrained to u_j or m_j .

For $(\partial I_j / \partial m_j^*)_{m_j^*=m_j} < 0$, the constrained maximum is at $p = m_j$ and for $(\partial I_j / \partial m_j^*)_{m_j^*=u_{j+1}} > 0$, the constrained maximum is at $p = u_{j+1}$.

To maximise $I^{(o)}(q)$, it is necessary to perturb p from the mean by as much as possible, say to

$$p = \begin{cases} \hat{p}_i & \Delta_i \leq \Delta < \theta_i \\ \bar{p}_i & \theta_i \leq \Delta < \Delta_{i+1} \end{cases}$$

where θ_i is determined by condition (4). However from constraint (3), there can be no discontinuous increase in p at Δ_i , and therefore

$$\hat{p}_j = u_j$$

$$\bar{p}_j = u_{j+1}$$

and

$$\theta_j = \frac{\delta T_j + u_j \Delta_j - u_{j+1} \Delta_{j+1}}{u_j - u_{j+1}}$$

so that

$$I_j = (\theta_j - \theta_{j-1}) \cosh^{-1} \frac{u_j}{q}$$

as shown in fig. 3.5, a $p-\Delta$ plot of the band of possible models where the solid $p(\Delta)$ curve through the bands is

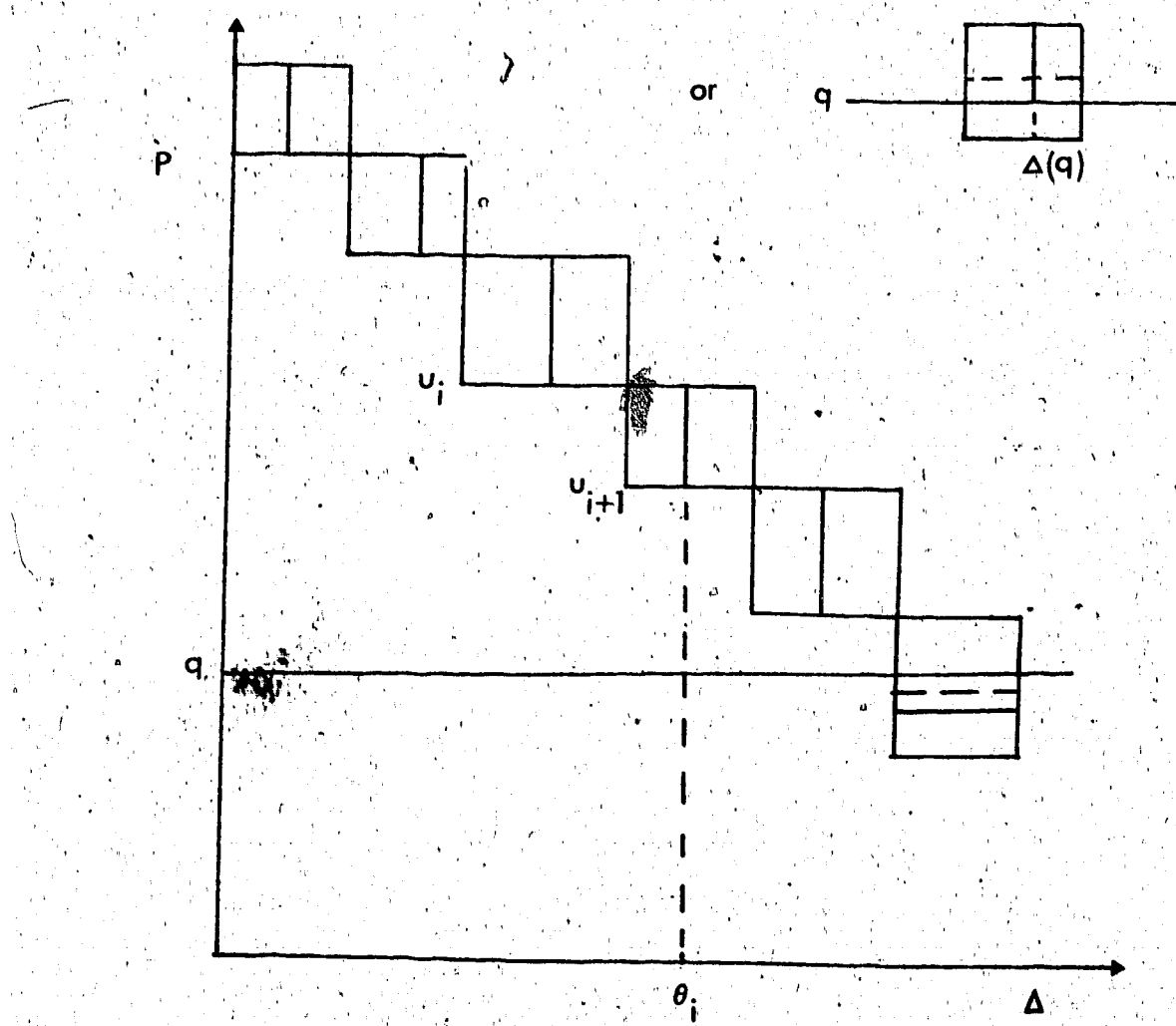


Fig. 3.5. A plot in the $p-\Delta$ plane of the band of possible $p(\Delta)$ curves where the solid line through the boxes is the $p(\Delta)$ curve which minimises $I^{(o)}(q)$. The inset refers to the alternative end point value if $q < m_j$.

that which gives the minimum integral.

The end points must again be considered separately.

For $\Delta(0)$ there are two cases:

(i) $u_1 = \infty$ (i.e. no surface velocity constraints)

then

$$I_1 = (\theta_1 - \Delta_1) \cosh^{-1} \frac{u_2}{q}$$

(ii) $u_1 \neq \infty$

then

$$I_1 = (\theta_1 - \Delta_1) \cosh^{-1} \frac{u_1}{q} \quad (\text{fig. 3.5})$$

At $\Delta(q)$, the global minimum will be

$$p = \begin{cases} u_j & \Delta_j \leq \Delta < \Delta(q) \\ q & \Delta(q) \leq \Delta < \Delta_{j+1} \end{cases}$$

where, to satisfy (4)

$$\Delta(q) = \frac{\delta T_j + u_j \Delta_j - q \Delta_{j+1}}{u_j - q}$$

as illustrated in the inset of fig. 3.5. However, if the condition $\Delta_j < \Delta(q)$ is to be met, then

$$q < \frac{\delta T_j}{\delta \Delta_j} = m_j$$

Thus, for $m_j \leq q < u_j$, the integral I_j must be constrained to zero, as shown in fig. 3.5.

Using these conditions on maximisation and minimisation a program was written to find extremal velocity depth models for given (p, T, Δ) data. Test data (from the Herrin tables) was used to determine a number of effects. First, the sampling interval was varied between approximately 1, 3 and 5 degrees for this standard data and extremal profiles were calculated for $9.0 \leq q \leq 10.0$ at 0.1 sec/deg intervals of q (this corresponds to a radius range of about 5600 to 5800 km). As can be seen from fig. 3.6, decreasing the sampling interval decreases the width of the velocity-radius envelope. This is as expected as in the limit of continuous data the velocity depth profile would be unique.

Tests were also made on the effects of errors in T and Δ measurements but the results of this were inconclusive and have not therefore been presented. Any meaningful results from this type of experiment would require systematic variation of both T , Δ and p measurements (both dependent and independent variations) over different interval lengths and at different points in the data set.

The model was also fixed to different depths and the resulting profiles compared. That is first no assumptions were made about the earth's internal structure,

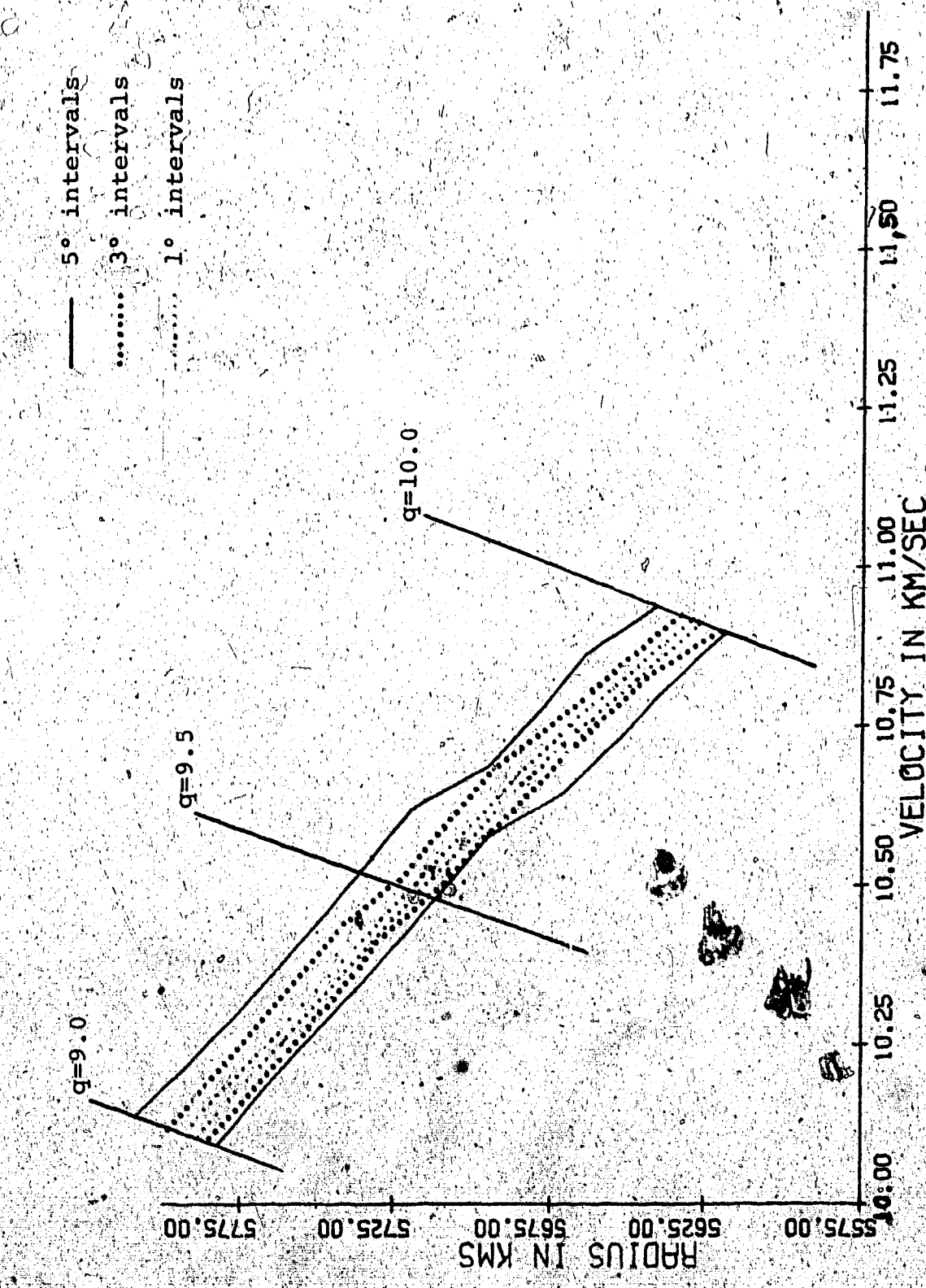


Fig. 3-6. Radius-velocity plot to show the effect of decreasing the sampling width from 5° to 3° and 1° . The range of q values used is also indicated.

only that its surface radius was 6371 km, and using the standard data the velocity-depth envelope for the crust and mantle was computed, as shown in fig. 3.7. It was then assumed that velocity was known as a function of radius in the crust so that to a depth of about 50 km (i.e. radius at 6322 km) the velocity-depth profile from the inversion procedure is unique. Below that, a series of profiles is again possible and an envelope of profiles is obtained. Thirdly, the model is fixed to a depth of approximately 850 km (i.e. it is assumed that the structure of the upper mantle is also known). The last two cases have been superimposed on the radius-velocity diagram of the first case, as is shown in fig. 3.7. It should be noted from the diagram that the effect of fixing any part of the profile only reduces the width of the envelope in the immediate vicinity of the known part of the profile. Thus even knowing the structure of the upper mantle the band of possible velocities for given radius close to the bottom of the mantle remains unaffected. This is also the conclusion drawn by Wiggins et al (1973) though their method of inversion is different and uses few time constraints. However the data used here is meant only to illustrate the theory and may not, therefore, be compared too critically with the results of Wiggins et al.

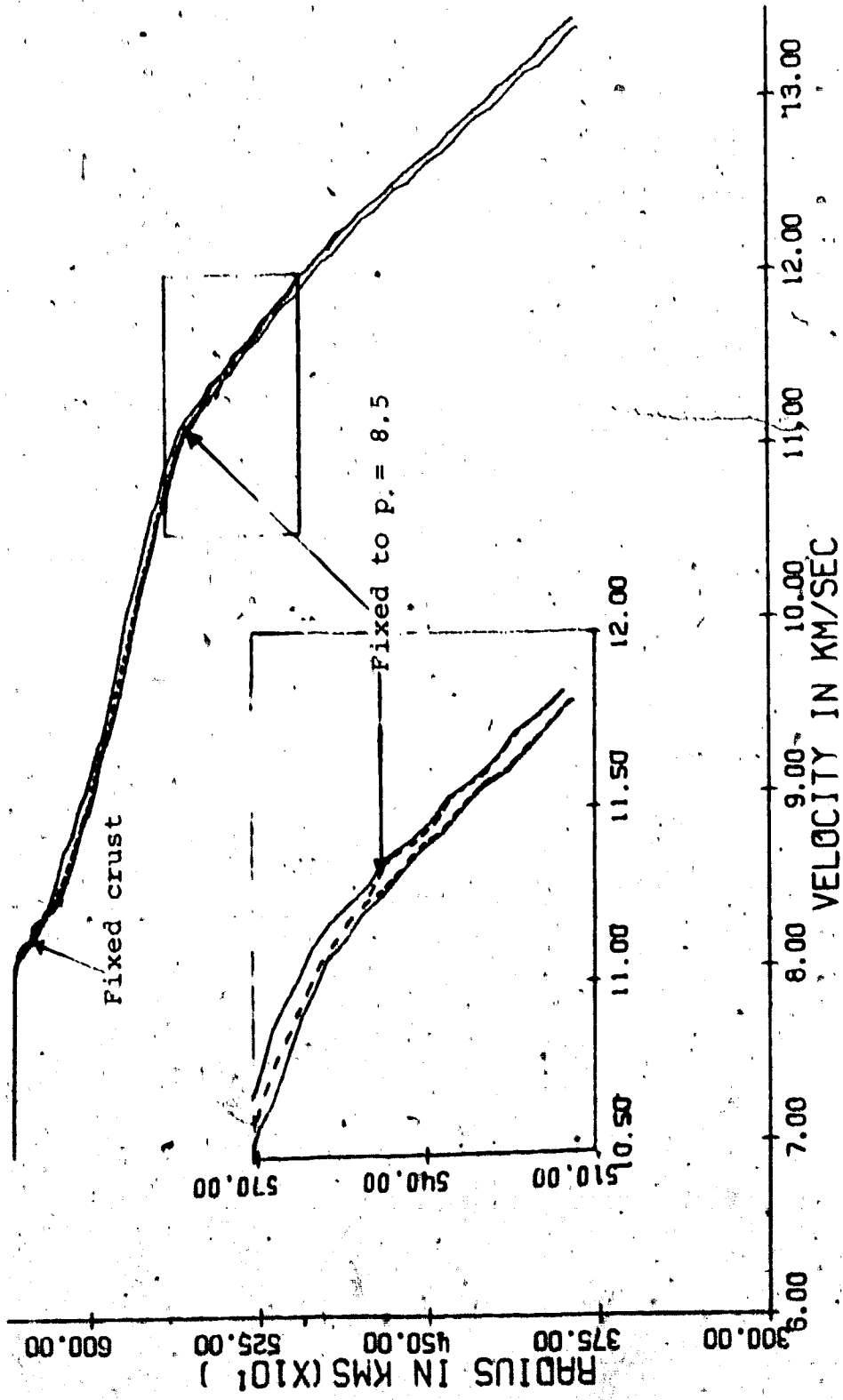


Fig. 3.7. Radius-velocity plot for (p, T, Δ) data with the effect of fixing part of the model indicated by broken lines.

It is also of interest to note the behaviour of individual profiles as they move away from the extremal curves. It should be remembered that a function of $p(\Delta)$ which will maximise the integral, $I^{(o)}(q)$, for one value of q , say q_{\max} will not do so for other q values (i.e. for other rays). In fact the way in which the $v(r)$ profile moves away from the envelope edge (in this case the minimum curve) will depend on the position of q_{\max} with respect to the p parameters at the end point.

For example, if at the end point $m_j^* = u_j$ for $q = q_{\max}$ (and $p = m_i$ for all other intervals) then for

$q_{\max} \leq q \leq m_{j-1}$ these values of p will also be the maximum ones so that the model will be on the envelope

for $q_{\max} \leq q \leq m_{j-1}$. The system is also oscillatory as the same conditions will be met (i.e. the given values of p will be those providing the maximum integral) for

$u_{i+1} \leq q \leq m_i$ for all $i < j$. Similarly, if for $q = q_{\max}$ $m_j^* = m_j$, then this set of p values will be the maximal

set for $u_{j+1} \leq q \leq m_j$ and for $u_{i+1} \leq q \leq m_i$, $i < j$.

If $m_j < m_j^* < u_j$, then this function of $p(\Delta)$ will only give the maximum integral for $u_{i+1} \leq q \leq m_i$, $i < j$.

Obviously then, the individual characteristics of the $v(r)$ curves will depend on the distribution of data with respect to the values of q taken. Computations were made with the same sample data as used before,

with the profiles fixed to a depth of 1325 km. In fig. 3.8 only a small section of the total profile is illustrated (i.e. $6.0 \leq q_{\max} \leq 6.8$) so that the detailed characteristics may be observed. These individual curves do show the above properties. For example, at $q_{\max} = 6.1$, $m_j < m_j^* < u_j$ and the curve moves away from the minimum quite fast but returns at $q = 6.3$ and 6.6 (which correspond to $u_{i+1} \leq q \leq m_i$ for $i = j-1$ and $j-2$).

The individual curves of fig. 3.8 are possible velocity models which, though they do touch the extremal curves at certain points, in general lie within the envelope. The extremal curves (which are not themselves possible models) represent the largest range of velocities at any one depth which the given data will allow. Hence, it is unreasonable to compare these extremal envelopes with results obtained by Gilbert and Backus inversion (Johnson and Gilbert 1972), as has been done by Wiggins et al (1973), because the envelope from this method of inversion will obviously be broader than the averaged uncertainties from other techniques. In order to compare uncertainties in this method with those of other inversion methods, it is necessary to use an averaged radius, as defined by Bessonova et al (1970).

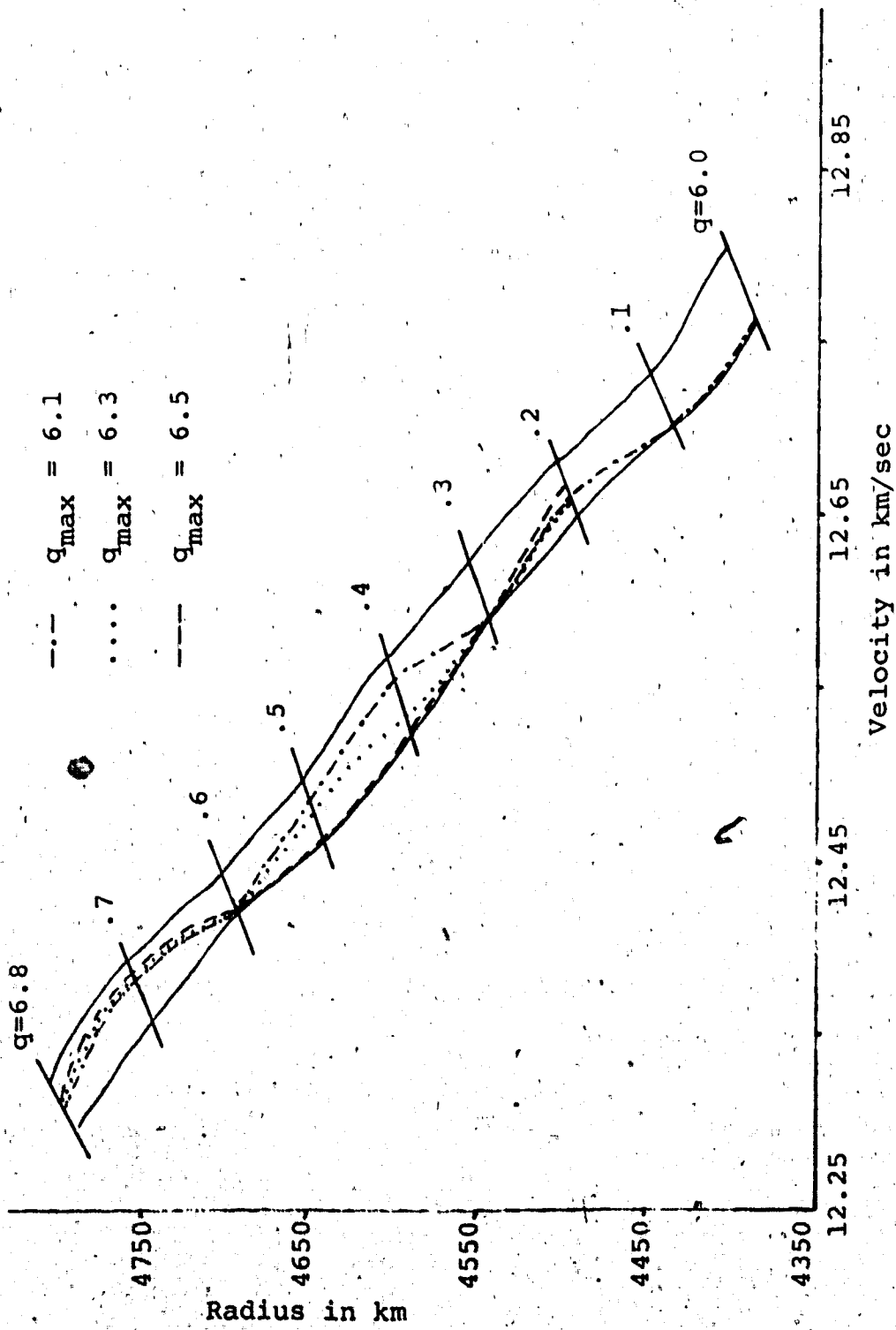


Fig. 3.8. A radius-velocity plot with the envelope of profiles represented by the solid lines and three individual profiles, which are also the extremal profiles for $q = q_{\max}$, represented by broken lines. The lines across the envelope are the values of q , as shown.

This averaged radius, given by equation (2.8), is

$$\ln R(p,a,b) = \frac{1}{b-a} \int_a^b \ln s(q) dq$$

where averaging is from $p = b$ to $p = a$. Obviously for $b = a$, the averaged radius is $R(b,b)$ and the extremal radii $R_{\max}(b,b)$ and $R_{\min}(b,b)$ are as discussed above (i.e. equal $s_{\max}(b)$ and $s_{\min}(b)$). For the case under consideration, that is no low velocity zone existence,

$$\begin{aligned} \ln R(p,a,b) &= - \frac{r_o}{b-a} \int_a^{r_o} \Delta(p) \phi(p,a,b) dp \\ &= - \frac{r_o}{b-a} \sum_i I_i \end{aligned} \quad (2.9)$$

where

$$\phi(p,a,b) = \begin{cases} \cos^{-1} \frac{a}{p} - \cos^{-1} \frac{b}{p} & b < p < r_o \\ \cos^{-1} \frac{a}{p} & a < p \leq b \end{cases}$$

To find the extrema of $R(p,a,b)$ it is necessary to consider the extrema of $\phi(p,a,b)\Delta(p)$.

In general, $d\phi/dp < 0$ is required, so that any perturbation, δp , away from the mean, $p = m_i$, will decrease the total area under the (p) curve for that

interval. Similarly, for $b < p < n_0$, $d\phi/dp < 0$ and, as can be seen from fig. 3.9, a perturbation, δp , from the mean value of p (i.e. m_i) will also decrease the area under the $\phi(p)$ curve for the i^{th} interval. Therefore, for $b < p < n$, $p = m_i$ will maximise $\phi(p) \Delta(p)$ in the i^{th} interval. However, for $a < p < b$, $d\phi/dp > 0$ so that, as shown in fig. 3.9, a perturbation δp from $p = m_j$ will increase the area under the $\phi(p)$ curve for that interval. This conflicts with the effect on $\Delta(p)$ of perturbing p . For the data considered, the possible variation in $\Delta(p)$ (i.e. from Δ_j to Δ_{j+1}) is smaller than that in $\phi(p)$, which varies quite rapidly, so that the maximum possible perturbation of p from $p = m_j$ which satisfies the travel time constraints, will maximise the integral for $a < p < b$. In the case of (p, T, Δ) data, this means that

$$p = \begin{cases} u_j & \Delta_j < \Delta < \theta_j \\ u_{j+1} & \theta_j < \Delta < \Delta_{j+1} \end{cases}$$

where

$$\theta_j = \frac{\delta T_j + u_j \Delta_j - u_{j+1} \Delta_{j+1}}{u_j - u_{j+1}}$$

(as shown in fig. 3.10).

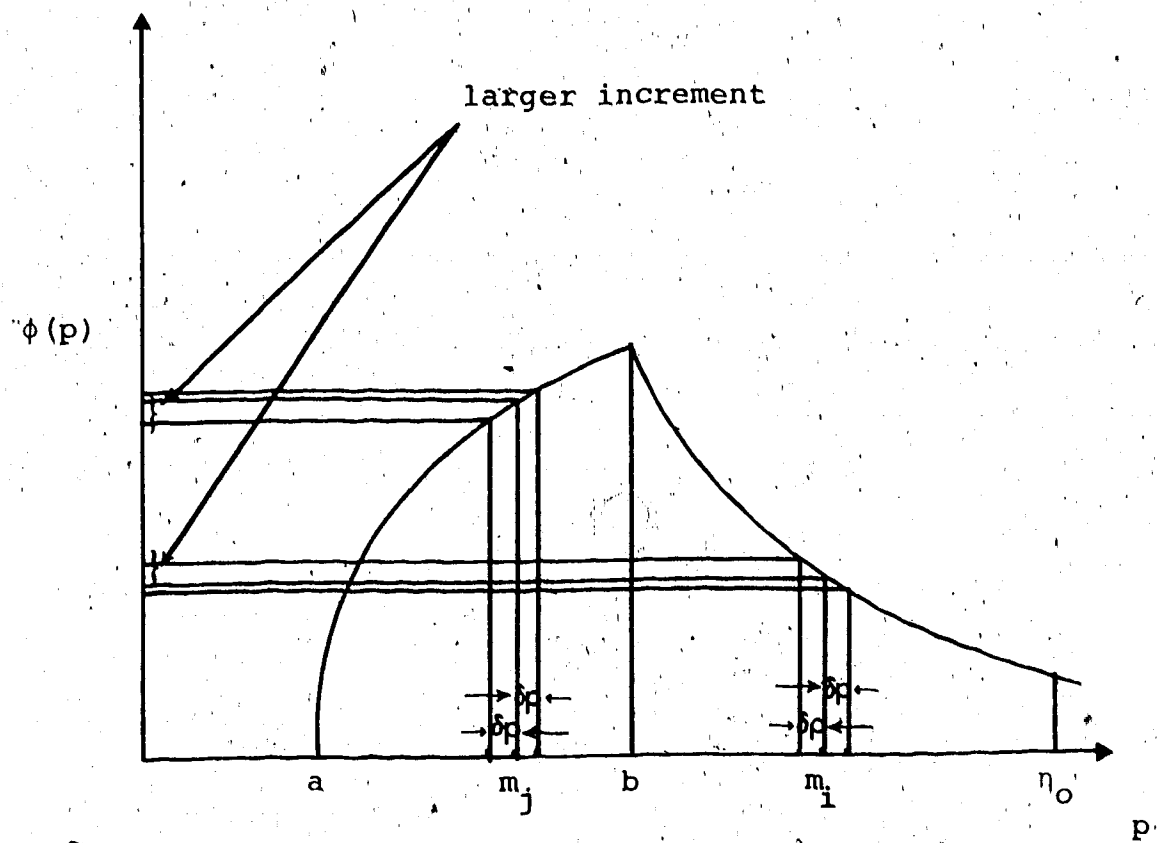


Fig. 3.9. A graph of $\phi(p)$, the averaging function defined by equation (2.9). For $b < p < n_o$, a perturbation δp from the mean, $p = m_i$, will result in a decrease in the area under the $\phi(p)$ curve. For $a < p < b$, a perturbation δp from $p = m_j$ will result in an increase in the area under the $\phi(p)$ curve.

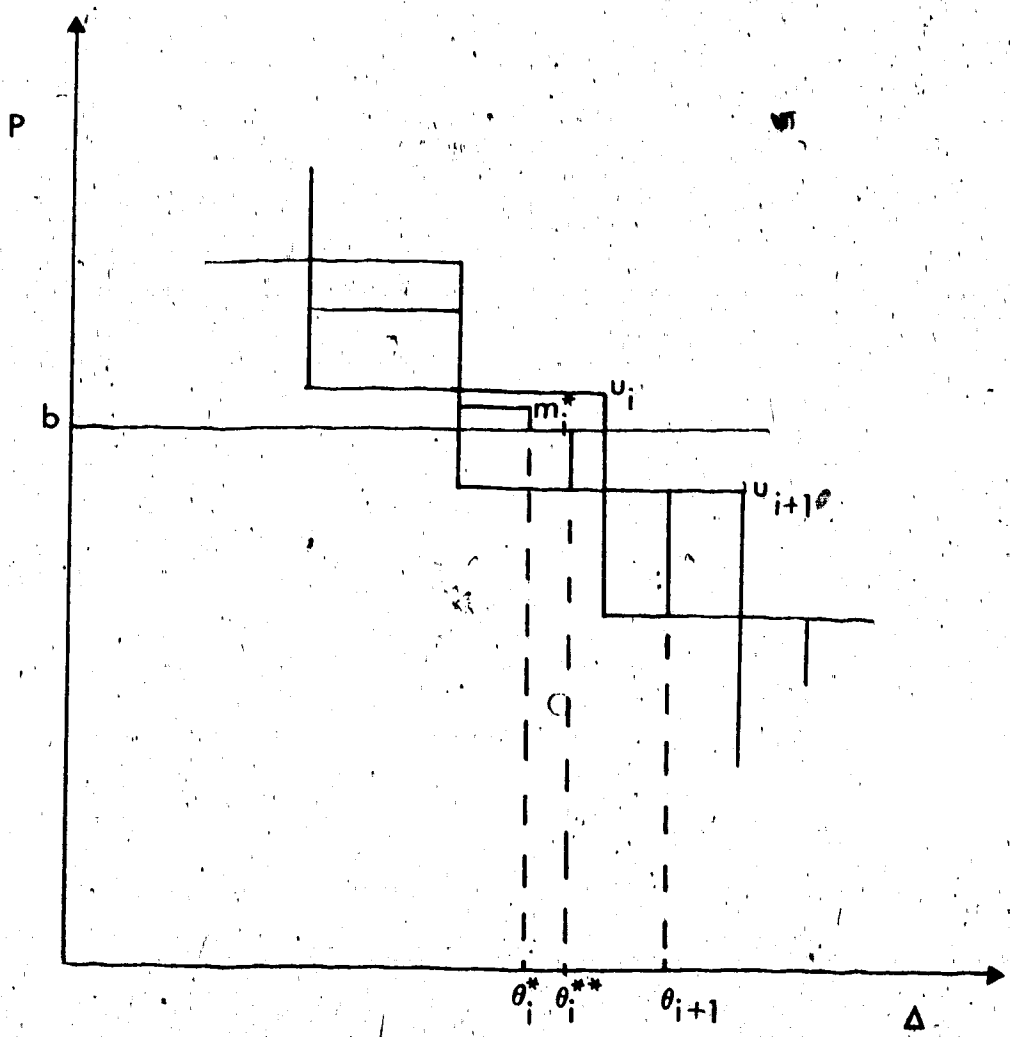


Fig. 3.10. The values of $p(\Delta)$ about the point $p = b$ which will, in general, maximise the integral, are represented by the solid lines through the boxes.

Conversely, for $b < p < n_0$, the largest possible perturbation of δp from the mean will minimise $\phi(p)\Delta(p)$ so that the minimising values of p are

$$p = \begin{cases} u_i & \Delta_i < \Delta < \theta_i \\ u_{i+1} & \theta_i < \Delta < \Delta_{i+1} \end{cases}$$

For $a < p < b$, the effect on $\phi(p)$ will predominate so that $p = m_j$ will minimise the integral in the j^{th} interval.

As before, the end points must be considered separately. For both cases, $\Delta(0)$ is treated as for $s_{\max}(q)$ and $s_{\min}(q)$. If $u_{i+1} \leq b \leq u_i$ and $a > u_{i+1}$ then $\Delta(a)$ is also the same as the end point $\Delta(q)$ in the previous discussions. The most general maximisation of the integral is as shown in fig. 3.10 where $\Delta(b)$ corresponds to $\Delta(q)$ for $b < p < n_0$ and $\Delta(0)$ for $a < p < b$. However, this contribution may be further increased by decreasing m_i^* and increasing θ_i^{**} until in the limit $\theta_i^{**} = \theta_i^*$. The relationship between θ_i^* and m_i^* is found from the travel time constraint on the interval:-

$$\delta T_i = m_i^*(\theta_i^* - \Delta_i) + u_{i+1}(\Delta_{i+1} - \theta_i^*) \quad (3.1)$$

and then, as

$$I_i = \Delta_i \int_{m_i^*}^{u_i} \phi(p) dp + \theta_i^* \int_{u_{i+1}}^{m_i^*} \phi(p) dp \quad (3.2)$$

m_i^* may be determined numerically by substituting θ_i^* from

(3.1) into equation (3.2) and then using the condition

$\partial I_i / \partial m_i^* = 0$. Both θ_i^* and m_i^* are subject to further constraints:

$$(1) \quad b \leq m_i^* \leq u_i$$

$$(2) \quad \Delta_i \leq \theta_i^* \leq \Delta_{i+1}$$

The right hand equality of constraint (2) sets $m_i^* = m_i$,

$\theta_i^* = \Delta_{i+1}$ for $m_i \geq b \geq u_{i+1}$. For $u_i \geq b > m_i$ it is

not obvious if $m_i^* = b$ or $m_i^* > b$ will give the absolute maximum. This may be checked numerically. The two limiting cases are:

$$(1) \quad b = u_{i+1} \quad m_i^* = m_i \quad \theta_i^* = \Delta_{i+1}$$

$$(2) \quad b = u_i \quad m_i^* = u_{i-1} \quad \theta_i^* = \theta_i$$

If $a \geq u_{i+1}$ the function will not be deformed

for either range of b , except to alter the value of θ_i^*

for $u_i \geq b > m_i$ to

$$\theta_i^* = \frac{\delta T_i + m_i^* \Delta_i - a \Delta_{i+1}}{m_i^* - a}$$

The general condition for a minimum in the interval containing b is as shown in fig. 3.11 where θ_i^* and m_i^* are determined from

$$\delta T_i = u_i(\theta_i^* - \Delta_i) + m_i^*(\Delta_{i+1} - \theta_i^*) \quad (3.3)$$

and $\partial I_i / \partial m_i^* = 0$, given I_i as in equation (3.2), and the constraints

$$(1) \quad u_{i+1} \leq m_i^* \leq u_i$$

$$(2) \quad \Delta_i \leq \theta_i^* \leq \Delta_{i+1}$$

From the left hand side of (2), $m_i^* = m_i$, $\theta_i^* = \Delta_{i+1}$ for $m_i \leq b \leq u_i$. For $m_i < b \leq u_i$, there are two possible minima, given by $m_i^* = b$ and $m_i^* < b$, as illustrated in

fig. 3.12 with

$$\theta_i^{*(1)} = \frac{\delta T_i + u_i \Delta_i - m_i^* \Delta_{i+1}}{u_i - m_i^*}$$

$$\theta_i^{*(2)} = \frac{\delta T_i + u_i \Delta_i - b \Delta_{i+1}}{u_i - b} < \theta_i^{*(1)}$$

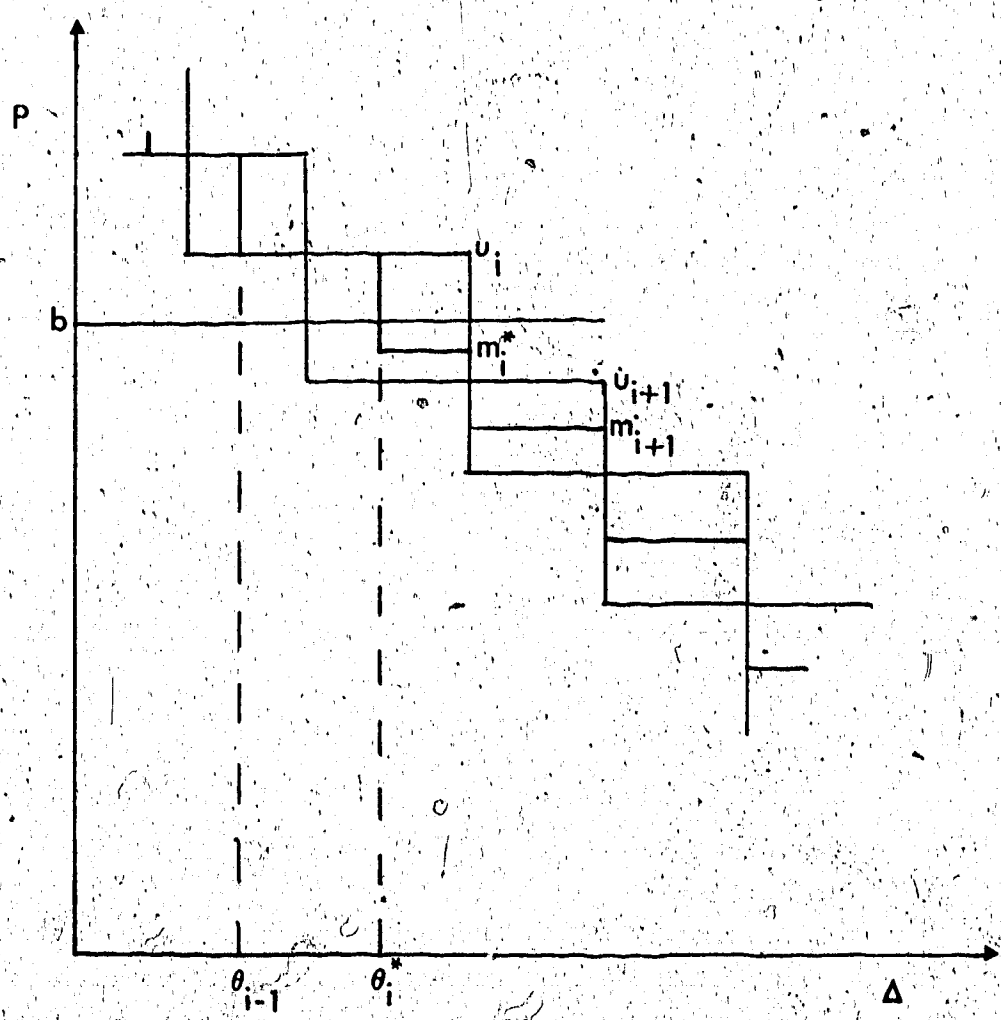


Fig. 3.11. The values of $p(\Delta)$ about the point $p=b$
which will minimise the integral, as
represented by solid lines through the
boxes.

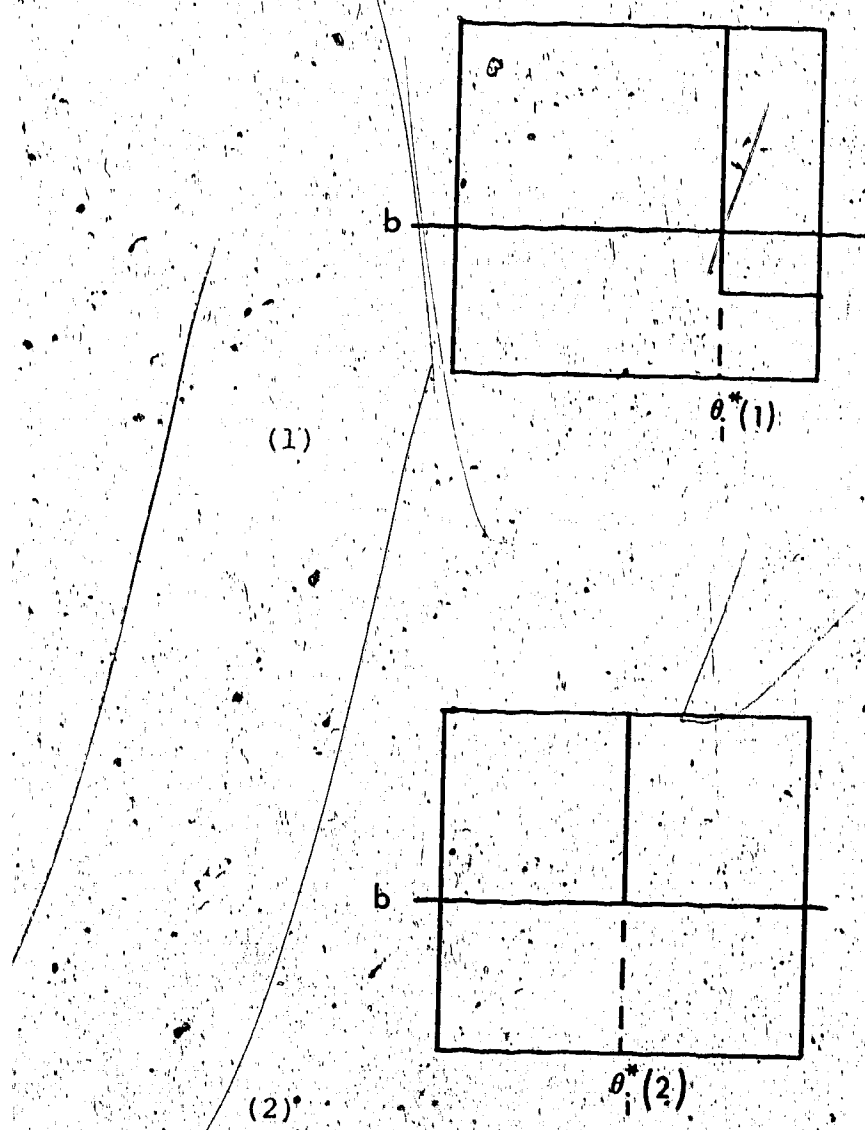


Fig. 3.12. The two possible ways of minimising
the integral about the point $p=b$ as
shown by (1) and (2).

The absolute minimum for this interval can be numerically determined. The two limiting cases are:-

$$(1) \quad b = u_i \quad m_i^* = m_i \quad \theta_i^* = \Delta_i$$

$$(2) \quad b = u_{i+1} \quad m_i^* = a_i \quad \theta_i^* = \theta_i$$

If $a < u_{i+1}$, it will only affect the i^{th} interval if $m_i \leq a < u_i$. Then m_i^* is rather than m_i .

Thus the function $\phi(p, a, b) \Delta(p)$ may be suitably maximised and minimised to obtain the extremal average radii. Using the same model as for the calculations of the maximum and minimum profiles (i.e. $s_{\max}(q)$ and $s_{\min}(q)$) fixed to the same depth maximum and minimum averaged radii ($R_{\max}(a, b)$ and $R_{\min}(a, b)$) were computed for a number of window lengths at fixed η . The values of η were chosen so that the same section of the profile was observed as for the non-extremal profiles of fig.

3.8 (i.e. $6.1 \leq \eta \leq 6.5$) and the window length, $b - a$, was varied from 0.1 to 0.9 sec/deg by 0.1 intervals for each value of η . The values of $R_{\max}(a, b)$ and $R_{\min}(a, b)$ for $a = b$ are $s_{\max}(\eta)$ and $s_{\min}(\eta)$ respectively. The window length was not increased further as at a length of 1.0 sec/deg the averaging is over about 200 km and increasing the length further would cause averaging of

large scale variations and the values obtained would no longer be meaningful.

It should further be noted that the averaging is a logarithmic averaging over a non-linear curve so that the separation of $R_{\max}(a,b)$ and $R_{\min}(a,b)$ will not be a linear function of $b - a$. For example, if on a very steep section of the velocity curve, then the average will be weighted to one end of the averaging interval so that the values of the averaged radii may be higher than the non-averaged values. However if this is the case both maximum and minimum would be weighted in the same way and both should move together.

As with the non-extremal profiles, the position of η with respect to p (and hence of a and b with respect to p) determines the behaviour of the averaged radii in moving away from $s_{\max}(\eta)$ and $s_{\min}(\eta)$, so that if in the non-averaged case a particular profile moves slowly away from the extreme then it is to be expected that in the averaged case, the radii will move slowly away from their values at zero window length (i.e. that their separation decreases slowly as a function of increased window length). This phenomenon may be observed in figs. 3.13 and 3.14 as compared to fig. 3.8. Thus for $q = 6.5$ in fig. 3.8, the $s(q)$ curve moves from the extremal value slowly and, as can be seen from fig. 3.13 (which

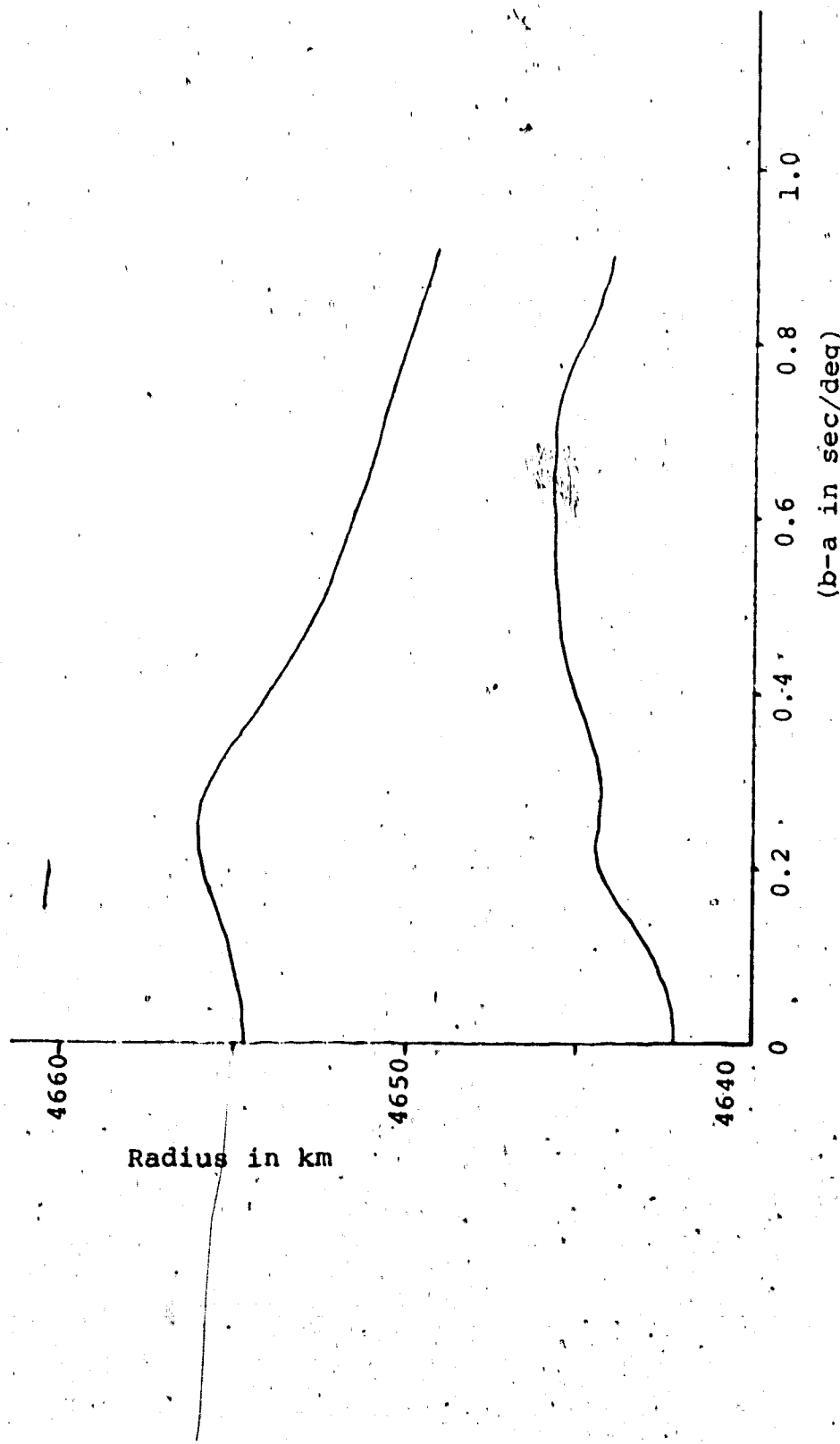


Fig. 3.13. A plot of extremal radius as a function of the averaging window, $(b-a)$, for $\eta = 6.5$ with the model fixed to $p = 7.60 \text{ sec/deg}$.

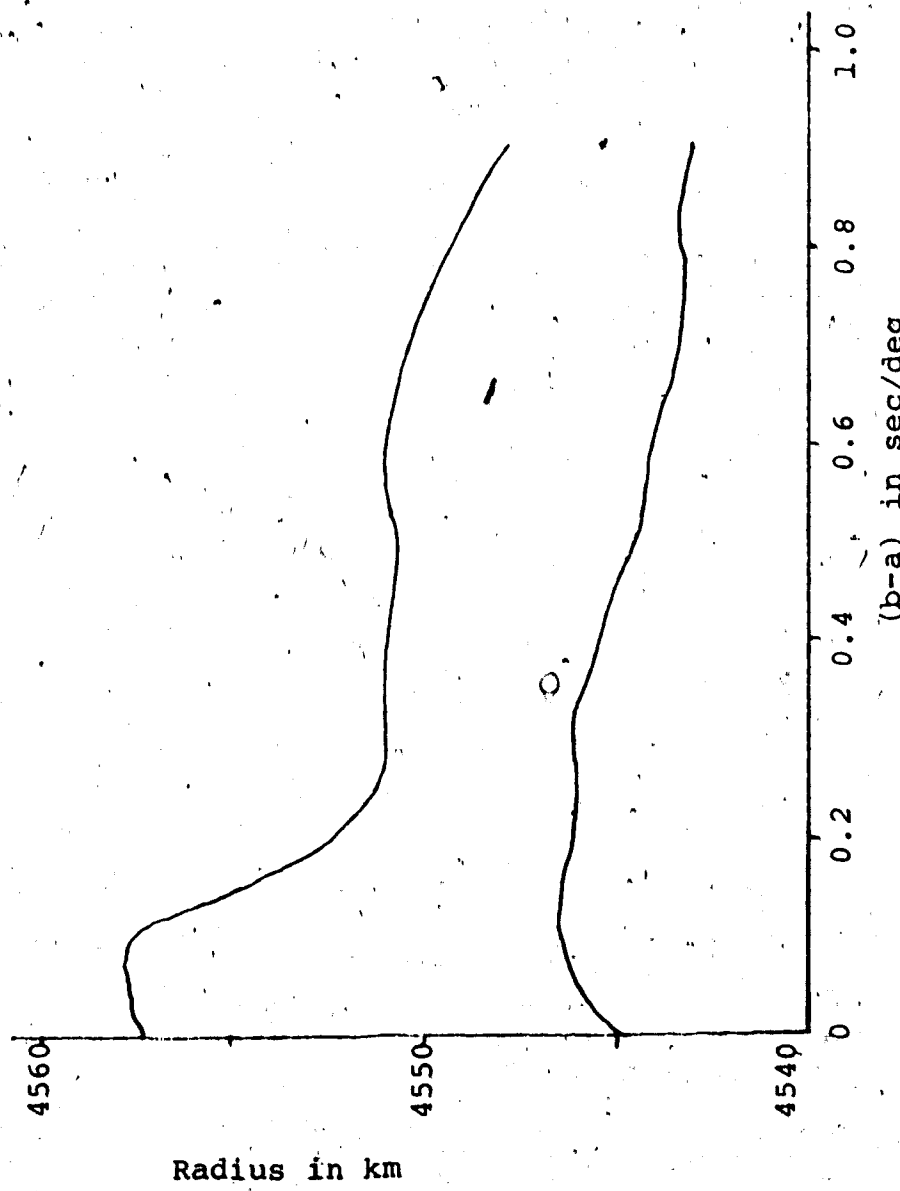


Fig. 3.14. A plot of extremal radius as a function of the averaging window, $(b-a)$, for $\eta = 6.3$ with the model fixed to $p = 7:60$ sec/deg.

is a plot of averaged radius R versus window length, $b - a$ for $\eta = 6.5$) the separation of the averaged radii also decreases slowly with increased averaging length. However, for $\eta = 6.3$ in fig. 3.8, the non-extremal model moves away from the envelope quite quickly and the separation of the averaged radii also decreases quite fast with respect to averaging length, as can be seen from fig. 3.14 which is again a plot of averaged radius R versus averaging length $b - a$ but for $\eta = 6.3$. Though the rate of decrease of envelope width varies for both $\eta = 6.5$ and $\eta = 6.3$ the width of envelope decreases by approximately 40%.

Fig. 3.14 may be plotted in another way as in fig. 3.15 which is a plot of averaged radius against η . Thus for $\eta = 6.3$, the variation in envelope width as a function of averaging length may be represented by a series of error ellipses. Obviously there will be an optimum value of $b - a$ (and hence $R_{\max}(a, b)$ and $R_{\min}(a, b)$), as for large values of $b - a$, though the separation between extremal radii is small, the area of the error ellipse is larger than at some intermediate values. The envelope for $a = b$ has been superimposed on fig. 3.14 and it can be seen that those cases of larger $b - a$ values do not follow the trend of this envelope.

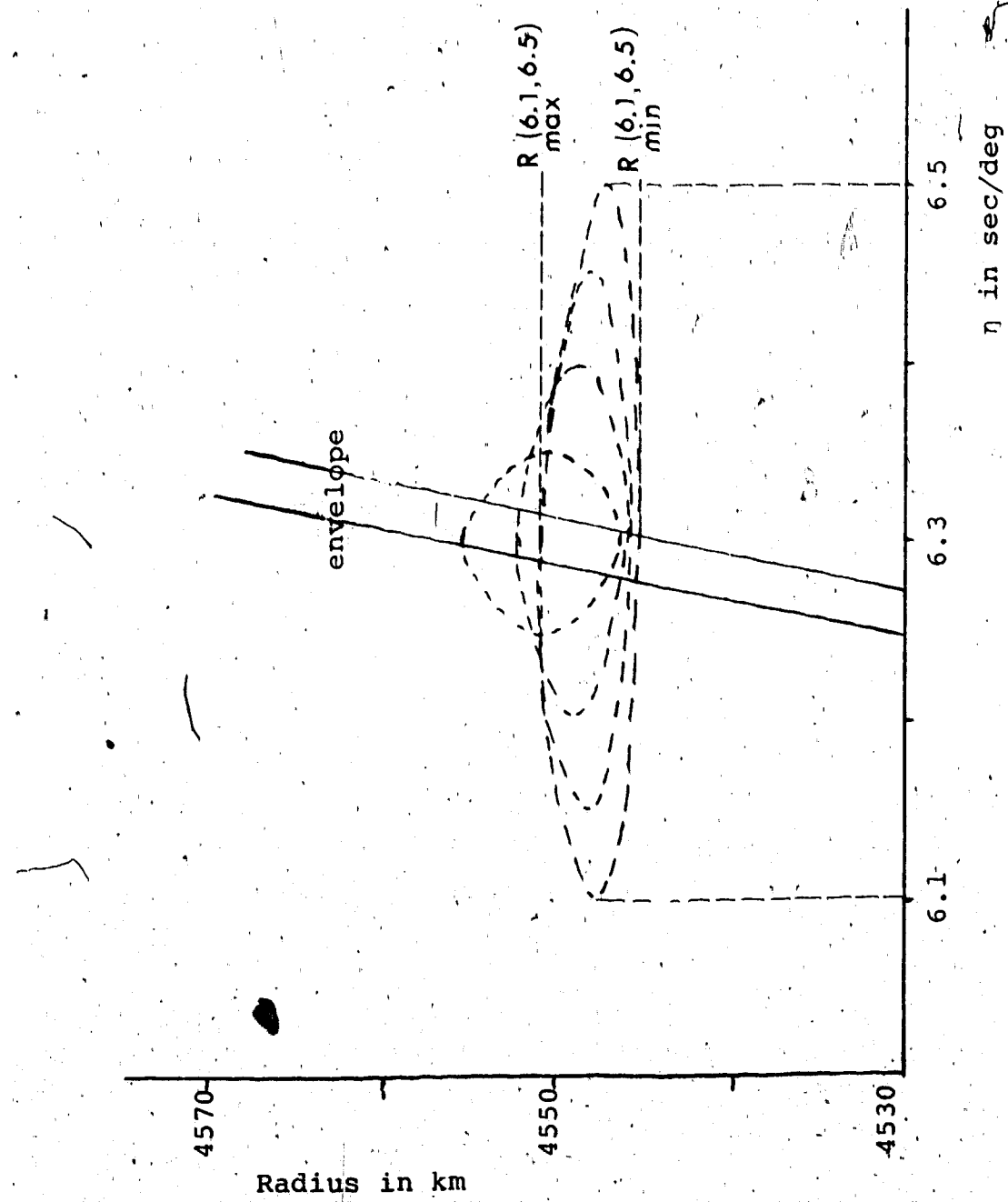


Fig. 3.15. An alternative way of plotting fig. 3.14, that is by representing the variation in extremal radii as a function of averaging length by a series of error circles in a radius versus η plot.

Yet another way of expressing this data is in a radius-velocity plot as in fig. 3.16. Here the averaged velocity has been defined as

$$V(a,b) = 2R(a,b)/(a+b)$$

The region considered is the same as that of fig. 3.8 and the outer envelope is for $b - a = 0$ (i.e. $s_{\max}(q)$ and $s_{\min}(q)$). The series of curves inside this envelope represent various values of $(b - a)$, as indicated on the diagram. As previously indicated, it can be seen that the effect of increasing the window size decreases especially beyond $b - a = 0.4$ sec/deg and that the changes in envelope width are not uniform with regard to different values of n . However, at $b - a = 0.4$, the averaged envelope has been reduced to 60% of the initial envelope for all values of n considered.

As was discussed earlier, comparisons with other inversion techniques are only valid if an averaged envelope is used, rather than the non-averaged extremal curves described at the beginning of this chapter. This type of averaging has not previously been done when using Herglotz-Wiechert inversion techniques. In particular, the reason Wiggins et al (1973) were unable to obtain results consistent with those of Johnson and Gilbert (1972) is because they were trying to compare

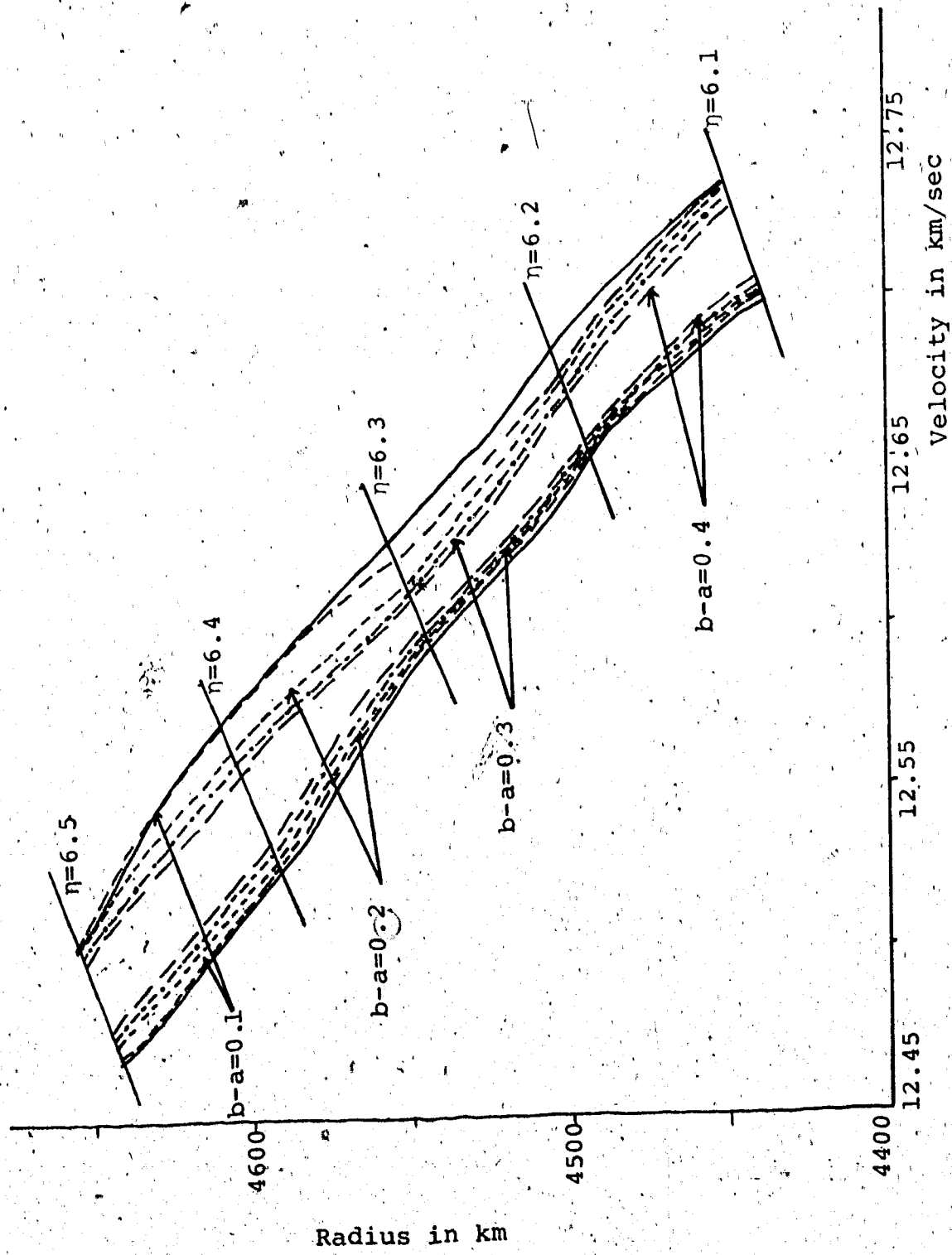


Fig.3.16. A radius-velocity plot for the same region as in fig. 3.8 where the solid line is for a zero averaging length. All sets of broken curves are for various averaging lengths, as shown. The relation to η (i.e. q in fig. 3.8) is shown by the solid lines across the curves and the values of η are as shown.

two different types of results. Averaging extremal curves (as oppose to maximising and minimising averaged curves) will smooth out the envelope but will not reduce its general width. The results of Wiggins et al represent the most extreme velocity variations at any one depth, for the given data, while the resolving power versus radius plots of Johnson and Gilbert (1972) are plots of variation in averaged velocity at any one depth.

For this reason, the type of results shown in fig. 3.16 are important, in that they provide the only way of testing whether this method is as good as other inversion methods. However at this stage, it is impossible to do a quantitative comparison with other techniques as no real data has been used as yet in this inversion method.

The method of maximising and minimising both velocity-depth models and averaged models discussed so far in this chapter may be extended to other types of data. As the arguments are basically the same, they will only be outlined in the following.

The second type of data set to be discussed is (p, Δ) data. That is $u_i = p(\Delta_i)$ for a finite number of stations Δ_i , $i=1, \dots$. As no time data is available, the constraints on any $p(\Delta)$ curve are reduced because the travel-time restriction (4) is no longer

applicable. Thus the $p(\Delta)$ curve which will maximise the interval may be taken along the upper edge of the box structure in the $p-\Delta$ plane (as shown in fig. 3.17):

That is

$$p = \begin{cases} u_i & \Delta_i < \Delta < \Delta_{i+1} \\ u_{i-1} & \Delta = \Delta_i \end{cases}$$

Similarly the path along the lower edge of the box structure (fig. 3.17) will provide the minimum integral where

$$p = \begin{cases} u_{i+1} & \Delta_i < \Delta < \Delta_{i+1} \\ u_i & \Delta = \Delta_i \end{cases}$$

For both cases end points need not be considered separately.

Maximising and minimising the average radius $R(a,b)$ is also considerably simplified, as with no time constraints it is only necessary to maximise and minimise Δ regardless of the shape of ϕ . Hence the maximum and minimum averaged curves will be obtained from

$$\phi(p) = \phi(u_i) \quad \text{for } \Delta_i \leq \Delta \leq \Delta_{i+1},$$

and

$$\phi(p) = \phi(u_{i+1}) \quad \text{for } \Delta_i \leq \Delta \leq \Delta_{i+1}.$$

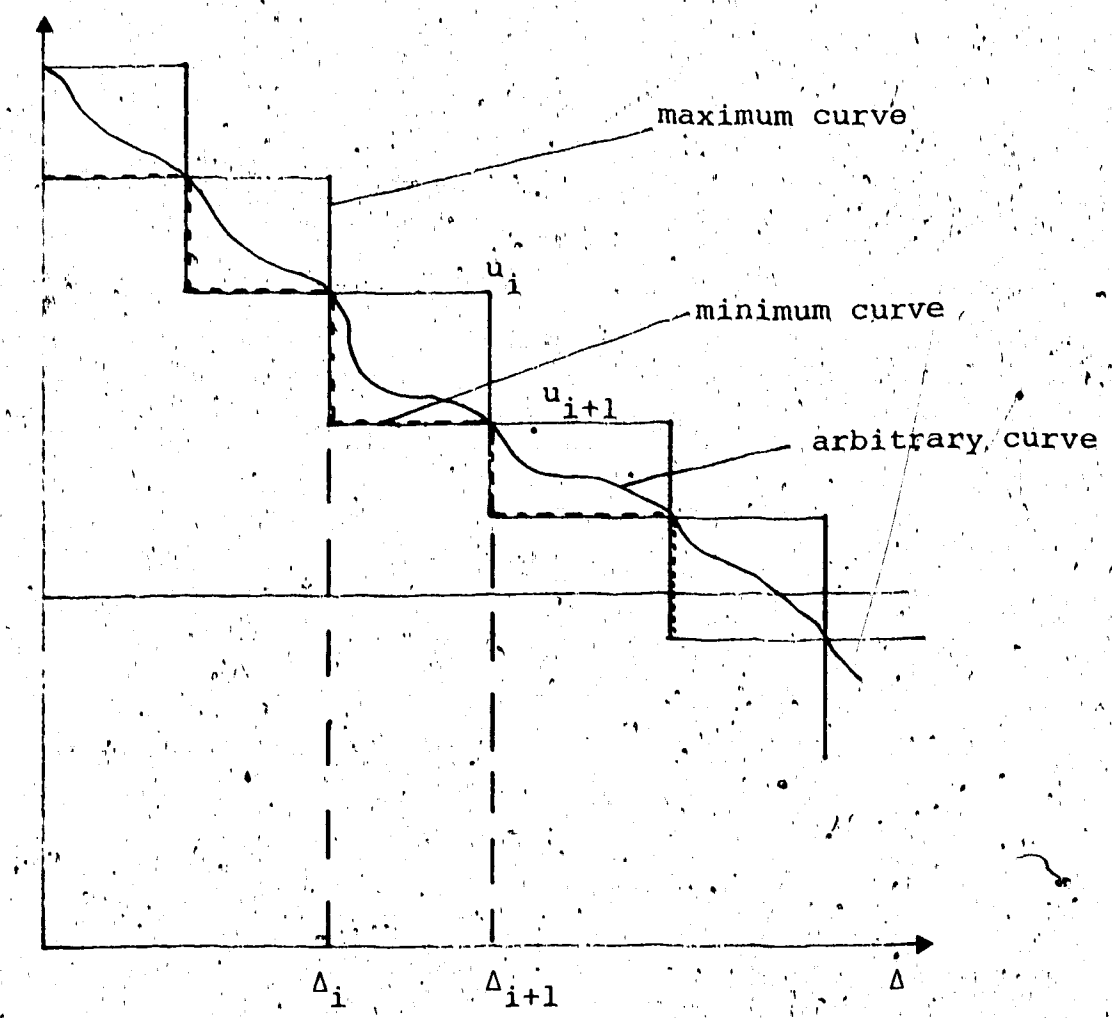


Fig. 3.17. These box structures in the $p\text{-}\Delta$ plane represent the bounds on permissible $p(\Delta)$ curves for inversion when using (p, Δ) data. The extremal $p(\Delta)$ curves are as shown, as is an arbitrary curve.

respectively, as shown in the plot of p versus Δ in fig. 3.18. Thus this type of data would be easy to program though it has not been done in this thesis.

Finally, sets of (T, Δ) data must be considered. That is, $T_i = T(\Delta_i)$ for a finite Δ_i , $i=1, \dots$. Here no p data is available and so the restrictions in the $p-\Delta$ plane become

$$(1) \quad w_i \leq p \leq u_i \quad \text{for } \Delta_i < \Delta < \Delta_{i+1}$$

$$(2) \quad p = u_i \quad \text{for } \Delta = \Delta_i$$

$$(3) \quad \frac{dp}{d\Delta} < 0$$

$$(4) \quad \int_{\Delta_i}^{\Delta_{i+1}} p d\Delta = \delta T_i$$

where $u_i = m_{i-1} = w_{i-2}$, so that rather than independent box structures in the $p-\Delta$ plane, there will be a band of permissible models, as shown in fig. 3.19. In addition, there may be some phase velocity measurements which will further restrict p in the intervals to which they refer, though the limit when p measurements are obtained for all (T_i, Δ_i) has already been discussed.

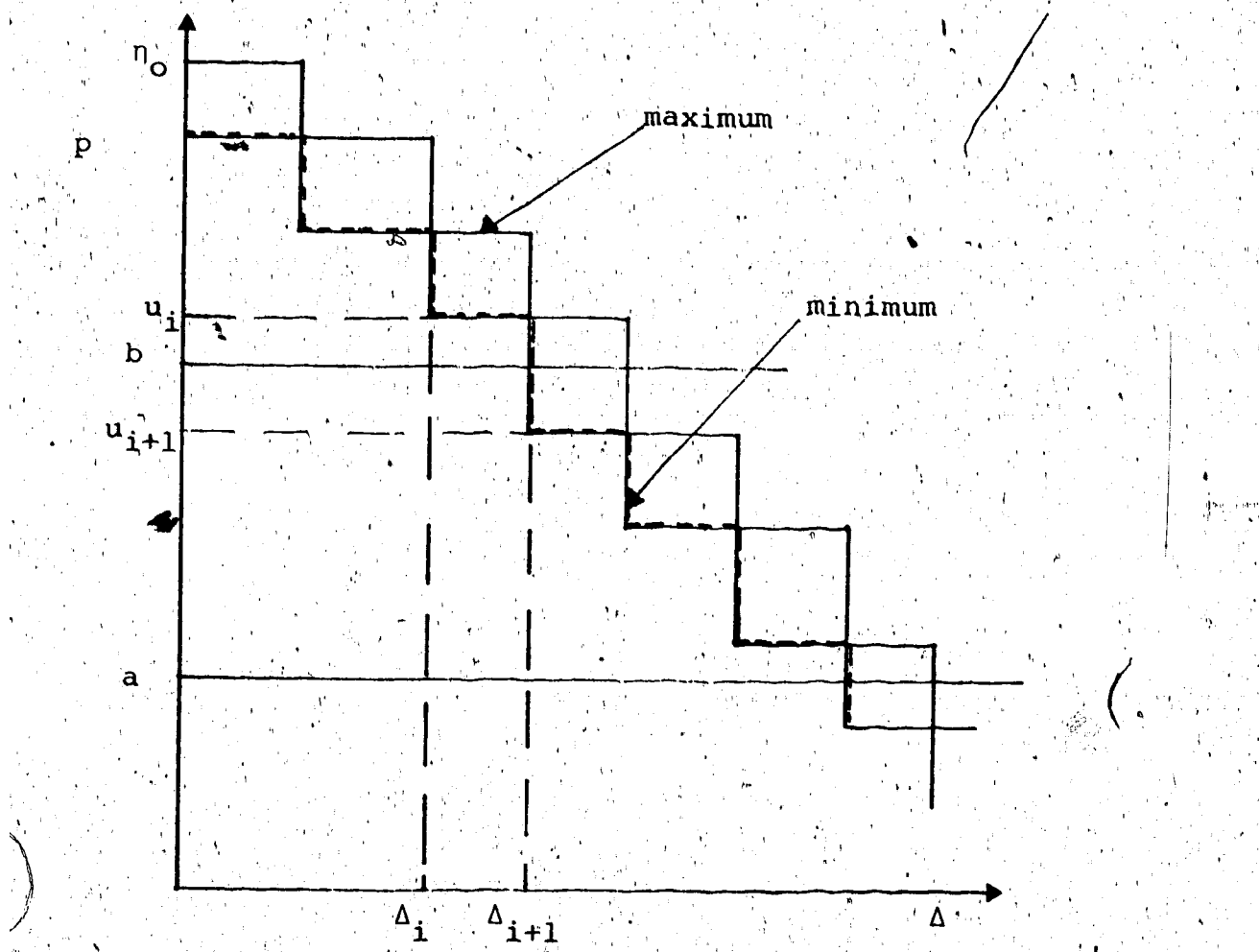


Fig. 3.18. The $p(\Delta)$ curves which give the extremal values of the averaging integral and hence the averaged radius, for (p, Δ) data.

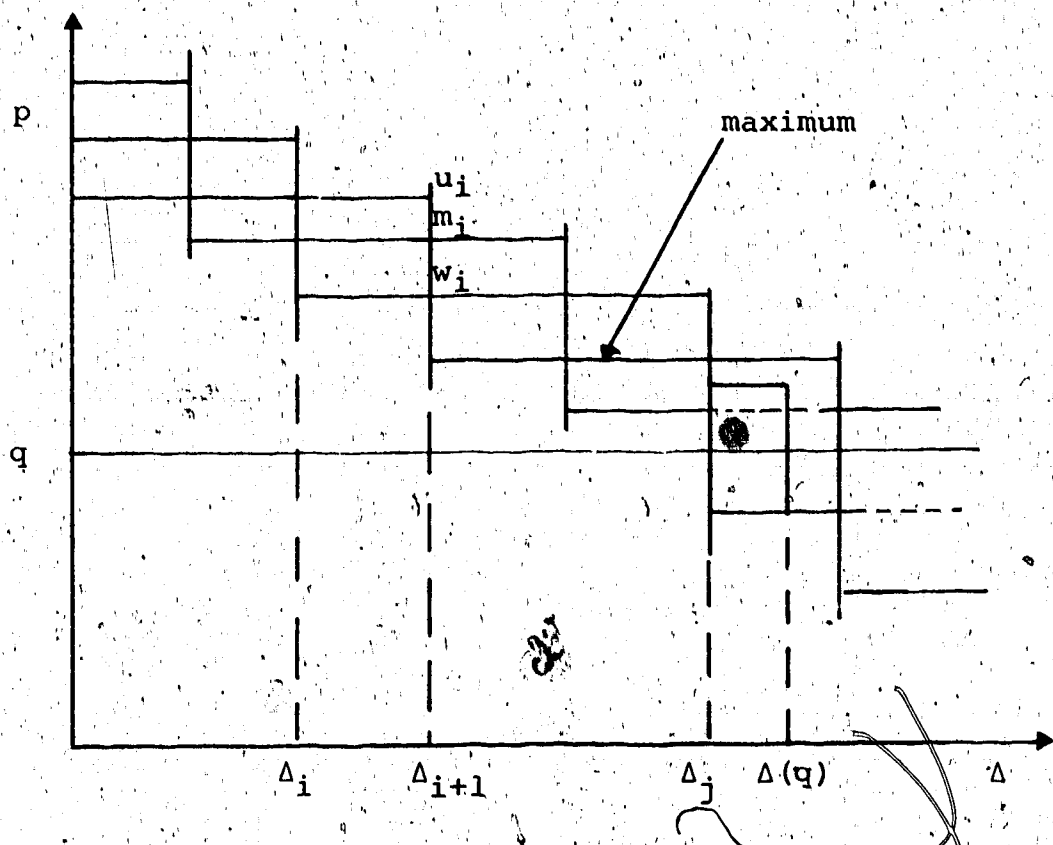


Fig. 3.19. The band of permissible models, in the $p-\Delta$ plane, for (T, Δ) data. The maximising $p(\Delta)$ curve is as shown.

at the beginning of this chapter. By the same argument as for (p, T, Δ) sets, $p = m_i$ for $\Delta_i \leq \Delta \leq \Delta_{i+1}$ will maximise the integral, $I_i^{(o)}(q)$, and hence minimise the radius $s(q)$. At $\Delta(q)$ there are two possibilities

$$(1) \quad \Delta_j < \Delta(q) < \Delta_{j+1}$$

$$(2) \quad \Delta_{j+1} < \Delta(q) < \Delta_{j+2}$$

Case (1) is as illustrated in fig. 3.19 where, to satisfy travel-time conditions,

$$\Delta(q) = \frac{\delta T_j + u_j \Delta_j - w_j \Delta_{j+1}}{u_j - w_j}$$

and p_j is chosen to maximise the integral $I_j^{(o)}$ either at $\partial I_j^{(o)} / \partial p_j = 0$ (active maximum) or at one of the constraints on p_j (constrained or passive maximum).

For the second case two local maxima exist which must be numerically tested to determine the global maximum. One is as described in (1) while the other is with $p = m_j$ in the j^{th} interval and the same as (1) in the $(j+1)^{\text{th}}$ interval. $\Delta(0)$ is not essentially different from the general interval, except when $u_1 = \infty$.

As taking $p = m_i$ will maximise $I_i^{(o)}(q)$, so perturbing p as much as possible from the mean, while satisfying travel time constraints will minimise $I_i^{(o)}(q)$.

However it is not possible to set

$$p = \begin{cases} u_i & \Delta_i \leq \Delta < \theta_i \\ w_{i+1} & \theta_i \leq \Delta < \Delta_{i+1} \end{cases}$$

(where θ_i is determined from the constraints) as at Δ_{i+1} there will exist a discontinuous increase in p from w_i to u_{i+1} . From the restriction $dp/d\Delta \leq 0$ this increase is not possible and so the minimum must be constrained so that

$$p = \begin{cases} \hat{p}_i & \Delta_i \leq \Delta < \theta_i \\ \hat{p}_{i+1} & \theta_i \leq \Delta < \Delta_{i+1} \end{cases}$$

where

$$\theta_i = \frac{\delta T_i + \hat{p}_i \Delta_i - \hat{p}_{i+1} \Delta_{i+1}}{\hat{p}_i - \hat{p}_{i+1}}$$

The values of the variables \hat{p}_i , $i=1, \dots, j$, must be determined numerically so that either $\partial I_i / \partial \hat{p}_i = 0$ (active minimum), $p = u_i$ (passive minimum with $\partial I_i / \partial \hat{p}_i < 0$) or $p = w_{i-1}$ (passive minimum with $\partial I_i / \partial \hat{p}_i > 0$). This is illustrated in fig. 3.20.

At $\Delta(q)$, the contribution from the j^{th} interval, where $\Delta_j \leq \Delta(q) \leq \Delta_{j+1}$, depends on the position of q :

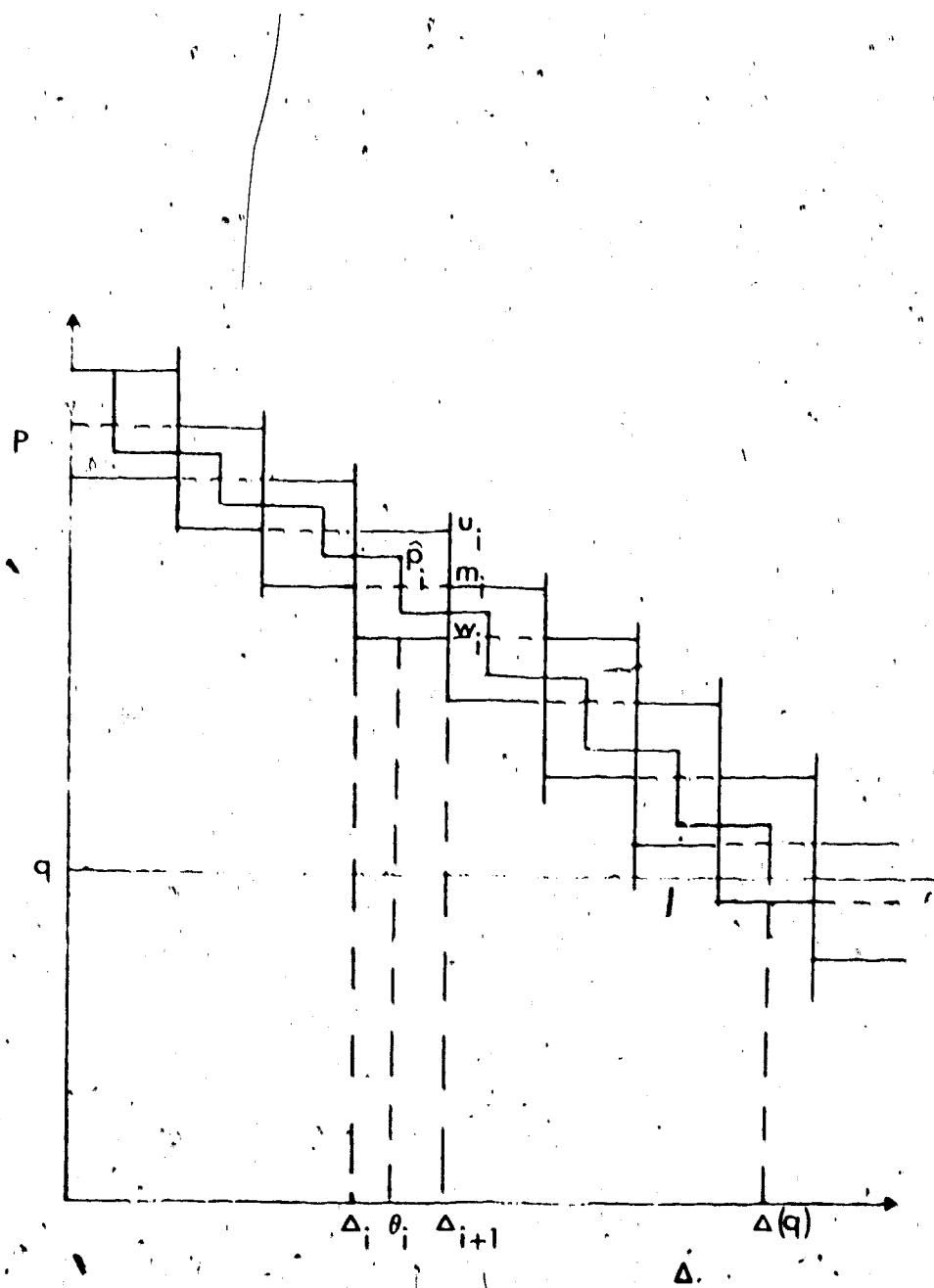


Fig. 3.20. The minimising $p(\Delta)$ curve for (T, Δ) data is represented by the solid line through the band structures. The end point, $\Delta(q)$, is that for $w_j \leq q < m_j$.

$$(1) \quad w_j \leq q < m_j$$

$$I_j = (\Delta(q) - \theta_{j-1}) \cosh^{-1} \frac{\hat{p}_j}{q}$$

where

$$\Delta(q) = \frac{\delta T_j + \hat{p}_j \Delta_j - \hat{p}_{j+1} \Delta_{j+1}}{\hat{p}_j - \hat{p}_{j+1}} = \theta_j \quad (\text{as shown in fig. 3.20}).$$

$$(2) \quad m_j \leq q < u_j$$

$$I_j = 0$$

At $\Delta(0)$, no true minimum exists. If u_1 is defined

then

$$\hat{p}_1 = u_1$$

and

$$I_1 = (\theta_1 - \Delta_1) \cosh^{-1} \frac{\hat{p}_1}{q}$$

If $u_1 = \infty$, then $\hat{p}_1 = \infty$, $\theta_1 = 0$, and

$$I_1 = 0$$

$$I_2 = (\theta_2 - \Delta_1) \cosh^{-1} \frac{\hat{p}_2}{q}$$

In determining the extremal average radii, the same arguments may be used as for (p, T, Δ) data sets to obtain the $p(\Delta)$, which will maximise $\phi(p, a, b)\Delta(p)$ as shown in fig. 3.21. That is

$$p = \begin{cases} m_j & \Delta_j \leq \Delta < \Delta_{j+1} & n_0 \leq m_j < u_j \\ m_i^* & \Delta_i \leq \Delta < \Delta_i^* & b \leq m_i^* < u_i \\ \hat{p}_{i+1} & \theta_i \leq \Delta < \theta_{i+1} & w_i \leq \hat{p}_{i+1} \leq b \\ \hat{p}_k & \theta_k \leq \Delta < \theta_{k+1} & w_{k-1} \leq \hat{p}_k < u_k \end{cases}$$

where, as before, m_i^* , θ_i^* , \hat{p}_{i+1} and θ_{i+1} are chosen to satisfy travel time constraints and maximise $\phi(p, a, b)\Delta(p)$.

Thus

$$\theta_i^* = \frac{\delta T_i + m_i^* \Delta_i - \hat{p}_{i+1} \Delta_{i+1}}{m_i^* - \hat{p}_{i+1}}$$

and in the limits as

$$(1) \quad b = u_i, \quad m_i^* = \hat{p}_i, \quad \theta_i^* = \theta_i$$

$$(2) \quad b = w_i, \quad m_i^* = m_i, \quad \theta_i^* = \Delta_{i+1}$$

For $w_i \leq b \leq m_i$, $m_i^* = m_i$ and $\theta_i^* = \Delta_{i+1}$ while for $m_i < b \leq u_i$, there are two possibilities:- $m_i^* = b$.

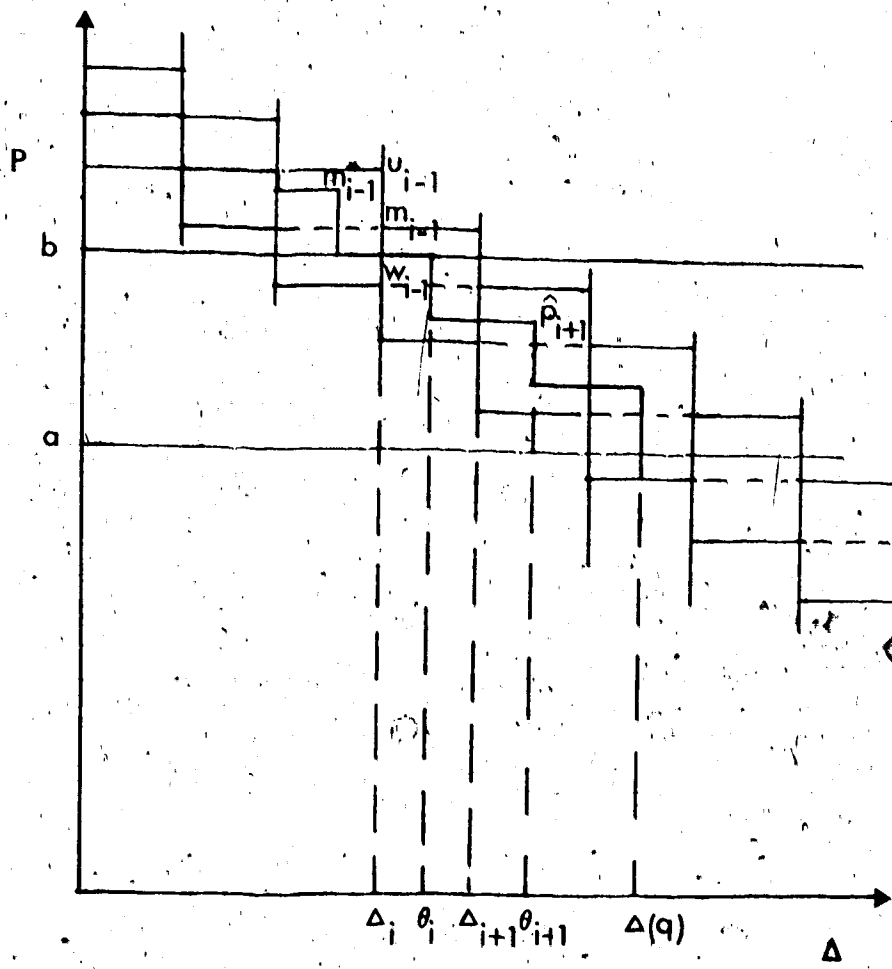


Fig. 3.21. The $p(\Delta)$ curve which will maximise the integral is shown as a solid line through the band structure, with $b-a$ the interval over which an average radius is taken.

or $m_i^* > b$, which must be tested numerically to obtain the absolute maximum of the integral. Also since in maximising the integral the object is to increase the area around $p = b$, taking $\hat{p}_{i+1} = b$ will increase the value of $\phi(p, a, b)\Delta(p)$, as is shown in fig. 3.21.

The values of p which will give the minimum $\phi(p, a, b)\Delta(p)$ curve are as shown in fig. 3.22, where to satisfy time constraints,

$$\theta_i^* = \frac{\delta T_i + \hat{p}_i \Delta_i - m_i^* \Delta_{i+1}}{\hat{p}_i - m_i^*}$$

and m_i^* and \hat{p}_{i+1} are chosen to minimise the integral.

In the limit

$$(1) \quad b = u_i, \quad \hat{p}_i = m_i, \quad \theta_i^* = \Delta_{i+1}$$

$$(2) \quad b = u_{i+1}, \quad m_i^* = w_i, \quad \theta_i^* = \theta_i$$

Obviously to program for this type of data is more difficult than for (p, T, Δ) data so that though a program has been written to determine $s_{\max}(q)$ and $s_{\min}(q)$ as a function of velocity for (T, Δ) data subroutines to find non-extremal models and calculate $R_{\max}(a, b)$ and $R_{\min}(a, b)$ have not yet been included.

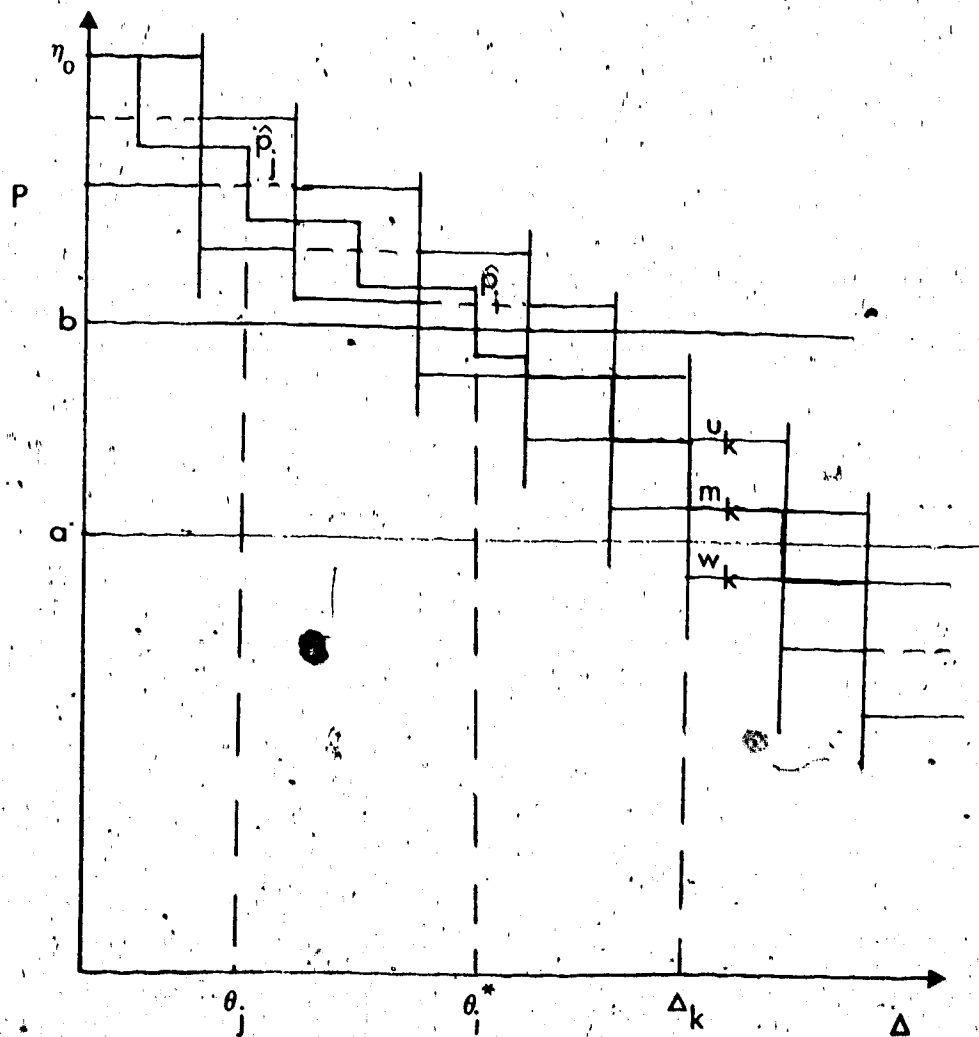


Fig. 3.22. The minimising $p(\Delta)$ curve for (T, Δ) data for an averaging interval $b-a$, is represented by the solid line through the band structure.

The computations done thus far for (p, T, Δ) have used ideal data in order to illustrate certain points about the general method of inversion. However once the analytical results of the following two chapters, on high and low velocity gradients with discrete data, have been programmed it will be possible to use real travel-time data to obtain an envelope of velocity-depth profiles over the whole earth.

CHAPTER 4

LOW VELOCITY CHANNELS

As was shown in Chapter 2, for both discrete and continuous data, it may be possible to distinguish between different types of discontinuity in the travel-time curve using amplitudes. For the type I or I' discontinuity, the problem may be reduced by an 'earth-stripping' process to a special case of discrete data and the conditions of maximisation and minimisation of velocity-depth models discussed in the previous chapter will be valid. Fig. 4.1 shows an example of such an earth-stripping procedure for the outer core where both P and S wave data were used (i.e. PKP-PcP, SKS-ScS) and the core radius was taken to be 3481 km. The diagram is merely intended to illustrate the type of results possible with the procedure. Obviously if only PKP data is used the extremal curves will not be as close.

However, for a type II discontinuity (i.e. $\eta(r^{(k)}+0) < \eta(r^{(k)}-0)$), $\delta\Delta_{(p)}^{(k)}$ is undefined and the above method of reducing the problem cannot be used. Also it may not be possible, in practice, to distinguish between types of discontinuity from amplitude measurements, in which case the results of Gerver and Markeshevichs must be applied to discrete data.

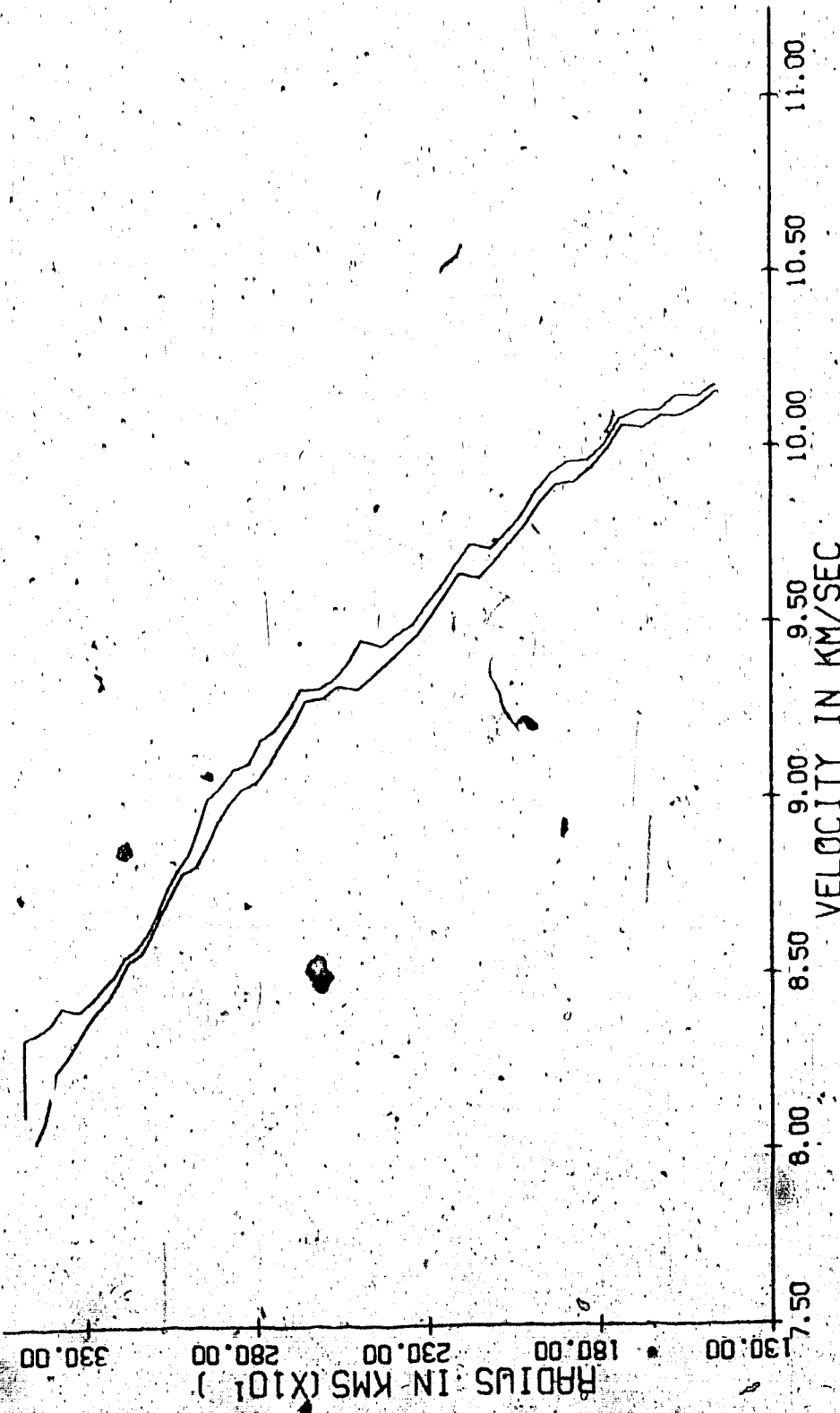


Fig. 4.1. Radius-velocity plot for the outer core region, using 'earth-stripped' PKP and SKS data.

McMechan (1971) has inverted discrete data containing low velocity zones, to obtain extremal velocity-depth profiles. However his method was to randomly change the velocity function and depth of a low velocity channel to obtain those which gave a maximum or minimum velocity as a function of depth. It should be possible to obtain an analytic solution to this problem (i.e.

finding extremal integrals for $q < p^{(1)}$ in equation (2.7)). This has been looked at by Chapman (personal communication) and will be discussed here, though no actual computations have yet been done.

For $q > p^{(1)}$, the standard Herglotz-Wiechert integral may be used, as in Chapter 3. For $q < p^{(1)}$,

$$I^{(k)}(q) = \sum_{k=1}^q \int_{\bar{r}^{(k)}}^{r^{(k)}} \frac{2}{r} \tan^{-1} \sqrt{\frac{n^2 - p^{(k)}_r}{p^{(k)}_r - q^2}} dr \quad (4.1)$$

(where $r^{(k)}$ is the top and $\bar{r}^{(k)}$ is the bottom of the k^{th} low velocity zone) must also be determined. This is obviously more difficult to solve directly than when $q > p^{(1)}$, as both $\bar{r}^{(k)}$ and $n(r)$ for $r < r^{(k)}$ are unknown. However, it is possible to place bounds on $n(r)$ within the low velocity channel, subject to the $\delta\tau^{(k)}$ and $\delta\Delta^{(k)}(p)$ constraints.

To determine the range of velocities, it is necessary to determine the possible radii, $s(q)$, where (by rewriting equation (2.7))

$$s(q) = r_0 \exp\left(-\frac{I^{(0)}(q)}{\pi} - \frac{1}{\pi} \sum_{k=1}^K I^{(k)}(q)\right).$$

A low-velocity channel may be constrained such that

$$\eta_{\min}^{(k)}(r) \leq \eta(r) \leq \eta_{\max}^{(k)}(r) \quad \text{for } \bar{r}^{(k)} < r < r^{(k)}$$

where, by definition of a low velocity channel, $\eta_{\min}^{(k)} \geq p^{(k)}$ and $\eta_{\max}^{(k)} \rightarrow \infty$ for zero velocity. It can be shown (Appendix 3) that using only the $\delta T^{(k)}$ constraint, $\eta(r) = \eta_{\min}^{(k)}(r)$ and $\eta(r) = \eta_{\max}^{(k)}(r)$ for $\bar{r}^{(k)} < r < r^{(k)}$ respectively maximise and minimise $r = s(q)$ for most $q < p^{(k)}$.

It should be noted that in general, a model will only be physically valid if $ds/dq \geq 0$, where the limits as ds/dq tend to ∞ and 0 correspond to $q = p^{(k)}$ and a reflection, respectively. This implies that

$$\frac{dI^{(0)}}{dq} + \frac{d}{dq} \sum_{k=1}^K \eta^{(k)}(q) \geq 0$$

where

$$q \frac{dI^{(0)}}{dq} = - \int_0^\Delta(q) \frac{p d\Delta}{(p^2 - q^2)^{1/2}}$$

which is negative, unless $\Delta(q)$ is on a reversed branch.

However,

$$\frac{dI^{(k)}}{dq} = \int_{r^{(k)}}^{r^{(k)}} \frac{2q}{n^2 - q^2} \sqrt{\frac{n^2 - p^{(k)} r^2}{p^{(k)} r^2 - q^2}} \frac{dr}{r}$$

which is positive but not significant with respect to $dI^{(o)}/dq$ except for $q \leq p^{(k)}$. Thus to determine if a low velocity channel is physically valid it is only necessary to check that

$$\sum_{k=1}^K q \frac{dI^{(k)}}{dq} \leq - \frac{dI^{(o)}}{dq}$$

In the case where a high velocity zone is immediately below the low velocity channel, $dI^{(o)}/dq$ will be small for rays bottoming in this region and so $dI^{(k)}/dq$ will be severely restricted from above.

In determining the actual values of $n_{\max}^{(k)}$ and $n_{\min}^{(k)}$ some other geophysical data must be used. Knowing $\delta t^{(k)}$, $r^{(k)}$ and $r_{\max}^{(k)}$, the extremal values of radius at the bottom of the channel, are defined and for $q < p^{(k)}$, the velocity bounds are defined by $n = n_{\min}^{(k)}(r)$ and $n = n_{\max}^{(k)}(r)$. However, below a certain depth these low velocity channel models will not define the extremal profiles and to do so the channel model must be slightly perturbed (see Appendix 3). It can be shown that

fractional variation in permitted velocities below a low velocity zone decreases away from the channel (i.e. the effect of the channel is most important in the vicinity of the channel) and

$$\frac{I_{\max}^{(k)}(q)}{I_{\min}^{(k)}(q)} \rightarrow \frac{I_{\max}^{(k)}(0)}{I_{\min}^{(k)}(0)} \quad \text{as } q \rightarrow 0$$

So far the $\delta\Delta^{(k)}(p)$ constraint has not been fully utilised as, for example, if $\eta^{(k)}(r) \rightarrow \infty$, the $\delta\tau^{(k)}$ discontinuity may be satisfied by an infinitesimally thin low velocity channel but this would give $\delta\Delta^{(k)}(p) \rightarrow 0$ which would not agree with the actual data. Also $\delta\tau^{(k)}$ can be satisfied with a thick channel and $\eta(r) \rightarrow p^{(k)}$, but this would create a large jump in $\delta\Delta^{(k)}(p)$, which again is incompatible with the data. Therefore it should be possible to further restrict low velocity models using the $\delta\Delta^{(k)}(p)$ constraint.

As stated in Chapter 2, low velocity models may have numerical instabilities and to avoid this the turning radius may be averaged over a range of $\eta(r)$, as shown by Bessonova et al, 1970. Maximising and minimising an averaged radius for discrete data, without low velocity zones, was discussed in the previous chapter. The inclusion of low velocity channels will be briefly discussed

here. It will be recalled that the definition of a radius averaged over some interval $a \leq p \leq b$ is

$$\ln \frac{R(a, b)}{r_0} = - \frac{1}{b-a} \left(\int_a^b \Delta(p) \phi(p, a, b) dp + \int_a^b \sum_{k=1}^K \tau^{(k)}(q) dq \right) \quad (4.2)$$

where $\tau^{(k)}(q)$ is as defined in equation (4.1) and

$$\phi(p, a, b) = \begin{cases} \cos^{-1} \frac{a}{p} - \cos^{-1} \frac{b}{p} & b < p < r_0 \\ \cos^{-1} \frac{a}{p} & a < p < b \end{cases}$$

As

$$\frac{d\tau}{dp} = - \Delta$$

$$\tau(q) = - \int_{r_0}^q \Delta(p) dp + \sum_{k=1}^K \delta \tau^{(k)} \quad (4.3)$$

and hence, integrating by parts

$$\begin{aligned} \int_a^{r_0} \Delta(p) \phi(p, a, b) dp &= - \phi(p, a, b) \int_a^{r_0} \Delta(p) dp \Big|_{a}^{r_0} \\ &\quad + \int_a^{r_0} \int_p^{r_0} \Delta(q) dq \frac{\partial \phi}{\partial p} dp \\ &= \int_a^{r_0} \tau(p) \frac{\partial \phi}{\partial p} dp - \sum_{k=1}^K \delta \tau^{(k)} \phi(p^{(k)}, a, b) \end{aligned}$$

using equation (4.3) and the condition $\phi(a, a, b) = 0$.

Thus equation (4.3) may be rewritten as

$$\ln \frac{R(a, b)}{r_0} = -\frac{1}{b-a} \int_a^b \tau(p) \frac{\partial \phi}{\partial p} dp + \frac{1}{b-a} \sum_{k=1}^K \delta \tau^{(k)} \phi(p^{(k)}, a, b)$$

$$-\frac{1}{b-a} \int_a^b \sum_{k=1}^K I^{(k)}(q) dq \quad (4.4)$$

where

$$\frac{\partial \phi}{\partial p} = \begin{cases} \frac{a}{p(p^2-a^2)^{\frac{1}{2}}} - \frac{b}{p(p^2-b^2)^{\frac{1}{2}}} & \text{for } b < p < r_0 \\ \frac{a}{p(p^2-a^2)^{\frac{1}{2}}} & \text{for } a < p < a \end{cases}$$

Finding the extremal values of $R(a, b)$ then becomes a question of bounds on τ . Because the sign of $\phi'(p, a, b)$ varies across $p = b$, $\tau = \tau_{\min}(p)$ will maximise radius for $a < p < b$ while for $b < p < r_0$, $\tau = \tau_{\max}(p)$ will maximise the radius. The values of τ_{\max} and τ_{\min} will depend on the data set. For the simple case of $T_i = T(\Delta_i)$ and $p_i = p(\Delta_i)$, the upper and lower limits of τ , in the τ - p plane, become a box-structure as shown in fig. 4.2.

Obviously in this case

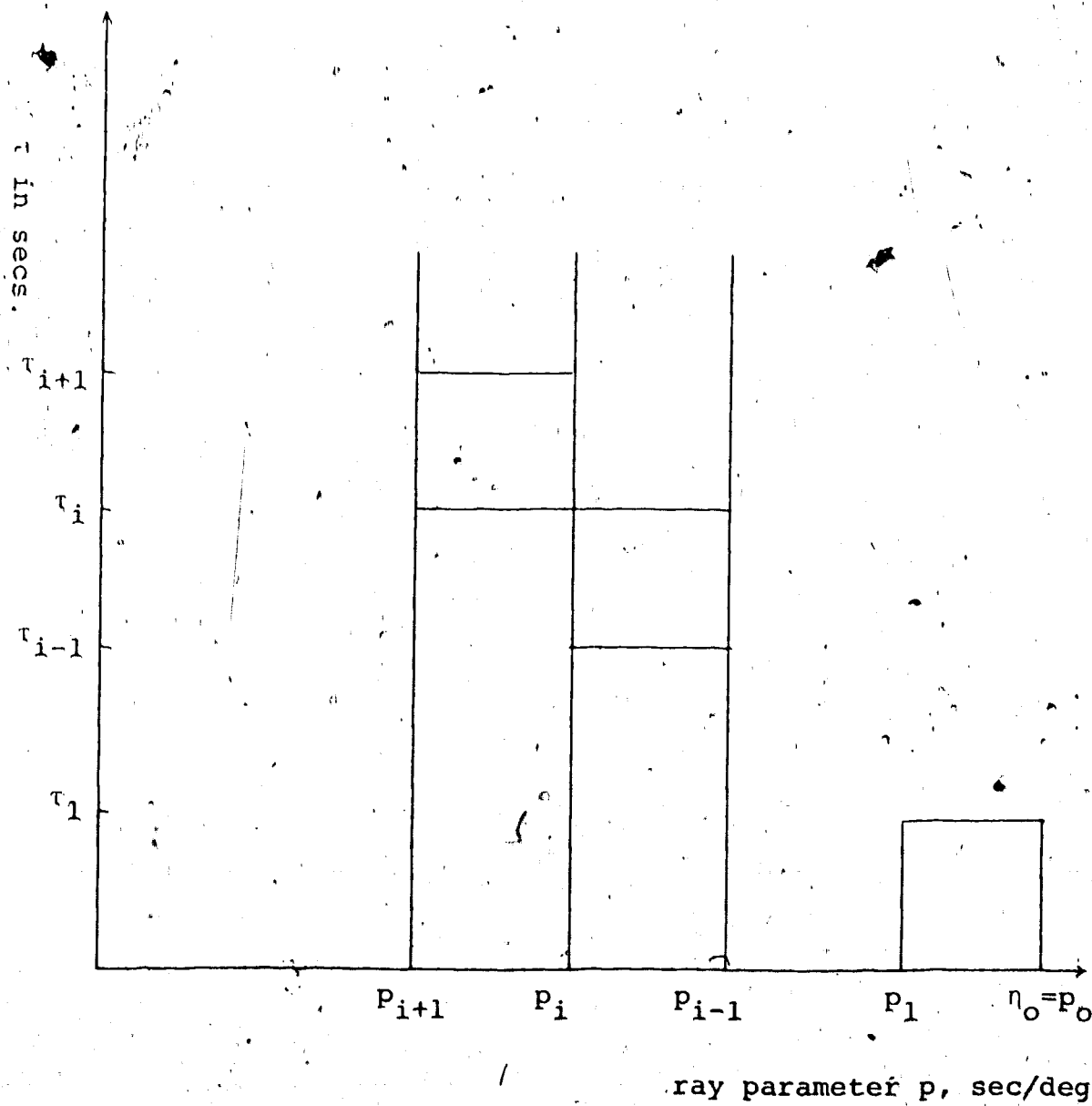


Fig. 4.2. The upper and lower limits on τ for (T, p) data, shown in the τ - p plane.

$$\tau_{\max}(p) = \tau_i \quad \text{for } p_i < p < p_{i+1}$$

$$\tau_{\min}(p) = \tau_{i+1}$$

and given other data sets, τ may be suitably limited.

The second term on the right hand side of equation (4.4) may be estimated, with limits, if (T_i, p_i, Δ_i) are measured. At worst, it must be assumed that there are discontinuities in every interval and then

$$\delta\tau^{(k)} = \tau_i - \tau_{i+1}$$

with $p^{(k)}$ such that $\phi(p^{(k)}, a, b)$ is maximised in that interval.

The third term on the right hand side of equation (4.4) may also be maximised and minimised using $\tau(p)$ and $\delta\tau^{(k)}$ data.

CHAPTER 5

TRIPPLICATIONS

A triplication on the travel-time curve is caused by an increase in velocity gradient. For a triplication, the condition $dp/d\Delta \leq 0$ is no longer valid, as for the reflected part of the $T-\Delta$ curve p becomes a monotonically increasing function of Δ . Thus (as can be seen in fig. 5.1) that segment of the Herglotz-Wiechert integral is negative. For continuous data this presents no problem. However with discrete data a number of possibilities must be considered.

If triplications are assumed to exist, then:

- (1) the triplications occur between data points and are unobserved,
- (2) triplications occur at data points but are unobserved or
- (3) triplications are observed at the data points.

The first case will not cause any change in the band structure. For the second case, the data point observed may be on the reflected branch such that p_i is less than p_{i+1} where the $i+1^{\text{th}}$ measurement is again on the forward branch. This situation is indicated in fig. 5.1 though of course the $p(\Delta)$ curve shown in this figure is for continuous data. If this is the case at Δ_i then using the standard definitions of m_i , u_i and w_i as

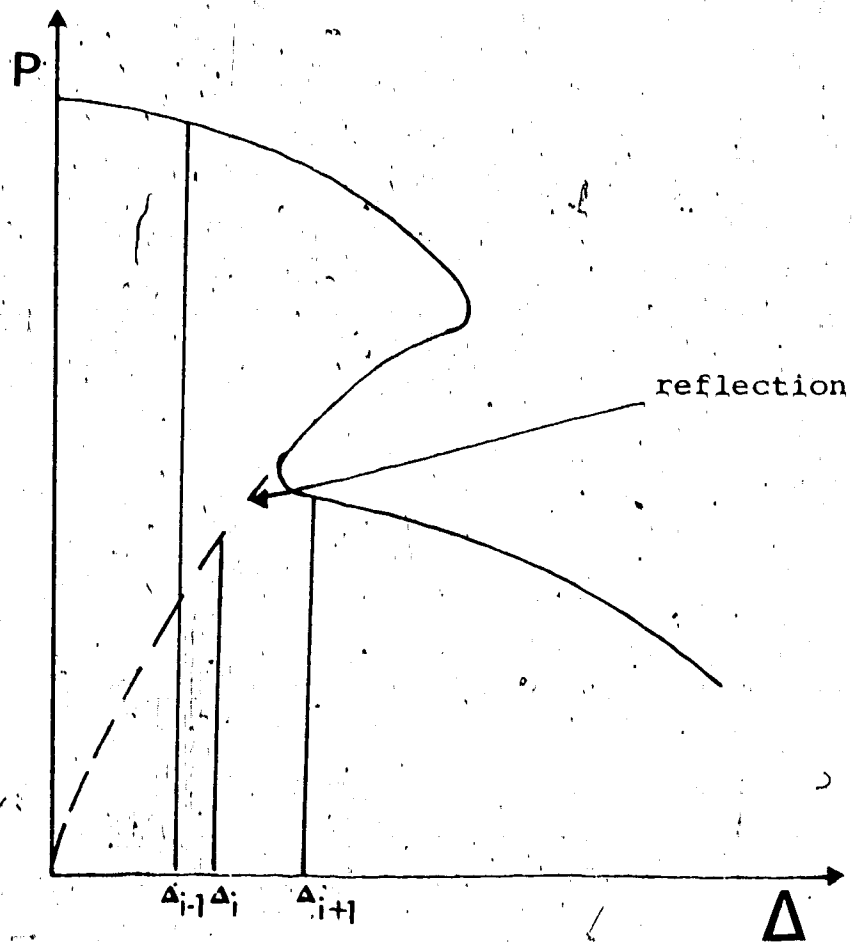


Fig. 5.1. Ray parameter, p , in sec/deg, as a function of range, Δ , in deg. This $p(\Delta)$ curve shows a triplication with an example of possible data, for unobserved triplications at data points, superimposed.

in Chapter 3 (i.e. T, Δ data is being considered) then to allow for this possibility the band between Δ_i and Δ_{i+1} must be widened (as illustrated in fig. 5.2).

For the case of an observed triplication, which has been studied by McMechan (1971), and McMechan and Wiggins (1972) the time constraint can no longer be satisfied on certain branches, when maximising and minimising the integration curve. To maximise in the interval containing the triplication, therefore, it is possible to take $p = u_i$, for $q \leq u_i$ (when again considering the general case of T, Δ observations with no p data). However, compensation must be made for this branch's lack of agreement with travel time constraints at some stage.

The maximum curve will be as shown in fig. 5.4 where the correspondence between the branches of the $T-\Delta$ curve and the $p(\Delta)$ curve at a triplication are as shown in figs. 5.3 and 5.4. The section labelled A in both diagrams refers to the forward branch, as does that labelled C. The section labelled B refers to the reverse branch of the travel time curve. The reflected branch is fixed either by time constraints or such that it passes through (Δ_i, w_i) . The point p' , shown in the diagram, defines the value of q for which this curve is an absolute maximum. More generally, the maximum for any

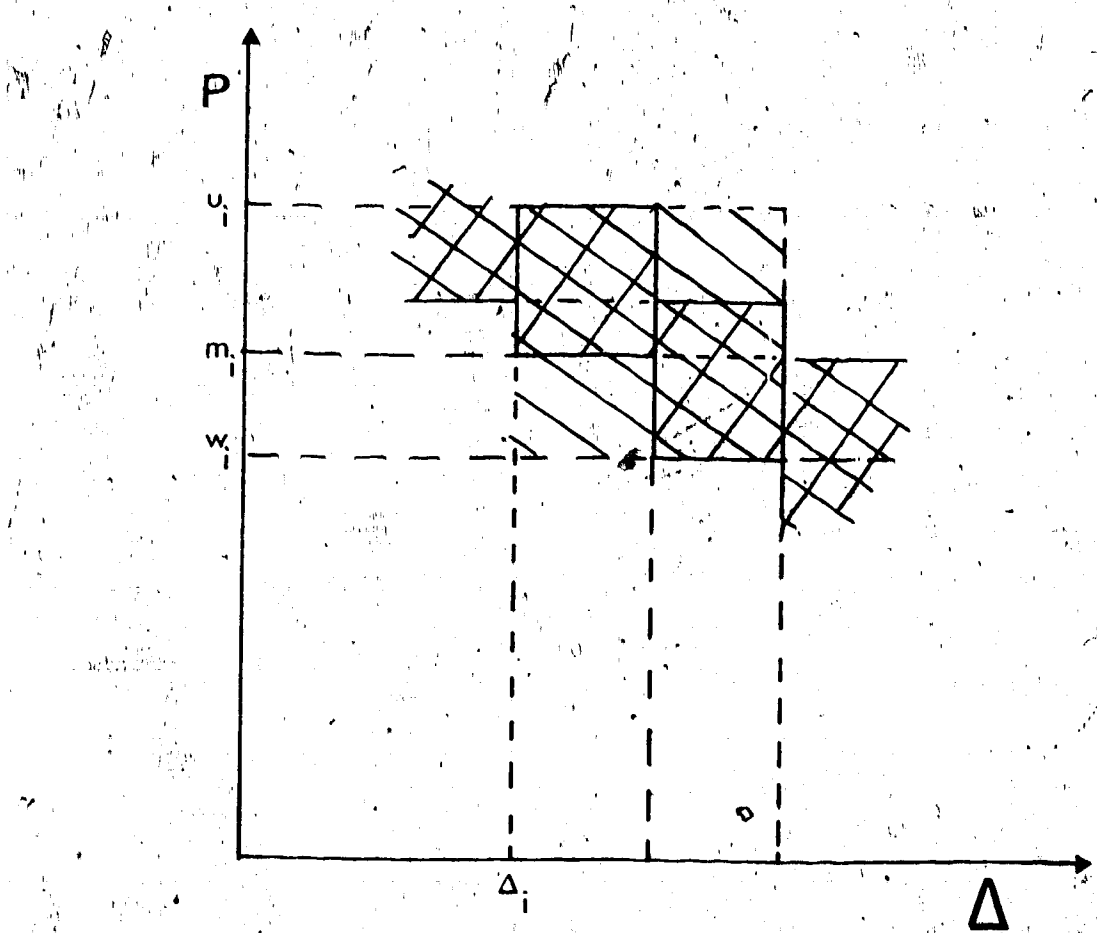


Fig. 5.2. The band structure, in the $p-\Delta$ plane, for an unobserved triplication at Δ_i . The cross hatched area shows the usual band width if no triplications occur while the shaded region shows the increase in band width necessary to accommodate the type of situation illustrated in fig. 5.1.

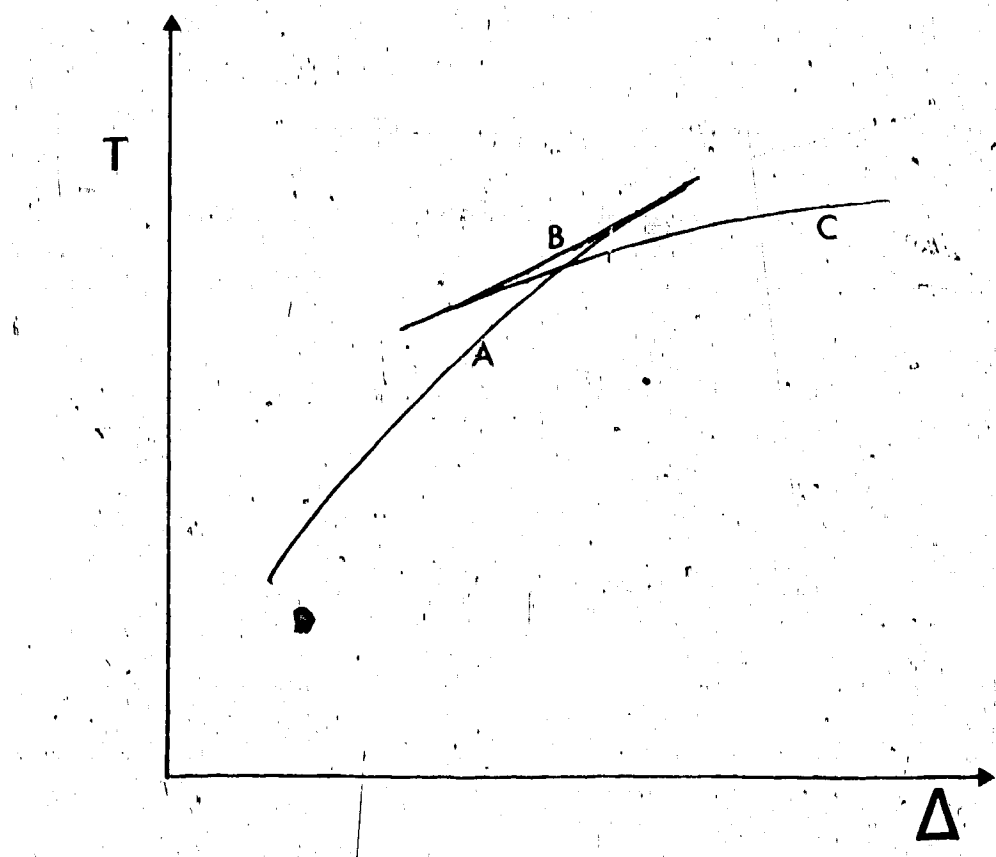


Fig. 5.3. Portion of the $T-\Delta$ which includes a triplication. The labels on the difference branches of the curve correspond to sections of the $p(\Delta)$ curve shown in fig. 5.4.

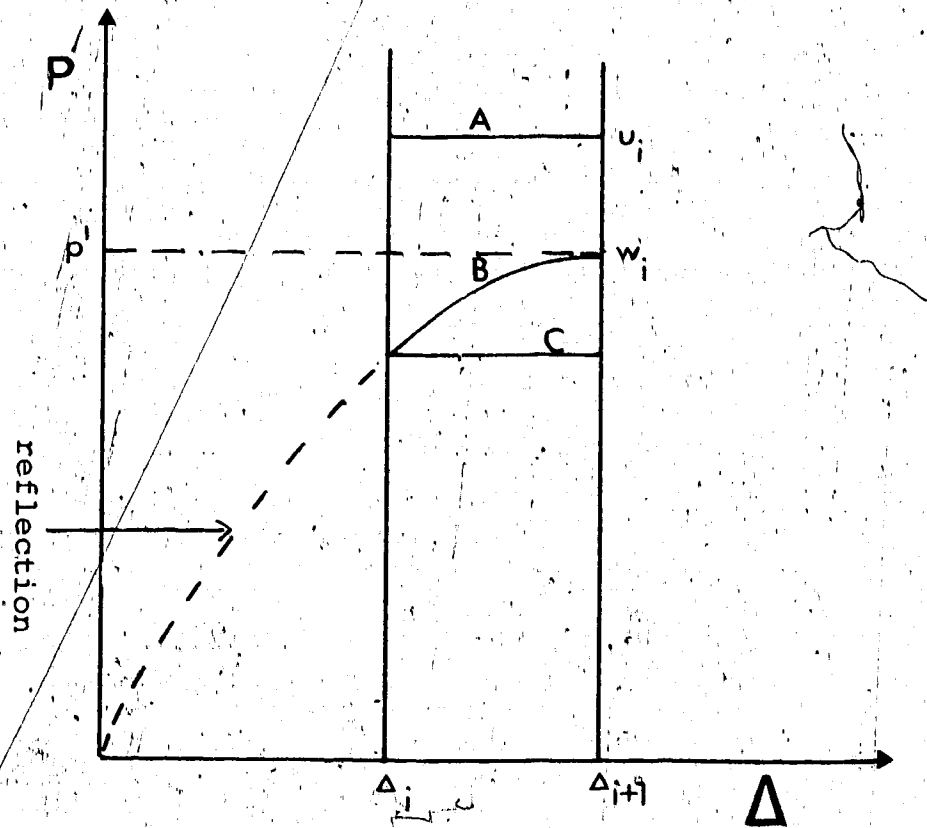


Fig. 5.4. The $p(\Delta)$ curve in the i^{th} interval which will maximise the Herglotz-Wiechert integral when a triplication is observed at Δ_i . Labels A and C refer to the forward branches of the travel-time curve, as shown in fig. 5.3 while B refers to the reverse branch.

particular q may be obtained from fig. 5.5, where \hat{p}_i is such that travel-time constraints are satisfied and the integral $I^{(o)}(q)$ is a maximum. Below a certain value of q , though q is still greater than w_i , the curve of integration is as shown in fig. 5.6. In the limit as $q \rightarrow w_i$, the reverse branch disappears, $\hat{p}_i \rightarrow m_i$ and the case becomes that discussed in Chapter 3.

The minimisation for $q > m_i$ is as shown in fig. 5.7, where $\hat{p}_i = q$. For $q < m_i$ it is not obvious whether fig. 5.8(a) or 5.8(b) would provide the absolute minimum, though this may be tested numerically. As $q \rightarrow w_i$, the case is again that discussed in Chapter 3, for an absolute minimum.

When triplications are observed at data points it is possible to include the maximising and minimising procedure necessary at a triplication in the more general computations considered in Chapter 3. However, this has not been done in the computations of this thesis as it has already been discussed by McMechan (1971).

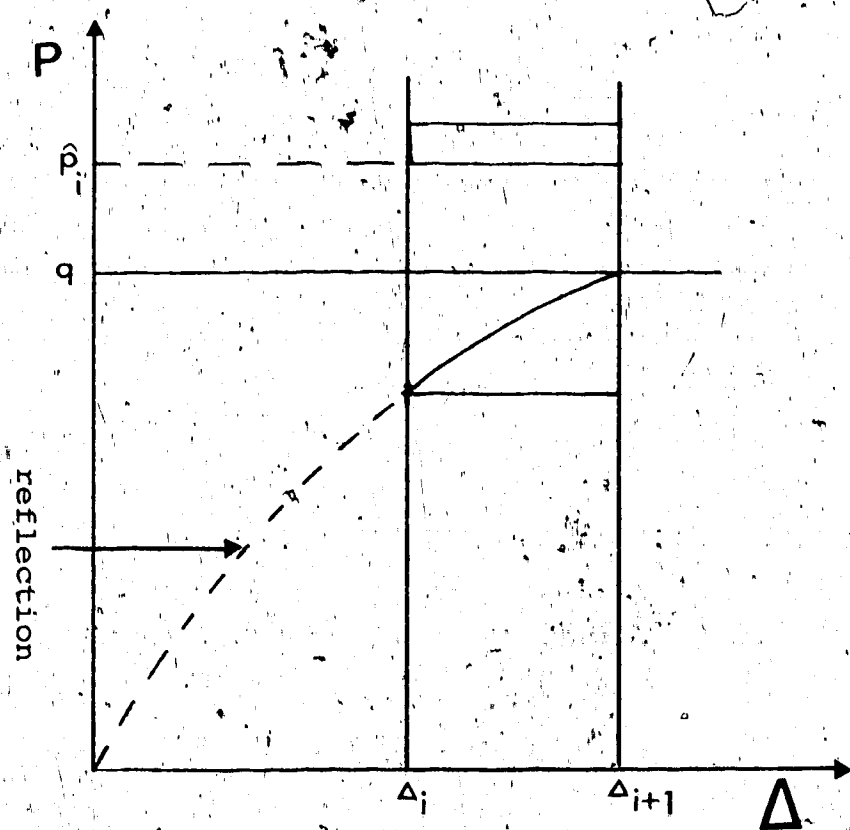


Fig. 5.5. The more general maximisation curve
in the i^{th} interval, where \hat{p}_i is the
value of p which will maximise $I^{(o)}(q)$
and also satisfy time constraints.

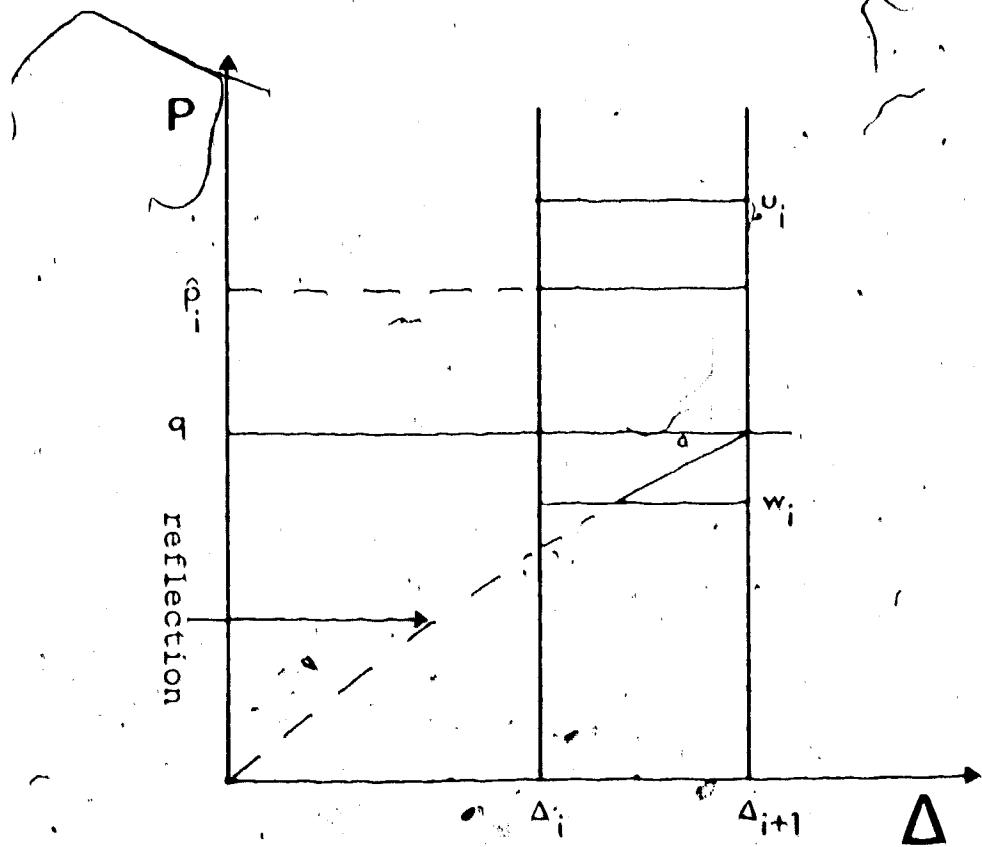


Fig. 5.6. The change in the maximisation curve
of fig. 5.5 for smaller value of q .

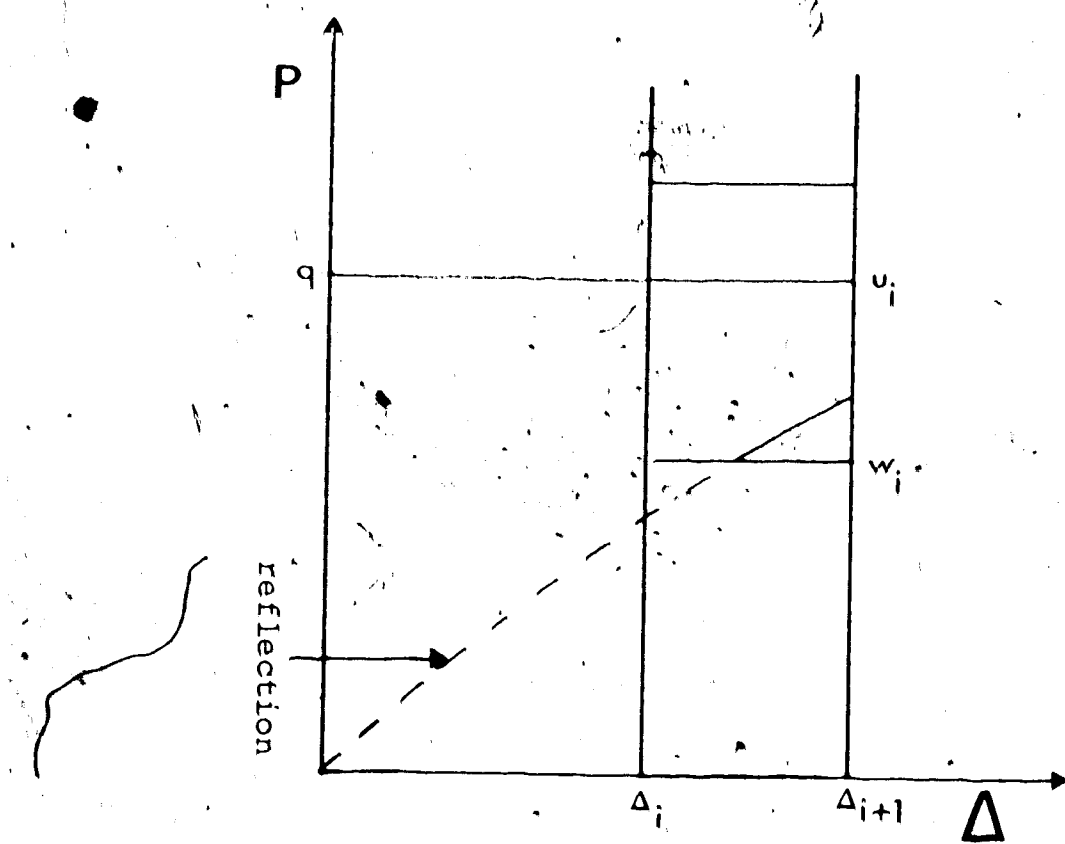


Fig. 5.7: The $p(\Delta)$ curve which will minimise
 $I^{(o)}(q)$ in the i^{th} interval, for
 $q > m_i$.

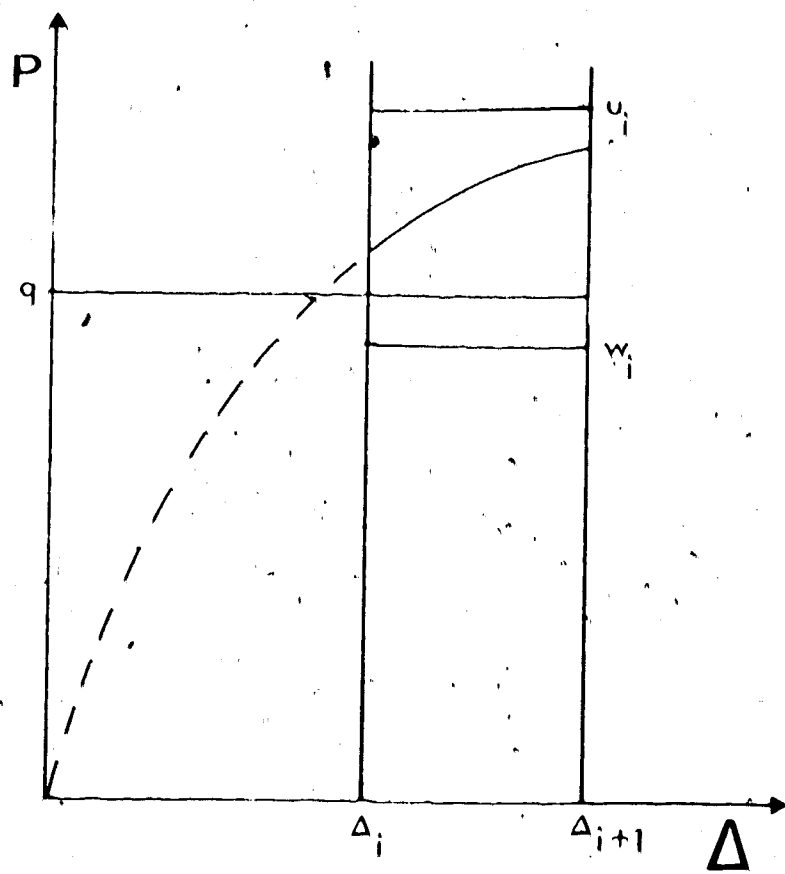


Fig. 5.8(a). Possible minimisation curve for

$$q < m_i.$$

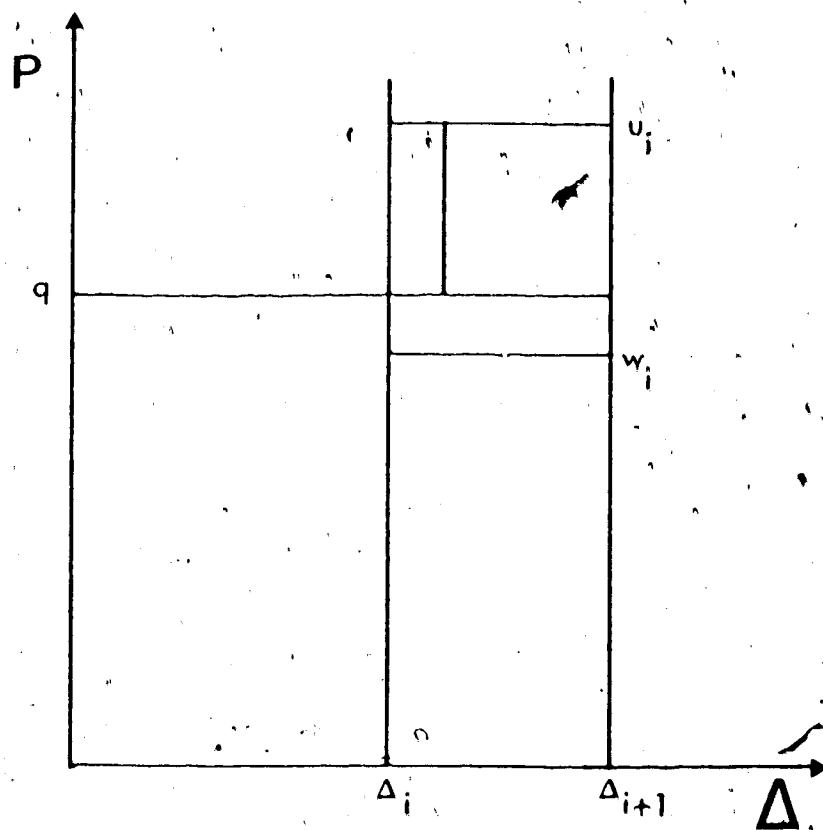


Fig. 5.8(b). Both this and fig. 5.8(a) show possible minimisation curves for $q < m_i$. The curve, giving the absolute minimum may be determined numerically.

CHAPTER 6

CONCLUSIONS

The results of the experiments with sampling intervals show that the more data available, the narrower the limits on the acceptable velocity-depth models become, which is as expected. However, by fixing part of the model, it appears that though making more assumptions about the higher regions of the earth does further restrict possible models in the near vicinity of the known region, little change in envelope width occurs at lower depths.

The results of computing individual profiles and their behaviour with respect to the extremal curves shows that although these profiles do touch the extremal curves at various depths, in general they lie within the envelope (though their exact behaviour depends on the actual data). In fact, the extremal curves, which show the largest ambiguity in velocity possible at any particular radius, are not themselves physically valid profiles. Thus averaging these extremal curves is not meaningful and to see the effect which averaging would have on the permissible amount of velocity variation, an averaged radius is defined and then suitably maximised and minimised for various averaging lengths.

Computations of these averaged envelopes for a number of averaging lengths show that averaging does reduce the envelope width considerably and for the range of depths considered the envelope width is reduced by 40% for an averaging length of 0.4 sec/deg. The exact way in which extremal curves vary with averaging length is dependent on the actual data (for similar reasons as for the exact behaviour of particular profiles with respect to the extremal curves, mentioned above). This type of computation is essential for any comparison with the more indirect inversion methods, such as Gilbert and Backus or Monte Carlo.

Maximisation and minimisation when high or low velocity zones are included is discussed in this thesis, though the analytic results obtained here have not been programmed. When this has been done, it will be possible to invert real data, which will facilitate a qualitative comparison of the extremal averaged curves obtained by this inversion method with the results of other inversions. For an interface such as the core-mantle boundary, it is possible to remove the effect of the low velocity zone by an 'earth-stripping' technique which effectively removes the earth's mantle and then inverts the reduced data. This technique is illustrated in this work, using both p and s wave data.

So far, to compute one velocity-depth envelope takes about 30 secs C.P.U. time, though when calculations for high and low velocity zones have been included, this time will obviously increase. A program for (T, Δ) data exists but does not contain subroutines to determine extremal averaged curves. The necessary programming for (p, Δ) data would be fairly simple and it is expected that both (T, Δ) and (p, Δ) envelopes will be wider than a corresponding (p, T, Δ) envelope.

With the present program, it should be possible to study the effect on the profiles of errors in the measurements, though a thorough analysis would require a systematic variation in all the given data parameters.

One of the more important aspects of this thesis is that the very nature of discrete data implies ambiguities in any inversion procedure. Tests show that these ambiguities may be reduced by increasing the amount of data and it may be further deduced that using time, distance and slowness data simultaneously will give the most restrictive envelope. However, there will always be some ambiguity.

The other important conclusion reached is that it is essential, when comparing with results from other inversion techniques, to understand exactly how these

comparisons should be made. The concept of an averaged radius, which must be maximised and minimised, is introduced so that it will now be possible to compare results from a Herglotz-Wiechert inversion procedure with other types of inversion.

REFERENCES

Abramowitz, M. and I. Stegun, 1965, Handbook of Mathematical Functions, Dover Publications, New York.

Bateman, H., 1910, The solution of the integral equation connecting the velocity of propagation of an earthquake in the interior of the earth with the times which the disturbance takes to travel to the different stations on the earth's surface, Phil. Mag., 19, 576-587 and Phys. Z., 11, 96-99.

Båth M., 1968, Mathematical Aspects of Seismology, Elsevier Publishing, New York.

Berry, M.J., 1971, Depth uncertainties from seismic first arrival refraction studies, J. Geophys. Res., 76, 26, 6464-6468.

Bessonova, E.N., V.M. Fishman and G.A. Sitnikova, 1970, Determination of the limits for velocity distribution from discrete travel-time observations, presented by V. Keilis Borok at the Seventh Upper Mantle Committee Symposium on Geophysical Theory and Computers, Södergarn, Sweden.

Bessonova, E.N., V.M. Fishman, V.Z. Rjabozi and G.A. Sitnikova, 1973, Method τ for inversion of traveltimes I, preprint.

Bolt, B.A., 1970, PdP and PKiKP waves and diffracted PcP waves, Geophys. J. Roy. Astron. Soc., 20, 367-382.

Bolt, B.A., 1972, Density distributions near the base of the mantle and near the earth's centre, Phys. Earth. Planet. Interiors, 5, 301-311.

Bullen, K.E., 1965, An Introduction to the Theory of Seismology, Cambridge University Press, London.

Chapman, C.H., 1971, On the computation of seismic ray travel times and amplitudes, B.S.S.A., 61, 5, 1267-1274.

Chapman, C.H., 1972, Personal communication.

Gerver, M. and V. Markushevich, 1966, Determination of a seismic wave velocity from the travel-time wave, Geophys. J., 11, 165²173.

Gerver, M. and V. Markushevich, 1967, On the characteristic properties of travel-time curves, Geophys. J., 13, 241-246.

Herglotz, G., 1907, Über das Benndorfsche Problem der Fortpflanzungsgeschwindigkeit der Erdbebenstrahlin, Phys. Z., 8, 145-147.

Johnson, L.R., 1967, Array measurements of P-velocities in the upper mantle, J. Geophys. Res., 72, 6309-6325.

Johnson, L.E. and J.F. Gilbert, 1972, Inversion and inference for teleseismic ray data: Methods in Computation Physics, ed. B.A. Bolt, B. Alder, S. Ferbach and M. Rotenberg, Academic Press, New York, 321-266.

Keilis Borok V., 1970, Inverse problem of seismology:
International School of Physics, "Enrico Fermi",
Villa Monastero, Varenna sul Lago di Como,
preprint.

Keilis Borok V.T. and T.B. Yanovskaya, 1967, Inverse
problems in seismology, Geophys. J. Roy. Astron.
Soc., 13, 223-234.

Knopoff L. and T.L. Tong, 1965, Analytic calculation of
the seismic travel time problem, Rev. Geophys.,
3, 1, 11-24.

Macelwane, J.B., 1951, Evidence on the interior of the
earth derived from seismic sources: Internal
Constitution of the Earth, ed. B. Gutenberg,
Dover Publications, New York, 227-305.

McMechan, G.A., 1971, Depth limits in body wave inversion,
M.Sc. Thesis, University of Toronto.

McMechan, G.A. and R.A. Wiggins, 1972, Depth limits in
body wave inversion, Geophys. J. Roy. Astron. Soc.,
28, 459-473.

Phinney, R.A., 1969, Reflection of acoustic waves from a
continuously varying interfacial region, Rev.
Geophys., 8, 517-532.

Press, F., 1970a, Earth models consistent with geophysical
data, Phys. Earth. Planet. Interiors, 3, 3-22.

Press, F., 1970b, Regionalized earth models, *J. Geophys. Res.*, 75, 6575-6581.

Richards, P., 1971, Potentials for elastic displacement in spherically symmetric media, *J. Acoust. Soc. Am.*, 50, 188-197.

Wiechert, E., 1910, Bestimmung des Weges der Erdbebenwellen im Erdinnern, I, Theoretisches, *Phys. Z.*, 11, 294-304.

Wiggins, R.A., 1969, Monte Carlo inversion of body wave observations, *J. Geophys. Res.*, 74, 3173-3181.

Wiggins, R.A., 1972, The general linear inverse problem: implication of surface waves and free oscillations for earth structure, *Rev. Geophys. Space Phys.*, 10, 251-285.

Wiggins, R.A., G.A. McMechan and N.N. Toksöz, 1973, Range of earth structure non uniqueness implied by body wave observations, *Rev. Geophys. Space Phys.*, 11, 1, 87-114.

APPENDIX 1

At high frequencies (Richards, 1971) the wave function ϕ is described by the Helmholtz wave equation

$$\nabla^2 \phi - \frac{1}{v^2} \frac{\partial^2 \phi}{\partial t^2} = 0$$

This transforms to

$$\frac{\partial^2 \phi}{\partial r^2} + \xi^2(r) \phi = 0 \quad (\text{A1.1})$$

where

$$\xi(r) = \left(\frac{\omega^2}{v^2} - \frac{v^2}{r^2} \right)^{\frac{1}{2}}$$

At the turning point of the ray

$$\xi(r_t) = 0$$

where

$$\xi(r) = \frac{\omega}{r} (n^2 - p^2)^{\frac{1}{2}} \quad (v = \omega p)$$

Using the above results, Chapman (1972) has shown the following:

Type I discontinuity:

For $r \rightarrow r^{(k)}$, $\xi^2(r)$ may be approximated by a linear function, so that equation (A1.1) reduces to Stokes equation. Assuming the free boundary condition, $\phi(r^{(k)}) = 0$, the reflection coefficient becomes

$$R(r_0, v) = \exp\left(\frac{i\pi}{6} + i\omega\tau(p)\right) \frac{Ai(te^{-2\pi i/3})}{Ai(te^{2\pi i/3})} \quad (Al.2)$$

where

$$\frac{2}{3} t^{2/3} = -i \int_{S(p)}^{r(k)} \xi(r) dr$$

($t \rightarrow \infty$, if no interface present).

The poles of $R(r_0, v)$ exist at

$$v_j = \omega p^{(k)} + \left(\frac{\omega p^{(k)}}{2}\right)^{1/3} \left(1 - \frac{r^{(k)} v_j^{(k)} e^{2/3}}{r^{(k)}}\right)^{1/2} e^{i\pi/3} \sigma_j$$

where $Ai(-\sigma_j) = 0$. These v_j 's give rise to the diffracted signal, which implies a decay rate of

$$e^{-\lambda_j (\Delta - \Delta^{(k)})}$$

for a diffracted signal with $\Delta > \Delta^{(k)}$, where

$$\lambda_j = \left(\frac{\omega r^{(k)}}{2}\right)^{1/3} \left(1 - \frac{r^{(k)} v_j^{(k)} e^{2/3}}{r^{(k)}}\right)^{1/2} \frac{\sqrt{3}}{2} \sigma_j \quad (Al.3)$$

It should be noted that at large ranges, the $j = 0$ term will predominate where $\sigma_0 = 2.3381$. More realistic boundary conditions cause poles intermediate between the Airy zeros but with the same frequency dependence.

Type II discontinuity:

$$n'(r^{(k)}) = 0$$

Therefore, for $r > r^{(k)}$, $\xi^2(r)$ must be approximated by

a quadratic. Equation (Al.1) then has the parabolic cylindrical functions as solutions. The reflection coefficient is (Phinney, 1969)

$$R(r_0, v) = - \frac{E^*(a, -t)}{E(a, -t)} \exp(i\omega t(p)) \quad (\text{Al.4})$$

where

$$a = -\frac{1}{2} \left(\frac{v(k)^3}{\omega^2 v''(k)} \right)^{\frac{1}{2}} \left(\frac{\omega^2}{v(k)^2} - \frac{v^2}{r(k)^2} \right)^{\frac{1}{2}}$$

As $t \rightarrow \infty$

$$\frac{E^*(a, -t)}{E(a, -t)} \rightarrow \frac{e^{\pi a^*}}{\sqrt{1 + e^{2\pi a^*}}} \quad (\text{Abramowitz and Stegun, 1965, 19.18.3})$$

The poles of $R(r_0, v)$ exist when

$$a = i(j + \frac{1}{2})$$

$$\text{i.e. } v_j = \omega p^{(k)} + i \left| \frac{r(k)^2 v''(k)}{v(k)} \right|^{\frac{1}{2}} (j + \frac{1}{2})$$

The decay rate of the diffracted signal, for $\Delta > \Delta^{(k)}$, is of the same exponential form as above with

$$\lambda_j = \left| \frac{r(k) v''(k)}{v(k)} \right|^{\frac{1}{2}} (j + \frac{1}{2}) \quad (\text{Al.5})$$

which is independent of frequency. Again, at large ranges only the $j = 0$ term will be important.

Type I' discontinuity:

The reflection coefficient is the same as equation (A1.4) with $t = 0$. Then

$$E(a, 0) = \frac{\frac{1}{2} \frac{1}{4}\pi a + \frac{1}{2}i\pi + \frac{1}{2}i \arg \Gamma(\frac{1}{2}+ia)}{\frac{1}{2} \frac{1}{2} - \frac{1}{4} \Gamma(\frac{3}{4} + \frac{ia}{2})}$$

(Abramowitz and Stegun, 1965, 19.3.5, 19.17.9)

$R(r_o, v)$ will have poles where

$$a = i(2j + \frac{3}{2}) \quad \text{(A1.6)}$$

These correspond to the odd poles of (A1.5) which will be asymmetric. The exact numerical factor depends on the boundary conditions. If $\phi' = 0$ had been taken as a rigid surface ($u_z = 0$) then the even poles would have been obtained.

As can be seen from the above, amplitude-frequency dependence will distinguish a type I discontinuity from I' and II. I' and II must be differentiated using some other data.



APPENDIX 2

For a type I discontinuity (Chapman, 1972) the range of the ray tends to infinity as p tends to $p^{(k)}$. That is beyond a certain $\Lambda(p)$, the original becomes infinitely small in amplitude due to increased geometrical spreading. Consider

$$\Lambda(p) = 2p \int_{r^{(k)}+\epsilon}^{\infty} \frac{dr}{r(n^2 - p^2)^{\frac{1}{2}}} + 2p \int_{s(p)}^{r^{(k)}+\epsilon} \frac{dr}{r(n^2 - p^2)^{\frac{1}{2}}}$$

For $r^{(k)} \leq r \leq r^{(k)} + \epsilon$

$$n(r) \approx p^{(k)} + \frac{1}{2} n''(k) (r - r^{(k)})^2 + \dots \quad (\text{A2.1})$$

$$n^2(r) \approx p^{(k)2} + p^{(k)} n''(k) (r - r^{(k)})^2 + \dots$$

and hence, using the substitution $y = r^{-1}$

$$\begin{aligned} & 2p \int_{s(p)}^{r^{(k)}+\epsilon} \frac{dr}{r(n^2 - p^2)^{\frac{1}{2}}} \approx 2p \int_{s(p)}^{r^{(k)}+\epsilon} \frac{dr}{r(p^{(k)2} + p^{(k)} n''(k) (r - r^{(k)})^2 - p^2)^{\frac{1}{2}}} \\ & = 2p \int_{(r^{(k)}+\epsilon)^{-1}}^{s^{-1}(p)} \frac{dy}{[(p^{(k)2} - p^2 + p^{(k)} n''(k) r^{(k)2}) y^2 - 2p^{(k)} n''(k) r^{(k)} y + p^{(k)} n''(k)]^{\frac{1}{2}}} \\ & = -2p [p^{(k)2} - p^2 + p^{(k)} n''(k) r^{(k)2}]^{-\frac{1}{2}} \ln |2[p^{(k)2} - p^2 + p^{(k)} n''(k) r^{(k)2}]^{\frac{1}{2}} \\ & \quad \times \{[p^{(k)2} - p^2 + p^{(k)} n''(k) r^{(k)2}] y^2 - 2r^{(k)} n''(k) y + p^{(k)} n''(k)\}^{\frac{1}{2}} \\ & \quad + 2[p^{(k)2} - p^2 + p^{(k)} n''(k) r^{(k)2}] y - 2r^{(k)} p^{(k)} n''(k) | \int_{(r^{(k)}+\epsilon)^{-1}}^{s^{-1}(p)} \end{aligned} \quad (\text{A2.2})$$

(Abramowitz and Stegun, 1965, 3.3.33).

Near the turning point, $r^{(k)}$, $s^{-1}(p) \approx r^{(k)}$ and hence the argument of the logarithm tends to zero (i.e. $\Delta \rightarrow \infty$). To first order

$$y = \frac{1}{r^{(k)}} - \delta y \quad \delta r = r^{(k)} \delta y$$

$$p = p^{(k)} + \delta p = p^{(k)} + \frac{\eta''(k) r^{(k)} 4}{2} \delta y^2$$

$$p^2 - p^{(k)}^2 = p^{(k)} \eta''(k) r^{(k)} 4 \delta y^2$$

Thus

$$\left. 2p \int_{s(p)}^{r^{(k)} + \epsilon} \frac{dr}{r(\eta^2 - p^2)} \right\} \approx \frac{2}{r^{(k)}} \left(\frac{p^{(k)}}{\eta''(k)} \right)^{1/2} \ln \left(\frac{\epsilon}{\delta r} \right) + \dots$$

To determine the amplitude, which is related to $|d\Delta/dp|^{-1/2}$, note that

$$\frac{d\Delta}{dp} \approx - \left(\frac{p^{(k)}}{\eta''(k)} \right)^{1/2} \frac{2}{\delta r} \frac{\delta r}{\delta p} + \dots$$

and hence the amplitude is governed by

$$\left(\frac{\eta''(k)}{p^{(k)}} \right)^{1/2} \delta p^{1/2} = C \exp \left(-\Delta(p) \frac{r^{(k)}}{2} \left[\frac{\eta''(k)}{p^{(k)}} \right]^{1/2} \right) \quad (A2.3)$$

This result is identical to the asymptotic form of the wave solution (A1.5 with $j = 0$).

APPENDIX 3

As shown by Chapman (1972), $\eta(r) = \eta_{\min}^{(k)}(r)$ and $\eta(r) = \eta_{\max}^{(k)}(r)$ will respectively maximise and minimise $r = s(q)$. From Chapter 2, it will be recalled that

$$\delta_T^{(k)} = 2 \int_{\bar{r}^{(k)}}^{r^{(k)}} \frac{1}{r} \left(\eta^{(k)} - p^{(k)} \right)^2 dr \quad (A3.1)$$

Thus for $\eta = \eta_{\min}^{(k)}$

$$\bar{r}^{(k)} = r^{(k)} \exp \left(\frac{\delta_T^{(k)}}{2 \left(\eta_{\min}^{(k)} - p^{(k)} \right)^{1/2}} \right) \quad (A3.2)$$

where it should be noted that if $\eta_{\min}^{(k)}(r) \rightarrow p^{(k)}$, then $\bar{r}_{\min}^{(k)} \rightarrow 0$, which is not desirable. Also, at $\eta = \eta_{\min}^{(k)}$

$$I^{(k)}(q) = \int_{\bar{r}^{(k)}}^{r^{(k)}} \frac{2}{r} \tan^{-1} \sqrt{\frac{\eta_{\min}^{(k)}(r) - p^{(k)}}{p^{(k)} - q^2}} dr \quad (A3.3)$$

To determine whether (A3.3) gives the absolute minimum integral, $\eta(r)$ is perturbed to $\eta_{\min}^{(k)}(r) + \delta\eta(r)$ and the corresponding perturbations in $\bar{r}^{(k)}$ and $I^{(k)}(q)$ observed.

By differentiating equation (A3.2) and substituting from (A3.1);

$$\delta \bar{r}^{(k)} = \frac{\bar{r}^{(k)}}{(n_{\min}^{(k)}(\bar{r}^{(k)})^2 - p^{(k)2})^{\frac{1}{2}}} \int_{\bar{r}^{(k)}}^{r^{(k)}} \frac{n_{\min}^{(k)}(r) \delta n(r)}{\bar{r}^{(k)} r(n_{\min}^{(k)}(r)^2 - p^{(k)2})^{\frac{1}{2}}} dr \quad (A3.4)$$

to first order. Similarly, perturbing (A3.3) and substituting for $\delta \bar{r}^{(k)}$ from equation (A3.4), then:

$$\begin{aligned} \delta I^{(k)}(q) &= 2(p^{(k)2} - q^2)^{\frac{1}{2}} \left[\int_{\bar{r}^{(k)}}^{r^{(k)}} \frac{n_{\min}^{(k)}(r) \delta n(r)}{\bar{r}^{(k)} r(n_{\min}^{(k)}(r)^2 - q^2)(n_{\min}^{(k)}(r)^2 - p^{(k)2})^{\frac{1}{2}}} dr \right. \\ &\quad \left. - \tan^{-1} \sqrt{\frac{n_{\min}^{(k)}(\bar{r}^{(k)})^2 - p^{(k)2}}{p^{(k)2} - q^2}} \int_{\bar{r}^{(k)}}^{r^{(k)}} \frac{n_{\min}^{(k)}(r) \delta n(r)}{\bar{r}^{(k)} r(n_{\min}^{(k)}(r)^2 - p^{(k)2})^{\frac{1}{2}}} dr \right] \\ &= 2 \int_{\bar{r}^{(k)}}^{r^{(k)}} \frac{n_{\min}^{(k)}(r) \delta n(r)}{\bar{r}^{(k)} r(n_{\min}^{(k)}(r)^2 - p^{(k)2})^{\frac{1}{2}}} \frac{(p^{(k)2} - q^2)^{\frac{1}{2}}}{(n_{\min}^{(k)}(\bar{r}^{(k)})^2 - q^2)^{\frac{1}{2}}} \\ &\quad \times \left\{ \frac{n_{\min}^{(k)}(\bar{r}^{(k)})^2 - q^2}{n_{\min}^{(k)}(r)^2 - q^2} - \frac{\phi}{\sin \phi} \right\} dr \quad (A3.5) \end{aligned}$$

where

$$\phi(q) = 2 \tan^{-1} \sqrt{\frac{n_{\min}^{(k)}(\bar{r}^{(k)})^2 - p^{(k)2}}{p^{(k)2} - q^2}}$$

Obviously, to determine whether $n(r) = n_{\min}^{(k)}$ maximises the integral it is necessary to determine the sign of the bracketed terms in equation (A3.5), and this may be done on a qualitative basis by plotting the behaviour of these terms. If it is first assumed that $n_{\min}^{(k)}$ has a minimum, denoted by $n_{\min}^{(k)*}$, within the k^{th} low velocity channel, then

$$n_{\min}^{(k)} \geq n_{\min}^{(k)*} \geq p^{(k)}$$

and

$$\frac{n_{\min}^{(k)}(\bar{r}^{(k)})^2 - q^2}{n_{\min}^{(k)}(r)^2 - q^2} \leq \frac{n_{\min}^{(k)}(\bar{r}^{(k)})^2 - q^2}{n_{\min}^{(k)*}(r)^2 - q^2}$$

For a type II discontinuity, $n_{\min}^{(k)*} = p^{(k)}$, so that

$$\frac{n_{\min}^{(k)}(\bar{r}^{(k)})^2 - q^2}{n_{\min}^{(k)}(r)^2 - q^2} \approx \frac{n_{\min}^{(k)}(\bar{r}^{(k)})^2 - p^{(k)}^2}{2p^{(k)}} \cdot \frac{1}{(p^{(k)} - q)}$$

where

$$\frac{d}{dq} \left(\frac{n_{\min}^{(k)}(\bar{r}^{(k)})^2 - q^2}{n_{\min}^{(k)}(r)^2 - q^2} \right) = \frac{2q(n_{\min}^{(k)}(\bar{r}^{(k)})^2 - n_{\min}^{(k)}(r)^2)}{(n_{\min}^{(k)}(r)^2 - q^2)^2}$$

Further, $\phi \approx \pi$ and therefore

$$\frac{\phi}{\sin \phi} \approx \frac{\pi}{\pi - \phi}$$

$$\frac{\pi - \phi}{2} = \tan^{-1} \sqrt{\frac{p^{(k)2} - q^2}{n_{\min}^{(k)}(\bar{r}^{(k)})^2 - p^{(k)2}}}$$

$$\approx \sqrt{\frac{2p^{(k)}(p^{(k)} - q)}{n_{\min}^{(k)}(\bar{r}^{(k)})^2 - p^{(k)2}}}$$

Thus

$$\frac{\phi}{\sin \phi} \approx \frac{\pi}{2} \sqrt{\frac{n_{\min}^{(k)}(\bar{r}^{(k)})^2 - p^{(k)2}}{2p^{(k)}(p^{(k)} - q)}}$$

where it should be noted that

$$\frac{\phi}{\sin \phi} = \frac{\phi/2}{\sin \frac{\phi}{2} \cos \frac{\phi}{2}} > \sec \frac{\phi}{2} = \frac{n_{\min}^{(k)}(\bar{r}^{(k)})}{p^{(k)}}$$

These approximations to the terms in brackets in equation (A3.5) are as shown in fig. (A3.1) where it can be seen that for the most part, the term in brackets is negative, making $\delta I^{(k)}(q)$ negative for positive δn . That is, that $n(r) = n_{\min}^{(k)}(r)$ will maximise $I^{(k)}(q)$ and, therefore, minimise velocity for any given q . The question of maximising velocity may be similarly treated, with $n(r) = n_{\max}^{(k)}(r)$ to obtain expressions for $\bar{r}^{(k)}$ and $I^{(k)}(q)$ which are then perturbed by changing $n(r)$ to $n_{\max}^{(k)}(r) - \delta n(r)$.

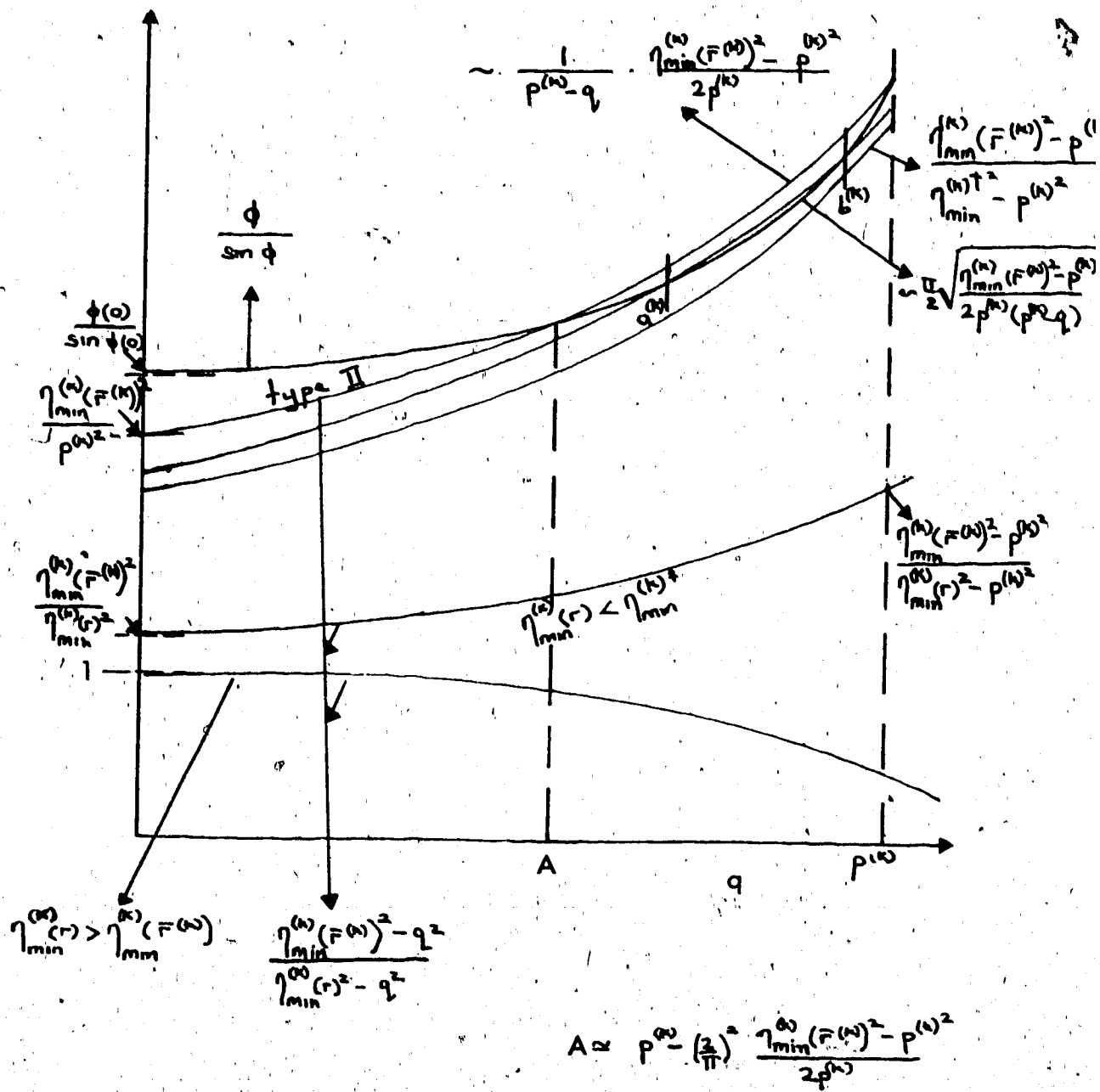


Fig. A3.1. Diagram to show behaviour of $\phi/\sin \phi$ and $(n_{\min}^{(k)}(r))^{-2} - q^2)/n_{\min}^{(k)}(r)^2 - q^2$ and hence determine the sign of $\delta I^{(k)}(q)$.

However it should be noted that at the points $a^{(k)}$ and $b^{(k)}$ shown in fig. A3.1 the two curves intersect so that the bracket term in equation (A3.5) changes sign, which is possible for $\eta(r) \leq n_{\min}^{(k)*}$ and will certainly be the case for a type II discontinuity as $n_{\min}^{(k)*} = p^{(k)}$ then. Thus at $r = r^{(k)}$ for a type II discontinuity

$$p^{(k)} - \left(\frac{2}{\pi}\right)^2 \cdot \frac{n_{\min}^{(k)}(r^{(k)})^2 - q^2}{2p^{(k)}} = a^{(k)}(p^{(k)}) < q < b^{(k)}(p^{(k)}) = p^{(k)}$$

and in general

$$a_{\min}^{(k)} = a^{(k)}(n_{\min}^{(k)*})$$

$$b_{\max}^{(k)} = b^{(k)}(n_{\min}^{(k)*})$$

and at some critical value $n_{\min}^{(k)\dagger}$

$$a^{(k)}(n_{\min}^{(k)\dagger}) = b^{(k)}(n_{\min}^{(k)\dagger})$$

For this range of q , $a^{(k)}(n_{\min}^{(k)}(r)) < q < b^{(k)}(n_{\min}^{(k)}(r))$ and corresponding $n_{\min}^{(k)}(r) > n_{\min}^{(k)\dagger}$, equation (A3.3) will not give the minimum integral (i.e. for a range of depths below the low velocity channel, the extremal channel model will not coincide with the extremal velocity profile below the channel). This range may be easily determined by solving the equation

$$\frac{n_{\min}^{(k)}(\bar{r}^{(k)})^2 - q^2}{n_{\min}^{(k)}(r)^2 - q^2} = \frac{\phi}{\sin \phi}$$

The exact perturbation of the low velocity channel which is required is not obvious and should probably be determined by trial and error. This will not be too ambiguous because both the q and r ranges are restricting factors.

The above discussion is probably best illustrated in the radius-velocity plot of fig. A3.2, where it should be noted that in a region below the low velocity channel the channel model does not correspond to the extremal profiles. These must be obtained by perturbing the channel model within the shaded area of the diagram.

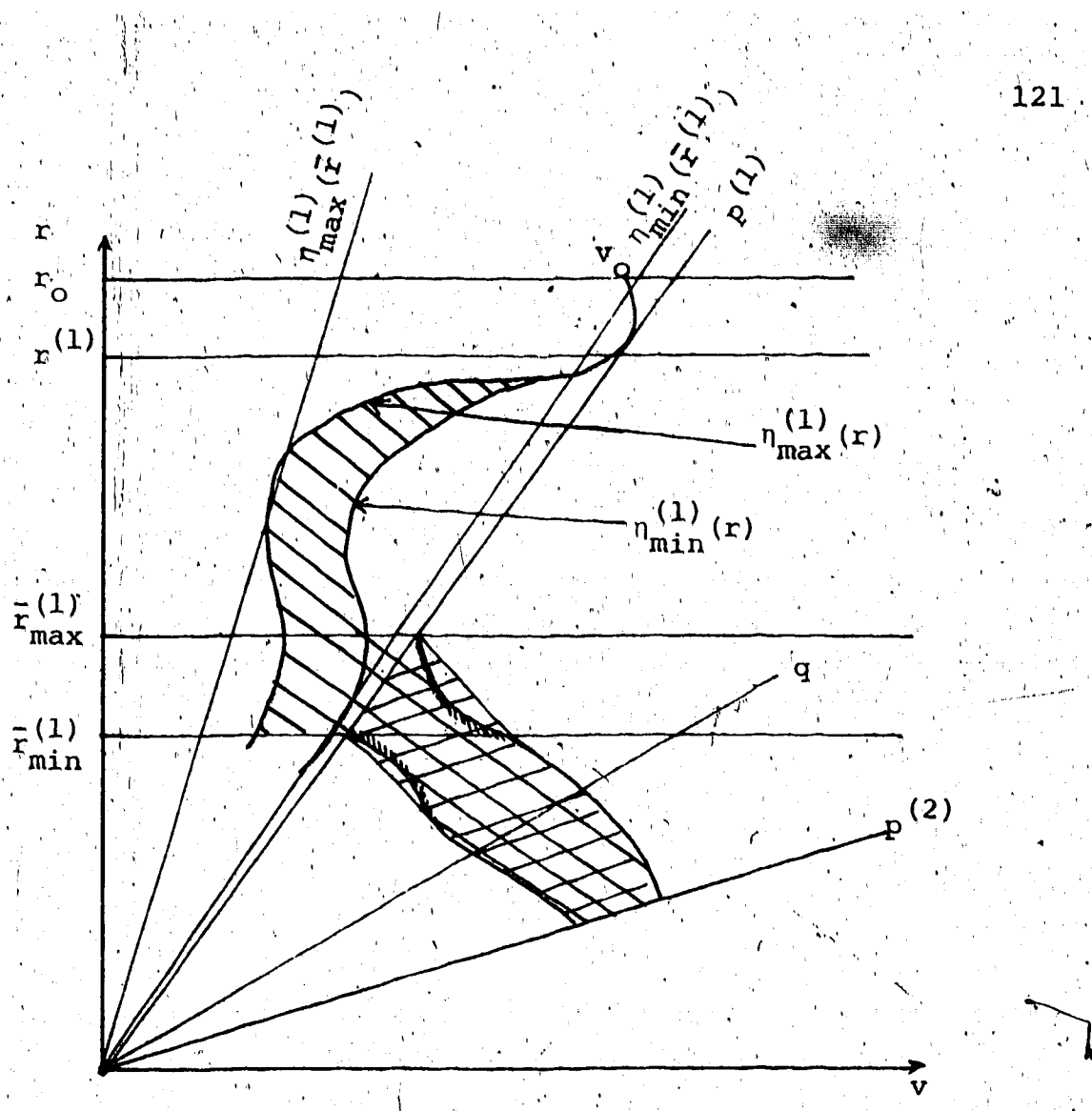


Fig. A3.2. A radius-velocity plot for a low velocity channel with $\bar{r}_{\max}^{(1)}$ and $\bar{r}_{\min}^{(1)}$ the maximum and minimum radii for the bottom of the low velocity channel (as determined by $\delta\tau^{(1)}$).

The shaded curves are those obtained from the low velocity channel model while the cross-hatched area is produced by perturbing the model.